Numerical Modelling of Entropy Production in Mixed Convection Heat Transfer

By

© Peter Unor Ogban

A thesis submitted to the School of Graduate Studies

in partial fulfillment of the requirements for the degree of

Doctor of Philosophy

Faculty of Engineering and Applied Science

Memorial University of Newfoundland

St. John's, Newfoundland and Labrador

October 2020

ABSTRACT

Energy losses in fluids engineering systems occur due to thermal and viscous irreversibilities. These irreversibilities can be tracked to identify regions of design modification for efficiency improvement in thermofluid systems. The rate of entropy production in numerical heat transfer is an important parameter that characterizes the degree of these irreversibilities. This can lead to improved designs with higher system efficiency levels for energy savings in various engineering applications. Previous conventional techniques have generally detected energy losses on a global scale or end-to-end basis.

This thesis focuses on two-dimensional numerical modeling of entropy generation and the Second Law of Thermodynamics in mixed convection heat transfer. A Control-Volume Based Finite Element Method (CVFEM) is used to discretize and solve the governing conservation equations. An entropy-based algorithm is developed by post-processing of the velocity and temperature fields to obtain numerical predictions of the rate of entropy production. The new model is used to analyze heat transfer and entropy production for both natural and mixed convection in enclosures filled with different fluids, including nanofluids. The optimal conditions for which viscous and thermal irreversibilities are minimized is analyzed. The results from Computational Fluid Dynamics (CFD) are validated using available benchmark data. A new approach for minimizing the rate of entropy production in different flow configurations with nanofluids is also obtained.

In addition, the local entropy production rates are obtained from two forms of the discretized Second Law – namely, transport and positive-definite forms of the entropy

transport equation. The computed local entropy generation rates from both methods are compared and related to expected numerical errors from available benchmark solutions. An entropy-based error indicator is determined to assess the solution accuracy of fluid flow simulations with heat transfer using the Second Law of Thermodynamics. The formulation presents a new approach for the characterization of numerical error using a parameter called the "apparent entropy production difference." Furthermore, a corrective mechanism on the numerical algorithm is developed. The transport entropy is used to calculate an artificial viscosity (named as an entropy-based artificial viscosity) to reduce the numerical error and ensure closer compliance with the Second Law.

ACKNOWLEDGEMENTS

I wish to express my heartfelt gratitude to all the people who have contributed to making this thesis possible. I am forever grateful to my supervisor, Dr. Greg F. Naterer, for the opportunity to undertake this research, for his guidance, patience, support, constant encouragement, and mentorship. I have benefitted immensely from his expertise in Entropy Based Design and the Second Law, technical reporting, presentation, and leadership. This research would not have been possible without his expert advice.

I would also like to acknowledge my supervisory committee members, Dr. Neil Hookey and Dr. Sohrab Zendehboudi, for their valuable expertise, instructions, training, and useful feedback in the course of this work. This work was supported by a research grant from the Natural Sciences and Engineering Research Council of Canada (NSERC) to my supervisor. A Graduate Fellowship from Memorial University of Newfoundland, and part living cost support from the Petroleum Technology Development Fund (PTDF) is also gratefully acknowledged.

I sincerely thank my friends and colleagues, Ahmed Elruby, Liam Long, Kshama Roy, and Cleverson Esene, for their helpful support, insightful discussion, and resources they provided. I dearly appreciate my lovely wife, Faith, for her sacrifice, love and understanding during my studies. Our children, Daniella and Jason, have been a source of joy and motivation. I am grateful to my mother and siblings for their prayers and support. Above all, I am thankful to God almighty for the gift of health, family, and friends during my Ph. D. studies and my life in general.

DEDICATION

This work is dedicated to my parents, the late Mr. Emmanuel Ogban and Mrs. Josephine Ogban, my wife Faith, and our children Daniella and Jason.

TABLE OF CONTENTS

NOMENCLATURE

x, y	Cartesian coordinates
u, v	Velocity components (m/s)
L	Length of enclosure (m)
H	Height of enclosure (m)
g	Gravitational acceleration (m/s^2)
C_p	Specific heat capacity (J/kg K)
k	Thermal conductivity (W/m K)
T	Temperature (K)
$q_0^{"}$	Heat flux (W/m^2)
$\dot{P}_s$	Rate of entropy production (W/m^{3}K)
$\dot{P}_s^*$	Dimensionless rate of entropy production
$\Delta\dot{P}_s$	Apparent entropy production difference (W/m^{3}K)
$\Delta\dot{P}_{s,n}$	Normalized apparent entropy production difference
$\Delta x, \Delta y$	Grid spacing
E_Θ	Dimensionless error in temperature
E_U	Dimensionless error in u-velocity
Ra	Rayleigh number $\left(\frac{g\beta_f \Delta T H^3}{v_f \alpha_f}\right)$
Pr	Prandtl number $\left(\frac{v_f}{\alpha_f}\right)$
ϕ_n	Normalized variable

k_{eff}	Effective thermal conductivity $\left(\frac{k_{nf}}{k_f}\right)$
Gr	Grashof number $\left(\frac{g\beta_f \Delta T H^3}{{v_f}^2}\right)$
Nu	Nusselt number
h	Heat transfer coefficient (W/m^{2}K)
$1/\Delta X$	Grid spacing

Superscripts and subscripts

max	Maximum value
min	Minimum value
pd	Positive-definite
te	Transport equation
av	Artificial viscosity
avg	Average value
p	Solid particle
f	Base fluid
nf	Nanofluid
c	Cold
h	Hot
ip	Integration point
w	Wall
eff	Effective

o	Initial
r	Reference state
t	Present state
*	Dimensionless

Greek Symbol

Ø	Nanoparticle volume fraction (%)
ϕ	Integration point of scalar variable
Φ	Viscous dissipation function (s^{-2})
ρ	Density (kg/m^3)
β	Thermal expansion coefficient (K^{-1})
α	Thermal diffusivity (m^2/s)
μ	Dynamic viscosity (m^2/s)
v	Kinematic viscosity (m^2/s)
Θ	Dimensionless temperature $\left[\frac{T-T_c}{T_h-T_c}\right]$

List of Abbreviations

CFD = Computational Fluid Dynamics

CVFEM = Control Volume Based Finite Element Method

CDS = Central Differencing Scheme

UDS = Upwind Differencing Scheme

EDS = Exponential Differencing Scheme

FIDAP = Fluid Dynamics Analysis Program

AR = Aspect Ratio

CFL = Courant Friedrichs Lewy

EA = Exergy Analysis

EGM = Entropy Generation Minimization

MWCNT = Multi-Walled Carbon Nano-Tube

SWCNT = Single-Walled Carbon Nano-Tube

MOOSE = Multi-Physics Object Oriented Simulation Environment

HEMP = Hydrodynamic, Elastic, Magneto, and Plastic

SIPG = Symmetric Interior Penalty Galerkin

DSEM = Discontinuous Spectral Element Method

LIST OF TABLES

LIST OF FIGURES

1 INTRODUCTION

1.1 Background

The world's energy demand continues to increase dramatically. Energy efficiency and availability are major issues of global concern. In order to ensure a sustainable energy supply with a lower environmental impact, better planning and management of limited energy resources is required. Hence, there is an increasing need for the design and development of engineering systems with higher energy efficiency and environmental sustainability. Entropy and the Second Law of Thermodynamics will have an increasingly important role in these endeavors.

Thermofluid systems such as aircraft propulsion, heat exchangers, energy storage, and power generation have performance losses due to viscous, thermal, and other thermodynamic irreversibilities. The Second Law can serve as a useful design tool for the optimization of these fluid, thermal, and energy systems [1]. The rate of entropy production can be used in numerical heat transfer as an important parameter to quantify the degree of these irreversibilities. The local values of thermal and frictional components of entropy production can be tracked to identify regions for design modification [2]. This can lead to improved designs with higher levels of system efficiency for energy savings in various engineering applications. Previous conventional techniques have generally detected energy losses on a global scale or end-to-end basis. This research aims to use entropy and the Second Law instead as key design parameters.

1.2 Motivation for Research

The design of thermofluid systems is governed by fundamental principles such as the conservation laws of fluid motion and energy. The First Law of Thermodynamics characterizes the quantity of energy in a system, while the Second Law of Thermodynamics measures the quality of energy or its potential to do useful work. The Second Law provides a special insight into energy use, its optimization, and the most effective technology selection. This research focuses on a novel application of the Second Law to the prediction of thermal and viscous irreversibilities locally instead of globally. This would track the regions of highest entropy generation rates to identify the regions of needed design improvements. An analogy would be "a sick patient telling a doctor that he/she is sick, without knowing the part of the body that is causing the ailment" [2].

One of the goals of this thesis is to develop a diagnostic tool for tracking energy losses (irreversibilities) in thermofluid systems through the computation of entropy production. Designers of energy systems may use entropy-based loss tracking as a tool to identify the measure of irreversibilities in a system and redesign such systems to minimize entropy production and optimize the system efficiency. This thesis focuses on the computation of local entropy production as a diagnostic energy loss tracking tool. The scope does not include redesigning thermofluid systems. An example of how entropy production minimization can be used to optimize the flow configurations such as nanoparticle volume fraction and velocity in a mixed convection system will be discussed.

This objective is generally applicable irrespective of the parameters of the system or flow configuration. Alternatively, this can be expressed in terms of the potential of a system to

produce useful work, which is known as “exergy”. For example, the cost of lost energy availability in a flow through a pipe can be estimated by multiplying exergy destruction in the flow by the cost of work input to the system (power for pumping the fluid). Through this approach, local entropy generation can be used in an economic framework, such as lost potential revenue from exergy destruction [2]. Overall, the entropy generation describes the degradation of mechanical energy to internal energy. It provides a valuable indicator for the assessment of energy efficiency for all energy-consuming or generating devices.

Entropy generation has both physical and computational characteristics. In addition to the physical processes of heat transfer and viscous dissipation, CFD models may destroy or produce false entropy through approximation errors that lead to non-physical numerical results, artificial dissipation, and other discretization errors [3-4]. Numerical simulations which do not satisfy a prescribed entropy constraint may yield non-physical results [5]. For example, the specific form of a convective upwinding scheme can be modified appropriately to satisfy entropy constraints and improve the overall accuracy of the model [3]. An entropy constraint was constructed based on alternate positive-definite and entropy transport forms of the Second Law using the Gibbs equation [6].

In this research, a Second Law formulation is presented and analyzed based on different forms of the positive-definite and entropy transport equations. In order to assess the numerical error, a new parameter called the “apparent entropy production difference” is computed based on the difference between the transport and positive-definite forms of the entropy production rate. A relationship between this difference and numerical errors in each control volume is developed and discussed. The “apparent entropy production difference”

is a useful parameter for characterizing errors in numerical solutions [7]. This parameter uses the Second Law to identify inconsistencies in numerical approximations which lead to anomalous results of the predicted entropy production. Also, a parameter known as entropy-based artificial viscosity is developed by using the entropy transport equation to calculate an artificial viscosity for a corrective mechanism in the numerical algorithm. This results in a significant reduction of the numerical errors in the algorithm by using entropy production to re-calculate the numerical viscosity according to the Second Law.

1.3 Entropy and Exergy Definitions

1.3.1 Definition of Entropy

From a second law perspective, the analysis of systems can be achieved in terms of the property entropy. A quantity that changes in value between two states which is independent of the process is known as a property [8]. The concept of property can be used together with the Clausius inequality to introduce a change in entropy. Consider two cycles implemented by a closed system as presented in Figure 1.1. One cycle is made up of an internally reversible process X from state 1 to state 2, succeeded by an internally reversible process Z from state 2 to state 1. Similarly, the other cycle comprises an internally reversible process Y from state 1 to state 2, succeeded by the same process Z from state 2 to state 1.

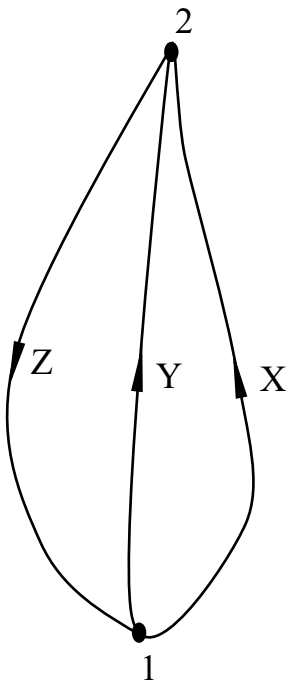

Figure 1-1: Two internally reversible cycles

For the first cycle, the Clausius inequality can be written in the form [8].

$$\left(\int_1^2 \frac{\delta Q}{T}\right)_X + \left(\int_2^1 \frac{\delta Q}{T}\right)_Z = -\sigma_{cycle} \tag{1.1}$$

The second cycle takes the form:

$$\left(\int_1^2 \frac{\delta Q}{T}\right)_Y + \left(\int_2^1 \frac{\delta Q}{T}\right)_Z = -\sigma_{cycle} \tag{1.2}$$

By setting the term σ_{cycle} to zero, since the cycle consists of internally reversible processes, and subtracting Equation (1.2) from Equation (1.1),

$$\left(\int_1^2 \frac{\delta Q}{T}\right)_X = \left(\int_1^2 \frac{\delta Q}{T}\right)_Y \tag{1.3}$$

This shows that for both processes the integral of δQ/T is the same. Since X and Y are arbitrary, it implies that the integral of δQ/T produces the same result for any internally reversible process between the two states. Hence, the value of the integral solely depends

on the end states. Therefore the integral denotes the change in certain property of the system. By using the symbol S to represent this property, which is known as entropy, the change in entropy is defined as:

$$S_2 - S_1 = \left(\int_1^2 \frac{\delta Q}{T}\right)_{\substack{int \\ rev}} \tag{1.4}$$

where the subscript "int rev" indicate that the integration is executed for any internally reversible process between the two states. On a differential basis, the entropy change defining expression takes the form:

$$dS = \left(\frac{\delta Q}{T}\right)_{\substack{int \\ rev}} \tag{1.5}$$

1.3.2 Definition of Exergy

Consider a given rigid body at a certain temperature T submerged in a thermal reservoir at some temperature T_o (for example, a hot piece of metal inside a cold room). Assuming $T > T_o$, the cooling process happens spontaneously until the solid body attains thermodynamic equilibrium with its environment. However, work can be developed by controlling the cooling. Instead of spontaneous cooling of the body, heat transfer can be passed to a power cycle to perform work, W_d. Such work can be used for executing shaft work, lifting a weight, or generating electricity.

Since the power cycle does not undergo any net change in state, the potential for producing work W_c arises only because the initial state of the body is different from that of the environment since $T > T_o$. Eventually, the body achieves thermal equilibrium with the environment. At equilibrium, the environment and the body each possess energy, but there is no more potential for work done from the two because further interaction can no longer

occur between them. Exergy represents the maximum theoretical value for the work, W_d. Maximum work is only achievable when there are no irreversibilities while the body cools to attain equilibrium with the environment.

In the case of spontaneous cooling to T_o, no work is obtained, hence, the initial potential to do work, exergy, is destroyed. The work W_d can also be developed when $T < T_o$. In this case, heat is transferred in the reverse direction, from the environment to the body and work is done as the body warms to reach equilibrium with the environment. As the previous case, the potential to do work arises solely because of the difference between the initial state of the body and that of the environment $(T < T_o)$.

Consider the Earth's atmosphere; a simple compressible system with an idealized temperature, T_o, and pressure, p_o, as the exergy reference environment. Exergy can be defined as the maximum theoretical work obtained from an overall system comprising of a body and its environment as the body comes into equilibrium with the environment.

The equilibrium state gives rise to the dead state; a state where the body is at p_o and T_o, and at rest with respect to the environment. At this state, there can not be any interaction between the body and its environment, hence, there is no potential to do work.

Using entropy and energy balances, the following equation is obtainable for the exergy of a system at a specified state [8],

$$E = (U - U_o) + p_o(V - V_o) - T_o(S - S_o) + KE + PE \tag{1.6}$$

where $E,\ U,\ V,\ S, KE, and\ PE$ refers to exergy, internal energy, volume, entropy, kinetic energy, and potential energy of the system, respectively. $U_o, V_o, and\ S_o$ represent, respectively, internal energy, volume, entropy of the system at the dead state.

1.4 Problem Definition

Based on a literature review, there are several shortcomings in the current state of knowledge in numerical heat transfer, which will be examined in this research. There is a need for a more robust local design methodology at a component level based on the Second Law of Thermodynamics. Designers of energy systems often adopt conventional approaches to evaluate the performance of a design based on global loss parameters or efficiencies. This method accounts for losses predicted over an entire system. However, the local values of available energy losses or entropy production can provide the designer with a more detailed insight than determining an end-to-end loss. The overall performance of thermofluid systems can be improved by modifying design parameters locally.

A literature review shows that there are few or no previous studies regarding entropy-based error methods in the analysis of natural and mixed convection heat transfer. So there is an opportunity for the development of a potentially new approach for numerical error characterization using entropy and the Second Law. This promising alternative approach to conventional error indicators would use the distribution and peak values of the apparent entropy production difference to predict trends in the solution errors for computational heat transfer and fluid flow.

Furthermore, there is also a need to better understand entropy production and heat transfer processes in natural and mixed convection problems with nanofluids. These could be used,

for example, to obtain the effects of nanoparticle volume fraction on heat conduction and entropy production. This research predicts the optimum nanoparticle volume fraction for which entropy production is minimized. This thesis will also extend these above methods to address physically implausible solutions and ensure positive entropy production in accordance with the Second Law.

1.5 Scope and Objectives

The scope and objectives of this research are briefly outlined as follows.

1. To develop a two-dimensional numerical model for the computation of entropy production, using positive-definite and transport forms of the entropy production equation, and apparent entropy production difference.
2. To develop and apply these numerical entropy generation models to natural and mixed convection heat transfer problems.
3. To validate the results from the numerical model with previously published benchmark data.
4. To conduct a numerical investigation of entropy production and heat transfer for natural and mixed convection in a rectangular enclosure filled with nanofluids and predict the effects of nanoparticle volume fraction on heat conduction and entropy production. Also, the research aims to predict the optimum nanoparticle volume fraction for which the entropy production is minimized.
5. To obtain a Second Law formulation that computes a new parameter called the "apparent entropy production difference" based on the difference between the transport and positive-definite forms of the entropy production rate. A relationship

between this difference and numerical errors in each control volume is developed and discussed.

6. To modify the algorithm in regions with physically implausible results to enhance the entropy production and compliance with the Second Law.

1.6 Outline of Thesis

This thesis outlines new analytical and numerical methods for entropy production analysis using the Second Law. Detailed numerical simulations involving entropy transport, energy and fluid flow equations will be performed using a Control-Volume Finite Element Method (CVFEM) and Finite Difference Method. Also, a new parameter known as the apparent entropy production difference will be obtained and used as entropy-based error indicator for fluid flow and thermal systems design improvement. A corrective mechanism will also be developed using an entropy-based artificial viscosity to improve the accuracy of the numerical model. The entropy and Second Law analysis is applied to various natural and mixed convection test problems involving different working fluids, including nanofluids. The numerical results of the simulations are validated against benchmark solutions.

In Chapter 2, a literature review for analytical, numerical, and experimental studies of entropy generation will be presented. Chapter 3 outlines the research methodology which features a generalized formulation for entropy production, fluid flow, and energy equations, and nanofluid properties. Chapter 4 presents results and discussion for the application of entropy and the Second Law to natural and mixed convection of nanofluids. Detailed analysis of the problem configuration is discussed. Chapter 5 examines entropy-based error

characterization in numerical heat transfer. The formulation of a new parameter (apparent entropy production difference) and its correlation with errors in numerical solutions is discussed. In Chapter 6, a new corrective mechanism is presented to minimize numerical errors and enhance system efficiency. Chapter 7 presents a general discussion and the thesis conclusions, with recommendations for further research.

Although the thesis is written as continuous text, it does have a feature of a paper-based thesis such as the repetition of a few geometries and mathematical models in the results chapters. This format is presented because a publication has been produced from each of the results chapters. Papers from Chapters 5 and 6 have already been published in journals, while Chapter 6 is in the process of submission for journal publication.

2 LITERATURE REVIEW

2.1 Overview

The concept of entropy has broad applications in several disciplines today, from thermodynamics and fluid mechanics to information and coding theory, biology, and economics. Entropy serves as an important parameter in attaining the highest limits of quality and performance in many engineering devices. Exergy and the Second Law are becoming increasingly important in achieving the upper theoretical limits in future technologies. They can shed more light on various flow processes, ranging from optimization of flow configurations in an aircraft engine to highly ordered crystal structures (low entropy) in a turbine blade, and many other applications [1,2].

An important application of entropy and the Second Law is flow design optimization of energy sub-systems, involving work-producing potential [9]. Entropy computations can track the work potential losses within the fluid flow and sub-system processes during a system's operation. With this information, the designer has a systematic means of identifying and targeting the regions incurring the most significant losses. Flow exergy can provide a valuable set of metrics and unifying framework for a more effective analysis of aircraft sub-systems [10,11]. Another example is entropy generation of fluid motion through a turbine. In this case, flow irreversibilities arise from fluid friction along the blades, tip or corner vortices and viscous mixing in the blade wakes, and other flow recirculations. The areas with the highest entropy generation, such as the wake, blade inception, and inlet regions, represent the regions where the most significant design

improvements can be made. Examples of design modifications to minimize entropy production include changes to inflow parameters (temperature, cooling mass flow rate), cooling holes (location, number, design), or geometric parameters (angles and blade shape, height) [2].

Entropy and Second Law have been used to compare the efficiency of various wind power systems. Exergy analysis can be used as a unified metric to compare a diverse range of operating and geometric designs. Through exergy methods, the turbine design and better site selection can improve the efficiency of a system and decrease costs [12]. Mamouri et al. [13] showed that entropy generation analysis of offshore wind turbine blades is useful for the design of the geometries of wind turbine blades. Entropy production can also be used as a diagnostic design tool to detect problematic areas in turbine operation, which require design changes. The energy losses at the turbine blade can be quantified by entropy generation analysis. Recommendations can be provided for future design modifications to reduce energy losses and increase the efficiency of the turbines [14].

2.2 Analytical Methods

Significant progress has been made in recent years towards the optimization of energy, fluid, and thermal systems using entropy and the Second Law. Part of this progress includes the development of various techniques for analytical approaches, such as: (i) minimization of entropy generation or available work through design modifications (called EGM; Method of Entropy Generation Minimization), and (ii) ideal theoretical operating conditions for a proposed design (called EA; Exergy Analysis) [15]. Exergy can be defined

as a thermodynamic property that measures the potential of an energy source to produce useful work. It quantifies the maximum potential of the energy system to produce useful work as it attains a specified final state of equilibrium with its environment. Exergy analysis aims to bridge the gap between the actual work produced by a device and exergy by a careful examination of the various thermodynamic processes involved in the energy conversion. Consequently, the values of exergy at every point are used to obtain the Second Law efficiencies which measure the system irreversibilities (or exergy destruction) produced by the energy conversion process [15, 16, 17].

To achieve the entropy generation minimization, the optimal configuration of geometry, heat transfer, material, and/or fluid motion, is required. In some cases, an analytical expression for the entropy generation in a process can be derived and minimized [1, 18, 19, 20]. This thesis will consider both numerical and analytical methods of entropy generation minimization.

2.3 Numerical Methods

The Second Law of Thermodynamics can be used for design optimization by incorporating Computational Fluid Dynamics (CFD) as a design tool in solving complex flow problems. Entropy generation is determined by post-processing of the computed flow fields [21]. CFD has been successfully used to solve many industrial problems arising in aerodynamics, energy storage, power generation, metallurgy, and other applications. It provides a designer with a time-saving and cost-effective approach for design optimization of engineering

systems. Local entropy production minimization with CFD provides additional design capabilities.

Natalini and Sciubba [22] presented a numerical method for the design of air-cooled gas turbine blades. A finite element method was used to solve the Navier-Stokes equations of motion and energy equation. The authors identified the entropy production rates corresponding to the heat transfer and fluid friction irreversibilities. They presented information for the assessment of different turbine blade configurations. By identifying the entropy generation rates corresponding to the fluid friction and heat transfer irreversibilities, the authors provided useful information for the assessment of different blade arrangements with optimal thermodynamic performance. The predicted flow fields with pitched turbine blades can be analyzed to identify areas of high exergy losses, thereby providing a direction to redesign the blade profile and minimize such losses and enhance the system performance [23].

Entropy generation predictions have also been used to find the optimal conditions for free convection in inclined cavities [24-27]. The results showed that the angle of inclination of the enclosure significantly affects the heat transfer effectiveness and flow behavior of the fluid. The optimum angle of inclination was obtained to ensure minimum entropy generation. Cheng et al. [28] predicted entropy production for mixed convection in a vertical enclosure with a transverse fin array. They presented results for various geometric and physical parameters and found an optimum geometric configuration of the finned channel with a higher level of second-law efficiency.

Entropy production for mixed convection in a flow inside concentric cylinder annuli with relative rotation was reported [29], the authors found that for the conduction regime, both the entropy generation number and the average Nusselt number are independent of the variation in Rayleigh number. In the convection dominated regime, the results showed an increasing trend for an increase in the Rayleigh number. The near-wall magnitude of overall entropy production rate is higher at a larger Rayleigh number, but the heat transfer irreversibility is higher at the center region of the cavity. Entropy production rates for laminar and turbulent flow through a channel were reported [30-32], Sahin [30] showed that the variation in viscosity has a significant effect on both the pumping power and entropy generation. The author also reported that the ratio of the pumping power to heat transfer and the entropy production per unit of heat transfer becomes large for low heat flux conditions. Demirel [31] found that the irreversibility is more uniformly distributed for a narrow-gap Couette flow. It was found that the assumption of a constant viscosity may yield a significant deviation in pumping power and entropy production results as compared with those with a temperature-dependent viscosity, specifically when highly viscous fluids are considered [32]. Numerical studies of entropy production have also been applied to various diffuser geometries [33]. Results suggested that an entropy-based approach provides a new way of establishing the optimum diffuser configuration with minimal flow losses.

Numerical studies of entropy production during natural convection have been applied to geological problems [34]. Chen and Du [35] reported turbulent double-diffusive free convection in a square cavity for various Rayleigh numbers, aspect ratios, and buoyancy

ratios. Their results indicated that the entropy generation rate increases with Rayleigh number, aspect ratio and buoyancy ratio. Also, the entropy generation due to heat transfer and mass transfer decreases with aspect ratio, whereas the entropy production due to fluid friction increases with aspect ratio. Mchirgui et al. [36] predicted the entropy production rate in double-diffusive convection in a differentially heated porous rectangular enclosure with horizontal concentration gradients. They found that the entropy production due to mass diffusion is larger compared to the local entropy production due to heat transfer and local entropy production due to fluid friction for Darcy numbers less than 10^{-3}. The irreversibilities due to heat transfer dominate over the fluid friction irreversibilities and mass diffusion for Darcy numbers of 10^{-3} and higher. Also, the total entropy production decreases with Darcy number.

Ruocco [37] studied entropy production of conjugate heat transfer from a flat plate to a laminar impinging planar jet involving air as the coolant fluid. The bottom plate is assumed an isothermal heater, while other surfaces were insulated. Their results showed that entropy generation is higher for air compared to that for water. The use of only one heater produced the minimum entropy production rate and higher rates of heat transfer for both air and water. Hidouri et al. [38] considered entropy generation in double-diffusive convection in a differentially heated rectangle cavity containing a binary gas mixture enclosed by impermeable vertical walls and permeable horizontal walls. They found that entropy production increases with the thermal Grashof number and buoyancy ratio. The minimum entropy production occurs at a specific buoyancy ratio between -1 and 0. The Soret effect reduces the rate of entropy production due to the concentration gradients.

CFD modelling of entropy production in natural convection has also been applied to building and ventilation systems. Ziapur and Dehnavi [39] considered entropy production in natural convection for a large triangular roof enclosure using a second law analysis. They reported that the entropy generation number is lower in the cavity with partial heating from the central region of the bottom wall compared to that of the cavity involving partial heating from the corner portion of the bottom wall. The entropy production number decreased with the aspect ratio of the large triangular-roof greenhouse. Varol et al. [40] examined natural convection entropy production in a partially cooled rectangular cross-sectional room with partially cooled sidewall windows and a uniformly heated floor. Results of computational fluid dynamics and the support vector machine are compared. The support vector machine is found to predict the entropy production with reasonable agreement.

A Second Law analysis in natural convection has also been reported for heat exchangers. You et al. [41] considered entropy production in thermal augmentation of horizontal pipes with a conical strip. Their results indicate that a non-staggered strip with an angle of 90° produced the least global total entropy production. The least global total entropy production is based on the optimal Reynolds number. Ko and Ting [42] performed a Second Law analysis of heat transfer in a helical coil with a constant heat flux wall in a fully developed convection. The authors reported that helical coils with a larger curvature ratio are more suitable for the low Reynolds number, while the smaller curvature ratio is suitable for the higher Reynolds number based on the minimum entropy production.

Rathnam et al. [43] studied natural convection entropy production within two entrapped triangular enclosures induced by a series of rectangular cross-sectioned tubes. The

entrapped enclosures were filled with porous media saturated with fluid. Their results showed that in the conduction dominant regime, the magnitudes of total entropy production are similar for both the hot entrapped fluid and cold entrapped fluid cases for all Prandtl number. At a high Darcy number, the total entropy production is a minimum for the cold entrapped fluid case within the upper triangle, whereas the total entropy generation is a minimum for the hot entrapped fluid case within the lower triangle at all Prandtl numbers.

Basak et al. [44] also considered natural convection entropy production within entrapped triangular enclosures. Their results showed less total entropy production and larger rates of heat transfer are observed in the lower triangle with hot entrapped fluid, and upper triangle containing cold entrapped fluid, especially for low Prandtl numbers and high Rayleigh numbers. Abu-Hijleh et al. [45, 46] studied natural convection entropy production from a heated isothermal cylinder placed horizontally in oil. The authors suggested that the viscous dissipation has a negligible effect on the local entropy production rates. The global total entropy production can be minimized by modifying the radius of the cylinder. Dagtekin et al. [47] examined the natural convection entropy production in a circular duct with various longitudinal fins of different shapes. They found that the entropy generation increases with the number of fins and decreases with the Rayleigh number for all shapes. The triangular fins with less length yielded the minimum entropy generation rate.

A Second Law analysis has been applied to packed beds by Demirel and Kahraman [48]. They considered convective heat transfer and entropy production in an annular packed bed, asymmetrically heated, with constant wall heat fluxes. Their results indicated that the entropy production due to fluid friction increases with an increase in packing, whereas the

addition of the packing reduces the entropy production due to heat transfer. The asymmetric thermal boundary condition produces less entropy production compared to the symmetric case. Demirel [49] examined natural convection entropy production in an asymmetrically heated square packed duct. A constant and asymmetric heat flux was assumed for the top and bottom walls, while the vertical walls were insulated. They reported that entropy production in each cross-section of the duct decreases with Reynolds number. The asymmetric heating is found to be most efficient for the packed bed in the convective regime when the entropy production is minimum.

Natural convection entropy production studies for cooling systems have also been reported. Shuja et al. [50] examined natural convection entropy production in a square enclosure with two heat generating porous blocks located at various positions. Their results indicated that the minimum entropy production due to heat transfer is found where the blocks are positioned vertically with reference to the central vertical axis. The optimum configuration of the block is determined by the configuration with the minimum total entropy production.

Shuja et al. [51] studied conjugate natural convection entropy production in a square enclosure bounded with adiabatic walls, which contain a steel heated block. Their results showed that the local entropy production due to heat transfer is lower when the solid body is positioned at the right top and left bottom corners of the enclosure. The larger entropy production due to fluid friction is observed when the solid body is positioned at the top right or lower left corner of the enclosure, whereas a negligible entropy production occurs where fluid friction is observed when the solid body is positioned at the center of the

enclosure. The global total entropy production is minimized when the solid body is positioned at the center of the cavity, and water is used as the coolant fluid.

Yang et al. [52] examined convective cooling of printed circuit boards with heat-generating chips. Their results indicated that the entropy production due to heat transfer and fluid friction are significant around the board surface and near the top surface of the chip at a larger aspect ratio. The increase in aspect ratio leads to an increase of the total entropy production due to heat transfer but a due to fluid friction.

The analysis of entropy production has been considered for thermal storage systems. Erek and Dincer [53] examined entropy production in a shell-and-tube latent heat storage system. Their results suggested that the entropy generation number is not considerably affected by the Reynolds number and tube length. A larger heat transfer rate was observed with the minimum entropy generation rate for the low shell radius at all Reynolds number. Flueckiger and Garimella [54] studied entropy production in a thermocline thermal energy storage tank with cyclic operation of a molten-salt system. They observed that the thermocline tank performance was improved by a reduction in the filler bed granule diameter. The external convection losses and reduction of efficiency of the thermocline tank is characterized by a larger entropy generation rate.

Second Law analysis of natural convection has also been reported for solar energy. Das and Basak [55] presented a study on natural convection entropy production during solar heating of triangular and square cavities. They found that a symmetric heater configuration is more efficient than asymmetric placements of heaters with lower entropy generation. Using the

minimum entropy production, the optimal configuration for all the cavities was obtained when the heaters along the sidewalls were centrally located. Ghachem et al. [56] examined three-dimensional double-diffusive free convection entropy generation in a solar distiller. Their results showed that entropy generation is minimized when the buoyancy ratio is equal to that for the solar distiller. Naphon [57] examined the entropy generation in a double-pass solar air heater with longitudinal fins. Their results indicated that entropy generation increases as the mass flow rate of air increases and decreases with the number of fins and the fin height. Biswal and Basak [58] performed a numerical study of natural convection entropy generation in right angled triangular cavities with curved surfaces whereby the right wall is exposed to solar energy. They reported that the structure with the concave right wall was optimal with respect to entropy generation for thermal processing of various fluids with solar heating on the curved wall.

Nasrin et al. [59] performed a numerical study of the performance of glass cover plate solar collectors with an absorber using Alumina/water nanofluids. Their results showed that the effects of higher Prandtl number on improving heat transfer effectiveness are higher in Al_2O_3 than the base fluid. The rate of convective heat transfer increases by 18% and 26% for water and Al_2O_3 – water, respectively. Risi et al. [60] analysed the performance improvement of a parabolic trough solar collector using (CuO+Ni) – nitrogen gas nanofluid. They obtained a maximum solar to thermal efficiency of 62.5%.

Tiwari et al. [61] studied the performance of a flat plate solar collector using Al_2O_3-Water nanofluids. They reported an increase in the thermal efficiency by 31.6% using 1.5% volume fraction of nanofluid. Risi et al. [62] examined the performance improvement of a

parabolic trough using Ni-water nanofluid. A thermal efficiency of 62.5% was reported. Tyagi et al. [63] also examined the performance of a non-concentrating microscale direct absorption solar collector using Al_2O_3-water nanofluid. Their results showed significant improvements in the efficiency of the solar collector for volume fractions less than 2%, while for a volume fraction higher than 2%, the efficiency remained nearly constant. The absolute efficiencies were found to be around 10% higher in the case of the nanofluid.

Rahman et al. [64] investigated heat transfer enhancement in circular solar collectors using multi-walled carbon nano-tube (MWCNT) – water nanofluids. Their findings indicated that the inclination angle and solid volume fraction have an important role in the improvement of the heat transfer and thermal efficiency of the collector. Sarkar [65] investigated the performance improvement of a flat plate solar collector using supercritical CO_2 – water nanofluids. An optimum enhancement in efficiency was found to be 18% as compared to water. Saidur et al. [66] examined a direct absorption solar collector for AL_2O_3 – water nanofluids. There was a significant improvement in solar absorption. The light absorption enhancement was observed at visible light and shorter wavelengths despite the low extinction coefficient. The volume fraction and extinction coefficient were linearly proportional. Said et al. [67] performed a Second Law analysis of a flat plate solar collector using single-wall carbon nanotube (SWNCT) – water nanofluids. They found that the SWCNT – water nanofluid can increase the heat transfer coefficient by 15.33% while reducing entropy generation by 4.34%.

Entropy production modelling has also been applied to compressible flows. Alipanah et al. [68] considered incompressible and compressible flow irreversibilities and entropy

production. Entropy generation during the incompressible flow was less than the compressible flow for the range of dimensionless temperature differences and Rayleigh numbers. Arshad et al. [69] studied entropy production of air flow through a diffuser. Their results indicated that entropy production near the diffuser wall is high, then decreases towards the center from the wall along the radial direction.

Entropy production modelling has also been reported for non-Newtonian flows. Yurusoy et al. [70] investigated the entropy production in a non-Newtonian fluid flow through annular tubes with a temperature-dependent viscosity. Their results showed that the non-Newtonian effects reduce the entropy production rate, whereas the viscosity increases the entropy production rate, especially in the region close to the inner wall of the annular tube. The minimum entropy production rate is achieved at a lower viscosity and higher non-Newtonian parameter.

Pakdemirli and Yilbas [71] examined entropy production in non-Newtonian fluid flow with a constant viscosity in the pipe system. They found that the non-Newtonian parameter reduced the fluid friction irreversibilities near the tube wall. The local entropy production due to fluid friction dominates over the entropy production due to heat transfer. The entropy production number increases from the center to an outer radial position in the pipe. The Brinkman number increases the total entropy production rates. Yilbas et al. [72] studied entropy production in non-Newtonian flow in an annular tube. Their findings suggest that the entropy production can be minimized when the Brinkman number is reduced.

Entropy production studies in natural convection involving the use of base fluids such as air, water, or oil are reported in [73 - 78]. Magherbi et al. [73] examined the entropy production due to heat transfer and fluid flow in transient laminar free convection for a square cavity with differentially heated sidewalls, filled with air (Pr = 0.71). They reported that the global total entropy production increases with Rayleigh number. Values at the onset of the steady-state are compared with the transient state and the minimum global total entropy production occurs at the steady-state.

Erbay et al. [74] examined the entropy production in a square cavity with differentially heated walls (cold vertical wall with a partially heated opposite vertical lateral wall). They observed that the maximum value of local total entropy production is significantly larger in the middle regions between the right and left walls for all irreversibility distribution ratios. The maximum value of the local total entropy production increases with Rayleigh number and Prandtl number, while the maximum value of the local total entropy production decreases with Rayleigh number at lower Prandtl numbera.

Yilbas et al. [75] investigated the entropy production in a square enclosure with different upper and lower wall temperatures. In this study, entropy production increased when fluid circulation along the x-axis increases. The entropy production is minimized at a particular Rayleigh number. Mukhopadhyay [76] studied the entropy production of free convection in an enclosure heated at the bottom by two discrete sources. The minimum entropy generation rate occurred for the same condition at which the peak heater temperature was minimized. Dagtekin et al. [77] analyzed the natural convection and entropy production in a circular duct with various longitudinal fins of different shapes. Here entropy generation

decreased with Rayleigh number and increased with the number of fins. The rate of entropy generation was less for the triangular fins with a shorter length. Mahmud et al. [78] reported the heat transfer and entropy production for free convection in a wavy-wall cavity with sidewalls at different temperatures. They presented an optimal case of the inclination angle and surface waviness that minimizes the entropy production for various aspect ratios. These examples showed how entropy generation computations can be successfully implemented with standard CFD solvers.

2.4 Entropy Production in Natural and Mixed Convection of Nanofluids

Entropy generation minimization for problems with natural convection has practical utility in the design of solar energy collectors, heat exchangers, thermal energy storage systems, and biomedical devices, among others. As discussed earlier, the rate of entropy production characterizes the degree of fluid friction and thermal irreversibilities. This section reviews past numerical modeling of entropy and the Second Law in natural and mixed convection problems with nanofluids.

Nanofluids are fluids that contain nano-scale particles with diameters of 1-100 nanometers (nm). These particles have unique thermophysical and chemical characteristics [79]. The use of air, water, or oil as a working fluid typically yields a relatively low thermal conductivity and heat transfer effectiveness [80-83]. Choi [79] has shown that the thermal performance can be enhanced significantly by the addition of nanoparticles with a higher thermal conductivity into a base fluid such as water, ethylene glycol, or oil to form a nanofluid. This can be advantageous for thermal engineering systems such as power

generation or heating and cooling systems [84]. Many past studies have been conducted on nanofluids, including various models, both theoretical and experimental, to determine their thermophysical properties, methods of preparation and applications [85-92].

Past studies have examined natural convection in enclosures filled with nanofluids. Hwang et al. [93] reported natural convection heat transfer enhancement in a square cavity containing Al_2O_3-water nanofluids. The authors discovered that nanofluids could significantly enhance the rates of heat transfer. Khanafer et al. [94] also examined the heat transfer in a square cavity filled with Cu-water nanofluids. The results indicated that the effects of heat transfer increase as the Cu nanoparticle volume fraction is increased in the working fluid. Sheikzadeh et al. [95] and Oztop and Abu-Nada [96] studied the natural convection of different nanofluids in a partially heated cavity. The temperature and flow fields were a function of position and length of the heat source. The free convection heat transfer effects of nanofluids in a differentially heated inclined enclosure were investigated by Abu-Nada and Oztop [25], Ghalambaz et al. [26], and Kahveci and Sadati [27]. The results showed that the angle of inclination of the enclosure significantly affects the heat transfer effectiveness and flow behavior of the nanofluid.

Relatively few past studies have examined the effects of nanofluids on entropy production rates. Shahi et al. [97] reported the entropy production due to natural convection cooling of a protruding heat source with Cu-water nanofluids in a square enclosure. The results showed an increase in the Nusselt number and a decrease in entropy production as the nanoparticle volume fraction increased. Li and Kleinstreuer [98] suggested that nanofluids are good coolants at a low nanoparticle volume fraction. An increase in nanoparticle

volume fraction reduces the entropy production at low Reynolds numbers with CuO-water nanofluids and pure water in trapezoidal microchannels. Singh et al. [99] performed a study of entropy production due to heat transfer and fluid friction of Al_2O_3-water nanofluids within different channel sizes and regimes. The effects of different models to calculate the viscosity and thermal conductivity of the nanofluid were reported. An optimal channel type was reported for which the entropy generation is minimized.

Moghaddani et al. [100] analyzed the entropy production due to ethylene, Al_2O_3-glycol, and Al_2O_3-water nanofluids in a circular pipe of constant heat flux. Increasing the nanoparticle volume fraction reduced the entropy production when the irreversibility due to heat transfer is dominant. They reported that the addition of the nanoparticles gives rise to a reduction in total entropy production for water-Al_2O_3 nanofluids in a laminar flow. In turbulent flow of water-Al_2O_3 nanofluids, the addition of the nanoparticles enhances the total entropy production for Reynolds numbers above 46,000 and reduces the total entropy production for lower Reynolds numbers. For laminar flow of ethylene glycol-Al_2O_3 nanofluid, the increase in nanoparticle volume fraction yields a higher total entropy production for Reynolds numbers above 14 and a reduction in total entropy production for Reynolds numbers below 11. The rate of entropy generation decreased with an increase in the nanoparticle volume fraction in a flow of Al_2O_3 -water nanofluids in a parallel disk [101].

Kashani et al. [102] examined natural convection entropy production in an enclosure with vertical wavy walls containing Cu-water nanofluid. Their results showed that the addition of nanoparticles to the base fluid decreases the total entropy generation. An enclosure with

concave type sidewalls was found to be the optimal case with a minimum entropy production rate and enhanced heat transfer for all Rayleigh numbers. Mahmudi et al. [103] investigated the entropy production in natural convection cooling of a heat source positioned inside the enclosure with a Cu-water nanofluid. Their results showed that the minimum entropy generation was used to identify the optimal configuration (where heater is positioned on the left wall at a distance of 0.4 m from the bottom wall). Khorasanizadeh et al. [104] studied natural convection entropy production in a Cu-water nanofluid within a cavity with a conductive baffle enclosed along the bottom hot wall. The authors identified an optimum baffle position for which the rate of entropy production is minimized.

Leong et al. [105] reported on natural convection entropy generation in a circular tube for water-base titanium dioxide and alumina nanofluids. Their findings indicated that titanium dioxide nanofluids produced less entropy compared to the alumina nanofluids. Natural convection Second Law analysis in a baffled L-shaped enclosure filled with water-alumina nanofluids was also reported [106]. The authors reported that the rate of entropy generation decreases with the irreversibility distribution ratio and dimensional ratio. An optimal baffle configuration was obtained.

Entropy production in conjugate free convection in a square enclosure filled with porous media saturated with a water-CuO nanofluid heated by a triangular solid in the lower left corner was also reported [107]. These results showed that entropy production increases with the irreversibility distribution ratio and thermal conductivity ratio in conjugate convection. The lowest wall thermal conductivity ratio and largest solid thickness are the optimum conditions based on the minimal value of the entropy production to heat transfer ratio.

Salari et al. [108] studied natural convection entropy generation in a differentially heated cuboid containing two immiscible liquid/gas fluids (carbon nanotubes-water nanofluid and air). They found that the total entropy production increases with the Rayleigh number and decreases with the nanofluid interface aspect ratio. The increase in irreversibility distribution ratio reduces the total entropy production. Cho [109] examined the effect of the magnetic field on entropy production in natural convection of Cu-water nanofluids in an enclosure involving wavy surfaces. It was reported that the total entropy production was almost constant with respect to the Hartmann number at a low Rayleigh number. At a high Rayleigh number, the total entropy production increases with the Hartmann number. The wave amplitude of the wavy surface increases with the total entropy production at a high Rayleigh number for the entire range of Hartmann numbers. Selimefendigil et al. [110] also considered the effects of a magnetic field in trapezoidal cavities containing nanofluids. Their results indicated that the entropy production decreases with the applied magnetic field and increases with the irreversibility distribution ratio. A decrease in the rate of entropy generation with the Hartman number is more evident in the lower enclosure compared to the upper enclosure.

Mamourian et al. [111] analyzed the entropy production in natural convection for water-Al_2O_3 nanofluid in a rectangular cavity with a constant axial magnetic field. The findings showed that the entropy production, at a specific Hartman number, increases with inclination angle of the enclosure until 30° after which there is a decreasing trend. The total entropy production increases with Rayleigh number for all Hartman numbers and inclination angles. Chamkha et al. [112] examined the natural convection entropy

generation for CuO-water nanofluid in a C–shaped enclosure under magnetic effects. They found that the rate of total entropy generation increases with the irreversibility distribution ratio. The applied magnetic field suppresses both the total entropy production rate and the natural convection effect.

Chen et al. [113] performed a Second Law analysis of double-diffusive natural convection in a differentially heated square enclosure containing SiO_2 – water nanofluid. They reported that the total entropy production is smaller for the laminar regime compared to the turbulent regime. The total entropy production decreases with the irreversibility distribution ratio. The total entropy generation is minimized at a buoyancy ratio of 1.

Cho et al. [114] investigated the natural convection entropy generation for an Al_2O_3-water nanofluid filled U-shaped cavity. Their results showed that as the irreversibility distribution ratio increases, the total entropy generation decreases, and the average Nusselt number increases. The total entropy generation and the average Nusselt number increase with the Rayleigh number. Also, an increase in the lengths of the cold walls results in a reduction of the total entropy production and an increase in the average Nusselt number.

Mahian et al. [115] studied the natural convection entropy generation for water-Al_2O_3 nanofluid in a flat plate solar collector. Their findings indicate that the entropy production is significantly lower for smooth pipes compared to that of rough pipes. The entropy production is found to decrease with the nanoparticle size for larger mass flow rates.

Cho et al. [116] performed a Second Law analysis of natural convection for Cu-water nanofluid and water in cavities with wavy sidewalls. It was reported that the Cu-water

nanofluid produced a minimum total entropy generation along with enhanced heat transfer performance. The authors showed that the mean Nusselt number can be maximized for a given nanofluid, while the total entropy production can be minimized by modifying parameters of the wavy surface geometry. Also, their results suggested that the natural convection heat transfer performance in wavy-wall cavity can be enhanced while simultaneously reducing the entropy production.

Alim et al. [117] analyzed the entropy production in a flat plate solar collector using CuO-water nanofluid. Their results showed a reduction in entropy production by 4.3% and heat transfer coefficient improvement by 22.1%. Parvin et al. [118] studied the heat transfer improvement and entropy production in a direct absorption solar collector for CuO-water nanofluid. Their findings indicated that the entropy generation and Nusselt number increase as the volume fraction of Cu nanoparticles particles and Reynolds number increases.

Mirzazadeh et al. [119] reported the entropy production of viscoelastic fluid flow through concentric rotating cylinders. Their results showed that the total entropy production number decreases as the fluid elasticity increases. The study also indicated that the entropy generation number increases with the Brinkman number. Mahian et al. [120] examined the entropy production due to heat transfer and fluid flow of nanofluids between cylinders. Their results demonstrated an optimum nanoparticle volume fraction for which the minimum entropy production rate was achieved.

In summary, this section reviewed past studies on numerical modeling of heat transfer enhancement, entropy generation and the Second Law application to natural and mixed

convection problems using nanofluids. The review shows that numerical modeling studies of natural and mixed convection heat transfer enhancement using nanofluids have been applied to a number of engineering problems including square cavities filled with fluid, heated cavity, inclined enclosures, and heat source optimization in enclosures. Also, entropy generation with nanofluids in natural convection has been studied in different applications such as optimization of microchannels, enclosures with concave sidewalls, heat source positions, baffle position, differentially heated cuboids with immiscible liquids, wave amplitudes of wavy surfaces, magnetic fields in trapezoidal cavities and C-shaped enclosures, U-shaped cavities, and solar collectors.

This study presents a new approach to the optimization of nanoparticle concentration for which entropy production is minimized. This thesis will focus on a numerical study of heat transfer and entropy production for natural and mixed convection in a rectangular enclosure filled with nanofluids. A case study will find an optimum nanoparticle volume fraction for which entropy production is minimized by modifying the moving wall velocity. The study also compares the natural convection heat transfer and entropy production for different nanofluids in the enclosure to determine the optimal nanofluid conditions in each system. An aspect ratio sensitivity analysis will also be performed.

2.5 Numerical Error Characterization

The numerical entropy production is a useful parameter for characterizing errors in numerical solutions [7]. This parameter uses the Second Law to identify inconsistencies in numerical approximations which lead to anomalous results of the predicted entropy

production. Entropy generation has both physical and computational characteristics. In addition to the physical processes of heat transfer and viscous dissipation, CFD models may destroy or produce false entropy through approximation errors. This can lead to non-physical numerical results, artificial dissipation, and other discretization errors [3,4]. If the differential equation solutions for the conservation of mass, momentum, and energy do not later satisfy the Second Law, the results may exhibit oscillations, lack of uniqueness, or other unusual attributes [121].

The total entropy generation predicted from a CFD formulation involves a sum of the physical and numerical entropy generation parts. Entropy is the measure of randomization or the degree of chaos, and this order can be represented in a physical sense and/or a computational sense. The physical characteristics of entropy which are the traditional view can be traced back to a lecture on the value of entropy relating to steam engine performance delivered by the mathematical physicist Rudolf Clausius in 1850 [3]. The computational characteristics of entropy are a relatively recent view which arose in the era of digital computers, and it examines entropy in terms of artificial dissipation, discretization errors, and implausible numerical results [5, 122-125]

This recent computational characteristic has considered connections between numerical stability, overall accuracy, solution uniqueness, and the second law. For example, a discrete entropy equation has been implemented to identify unique solutions and physical relevance in finite difference compressible flow modelling (Lax [122]). Also, the governing equations have been symmetrized through a change of entropy gradient variables to improve the performance of iterative algebraic solvers and stability. Merriam [124] has illustrated that

satisfaction of the second law is adequate, in some instances, to ensure computational stability of fluid flow.

This numerical stability suggests that entropy can serve as an effective parameter for solution convergence criteria. Furthermore, Camberos (7) has shown that entropy can be used as an effective measure of convergence and residual error because it defines a physically relevant quantity which is fully dependent on all fluid state variables. This essential attribute of the Second Law has a capacity to function as a physically based discretization error indicator which can identify physically unrealistic solutions in the CFD predictions. The promising potential of entropy production computations has been demonstrated in past applications. Entropy generation computations have been applied to numerical error, timestep constraints, and convergence criteria. It has been shown that a CFL condition of numerical stability (Courant, Freidrichs, and Lewy [126]) follows directly from the Second Law using the conditions of constant source terms and negligible diffusive transport. Source terms may impose more restrictive constraints on the timestep than a conventional CFL condition. The discretized entropy production equation can ensure nonlinear stability. It has been shown that a restrictive condition which involves a positive rate of entropy generation in each control volume can ensure numerical stability of the scheme [127].

Naterer and Schneider [5] presented numerical simulations to show that stable solutions which do not satisfy an entropy constraint yield inaccurate results. The Second Law can also be applied to improve the reliability of upwinding schemes. Numerical simulations which do not satisfy a prescribed entropy constraint may yield non-physical results [4]. The

specific form of a convective upwinding scheme can be modified appropriately to satisfy an entropy constraint and improve the overall accuracy of the model [3]. This entropy constraint is constructed based on positive-definite and entropy transport forms of the Second Law using the Gibbs equation. Errors in a numerical solution can be characterized by the magnitude of negative entropy generation which violates the Second Law [6]. With the possibility of entropy destruction due to numerical discretization, it becomes challenging to describe the generalized entropy generation without estimating the relative dimension of the actual (physical) entropy generation.

A non-negative numerical entropy generation may ensure a physically realistic solution and numerical stability. There is a need to quantify and prevent entropy destruction related with a numerical formulation. The entropy generation in a thermodynamic process can be obtained by using the entropy transport equation, which involves an inequality [6, 28, 127]. By using the Gibbs equation, which relates entropy to the mass, pressure, temperature, internal energy and density, another form of entropy production equation can also be obtained, which is positive-definite with a sum of squared terms [1]. Adeyinka and Naterer [7] presented a study that relates the generalized entropy production to a discrete error indicator for transient conduction in a solid material.

In summary, past studies showed that entropy production computations have been applied to timestep constraints, convergence criteria, and numerical error characterization. In terms of numerical error characterization, entropy generation models have been applied to compute discrete error for transient conduction in a solid material. One of the novel contributions of this work is the application of entropy generation computations as a

numerical error indicator in natural and mixed convection of fluids in square and lid driven cavities.

In this thesis, a Second Law formulation will be presented and analyzed based on different forms of the positive-definite and entropy transport equations. In order to assess the numerical error, a new parameter called the "apparent entropy production difference" will be developed based on the difference between the transport and positive-definite forms of the Second Law. A trend between this difference and numerical errors in each control volume will be discussed.

2.6 Entropy-Based Artificial Viscosity

The application of an "artificial viscosity" to solve the conservation equations was pioneered by von Neumann and Richtmyer [128]. The artificial viscosity refers to a numerical approximation of the fluid viscosity that achieves some prescribed objectives such as numerical stability. The concept of an artificial viscosity has been applied to several applications using different methods. Richtmyer [129] studied the use of artificial viscosity to stabilize shock waves in a finite difference method. Wilkins [130,131] reported an artificial viscosity in HEMP (Hydrodynamic, Elastic, Magneto, and Plastic) problems. An artificial viscosity has also been related to large eddy simulations. Smagorinsky [132,133] reported that the eddy viscosity can be related to the von Neumann–Richtmyer artificial viscosity. Nazarov and Hoffman [134] studied a residual-based artificial viscosity for modelling of turbulent compressible flow, based on a posteriori error estimation. The artificial viscosity was used in shock capturing, turbulence capturing, and as a numerical

stabilization for large eddy simulation of turbulent flow. The adaptive method addressed parts of the flow highlighted by posteriori error estimates, but left turbulence and shocks under-resolved in a large eddy simulation.

Albright and Shashkov [135] proposed a new technique for constructing an adaptive, artificial viscosity in one-dimensional, staggered-grid Lagrangian hydrodynamics. Their result demonstrated that a new adaptive technique produces more accurate results for a variety of tests with propagating shock waves. A higher order, state-based artificial viscosity method, associated with a governing partial differential equation, was proposed by Barter and Darmofal [136]. When applied to heat transfer problems on unstructured grids in hypersonic flows, they found that the artificial viscosity was less susceptible to numerical errors, thereby enabling more accurate heat transfer predictions.

Hartmann [137] introduced an artificial viscosity for stabilization of numerical solutions at with large local residuals while preserving conservation and orthogonality of the discontinuous Galerkin method. The authors derived a posteriori error estimates for the measured errors in terms of target functionals of an airfoil immersed in a flow field. Kolev and Rieben [138] obtained an artificial viscosity for a Lagrangian-Eulerian hydrodynamics model using a finite element approach. The authors reported improved numerical results with the model. Persson and Peraire [139] presented a shock-capturing method for higher order discontinuous Galerkin approximations of conservation laws. They showed how the artificial viscosity could be used to eliminate high frequencies in a solution and enhance stability.

Yechel et al. [140] studied the use of an upwind symmetric interior penalty Galerkin (SIPG) method for convection-diffusion-reaction modelling with nonlinear reaction mechanisms. They reported that the addition of an artificial viscosity term minimizes the local spurious oscillations. Reisner et al. [141] introduced a new method for adding space–time smoothing by a localized artificial viscosity in the nonlinear systems of conservation equations involving rarefactions, shock waves, and contact discontinuities.

Guermond et al. [142] presented a high-order entropy viscous method for approximating the nonlinear conservation laws. A nonlinear viscosity based on the local entropy production was added to the numerical discretization. The entropy viscosity method was applied to the one-dimensional Euler equations for a continuous finite element discretization in the MOOSE (Multi-Physics Object Oriented Simulation Environment) framework. Their method added dissipative terms to the governing equations, where a viscosity coefficient regulates the amount of dissipation. Their results indicated that the model can accurately resolve shocks and efficiently smooth out oscillations [143]. Chaudhuri et at. [144] proposed a spatio-temporal adaptive artificial viscosity-based shock-capturing scheme for the solution of both viscous and inviscid compressible flows using a Discontinuous Spectral Element Method (DSEM). They reported that artificial thermal conduction and artificial viscosity coefficients are proportional to the thermal and viscous entropy generating terms, respectively.

In summary, previous studies indicate that the concept of artificial viscosity has been applied to shock wave stabilization in a finite difference method and HEMP (Hydrodynamic, Elastic, Magneto, and Plastic) problems, modelling of turbulent

compressible flow based on a posteriori error estimation, error analysis in terms of target functionals of an airfoil immersed in a flow field, Lagrangian-Eulerian hydrodynamic modelling using a finite element approach, shock-capturing methods for higher order discontinuous Galerkin approximations of conservation laws, upwind symmetric interior penalty Galerkin (SIPG) methods for convection-diffusion-reaction modelling, adding space–time smoothing by a localized artificial viscosity in nonlinear systems of conservation equations, modelling of one-dimensional Euler equations for a continuous finite element discretization in the MOOSE (Multi-Physics Object Oriented Simulation Environment) framework, and a spatio-temporal adaptive artificial viscosity-based shock-capturing scheme for the solution of both viscous and inviscid compressible flows using a Discontinuous Spectral Element Method (DSEM).

Based on this previous literature review, and to the best of the author's knowledge, no past studies have considered the application of entropy-based artificial viscosity which is based on a Control Volume Finite Element Method (CVFEM) to improve numerical accuracy, particularly in natural and mixed convection heat transfer problems. Therefore, one of the goals of this thesis is to develop a new corrective mechanism for numerical algorithms, using the entropy transport entropy to calculate an artificial viscosity. This will be called an entropy-based artificial viscosity to ensure positive (or minimally negative) entropy production and thereby enhance the accuracy of the numerical model.

3 METHODOLOGY

This chapter presents a detailed description of the procedures for implementing the models of entropy production and the Second Law. The first section discusses the general scalar conservation equation, which includes the general transport equation, and conservation of mass, momentum, and energy. The second section describes the formulation of entropy generation and the Second Law of Thermodynamics. The third section of this chapter presents the numerical formulation, procedure, geometric discretization, and the local-global coordinate transformations, relevant to the application of the conservation law to the discretization of the governing equations.

The formulation specifically considers incompressible flow and natural / mixed convection problems with constant thermophysical properties, involving a Newtonian fluid. It is assumed that the buoyancy induced flow is two-dimensional and that a Boussinesq approximation can be used to evaluate the density variation in the buoyancy term.

Heat transfer in buoyancy induced flow in cavities occurs in various engineering applications. For example, solar thermal collectors, cooling of microelectronic assemblies, and heating/ventilation in buildings involves free convection. A nuclear reactor core surrounded by gas-filled cavities, and heat transfer between glass panes in double-pane windows, are other examples. Though the physical processes of natural convection have been widely published in the literature, only a few studies have considered the importance of irreversibilities in such systems.

A specified heat transfer rate can be achieved, but with different measures of fluid irreversibilities, based on the temperature difference and surface area across which heat

transfer occurs. For instance, convective cooling of a microelectronic component involves natural convection from the heat sink, however, pressure losses occur due to forced convection of air through internal components. In this case, each unit of entropy generated (or exergy destroyed) results in a corresponding measure of heat flow which is supposed to be removed from the system but cannot be removed as a result of entropy production. This entropy generation leads to kinetic energy dissipated to internal energy and pressure losses which work against the objective of component cooling [7].

3.1 General Scalar Conservation Equation

Consider a general scalar quantity, ϕ, such as velocity, temperature, or concentration, transported throughout a flow field by convection and diffusion. The velocity as a general scalar quantity refers to each of the individual Cartesian velocity components (u, v). The general two-dimensional scalar conservation equation can be written as [145]:

$$\frac{\partial(\rho\phi)}{\partial t} + \nabla \cdot (\rho \boldsymbol{v}\phi) - \nabla \cdot (\Gamma \nabla\phi) = \dot{P} \tag{3.1}$$

The first term on the left-hand side of Equation (3.1) refers to the transient storage term and the second term represents the convective flux. The third term on the left-hand side is the diffusive flux. The term on the right-hand side represents internal or external source terms. In the formulation of Equation (3.1), both $\dot{P}$ and Γ are generalized parameters representing the source terms and diffusion coefficient, respectively. For example, Γ could refer to viscosity, conductivity, etc. depending on the conserved quantity being considered. Also,

terms that cannot be expressed through the diffusion and convection terms (such as the pressure gradient) are included within the source term.

Assume a Newtonian fluid, incompressible flow with constant thermophysical properties. The buoyancy induced flow is two-dimensional and the Boussinesq approximation is used to evaluate the density variation in the buoyancy term [146]. Under these assumptions, the corresponding governing equations for the conservation of mass, momentum (Navier-Stokes equations), and energy equations are written as follows [146]:

$$\frac{\partial u}{\partial x} + \frac{\partial v}{\partial y} = 0 \tag{3.2}$$

$$\rho\left[\frac{\partial u}{\partial t} + u\,\frac{\partial u}{\partial x} + v\,\frac{\partial u}{\partial y}\right] = -\frac{\partial p}{\partial x} + \mu\left(\frac{\partial^2 u}{\partial x^2} + \frac{\partial^2 u}{\partial y^2}\right) \tag{3.3}$$

$$\rho\left[\frac{\partial v}{\partial t} + u\,\frac{\partial v}{\partial x} + v\,\frac{\partial v}{\partial y}\right] = \rho\beta g(T - T_c) + \mu\left(\frac{\partial^2 v}{\partial x^2} + \frac{\partial^2 v}{\partial y^2}\right) \tag{3.4}$$

$$\rho C_p\left[\frac{\partial T}{\partial t} + u\,\frac{\partial T}{\partial x} + v\,\frac{\partial T}{\partial y}\right] = k\left(\frac{\partial^2 T}{\partial x^2} + \frac{\partial^2 T}{\partial y^2}\right) \tag{3.5}$$

where u and v are the horizontal and vertical component velocities, respectively, ρ denotes the density, p is the pressure, μ refers to the dynamic viscosity, β is the thermal expansion coefficient, g is the gravitational acceleration, T is temperature, C_p represents the specific heat capacity, and k is the thermal conductivity.

The Boussinesq approximation neglects density differences except where they appear in terms multiplied by the acceleration due to gravity, g. The Boussinesq approximation is relevant to problems where the fluid temperature varies from one region to another, driving fluid flow and heat transfer. In buoyancy driven flow, the pressure is a function of

longitudinal axis only, therefore, the pressure gradient in the horizontal direction inside the boundary layer is hydrostatic in the cold wall boundary of the fluid [146].

$$\frac{\partial p}{\partial y} = -\rho_c g \tag{3.6}$$

By substituting Equation (3.6) into the momentum equation, and defining the thermal expansion coefficient as:

$$\beta \approx -\frac{1}{\rho}\left(\frac{\rho_c - \rho}{T_c - T}\right) \tag{3.7}$$

Then the body force term in the vertical momentum equation is approximated as

$$(\rho_c - \rho)g \approx \rho\beta g(T - T_c) \tag{3.8}$$

Hence, Equation (3.4) represents the Boussinesq form of the momentum equation, which includes the coupling between the flow field and the temperature field.

3.2 Formulation of Entropy Production

3.2.1 Positive-Definite Entropy Generation Equation

Entropy is a scalar quantity that is transported by fluid and heat flow, similar to the transport of mass, momentum, and energy; however, with an exception that entropy is not a conserved quantity. It is generated by irreversible processes such as fluid friction and heat transfer. The entropy generation can be represented in terms of the total derivative of entropy of a fluid element with respect to time (temporal and convective components) and entropy flux due to heat transfer [1]:

$$\dot{P}_S \equiv \frac{\partial S}{\partial t} + \boldsymbol{\nabla} \cdot \boldsymbol{F} \geq 0 \tag{3.9}$$

where $\dot{P}_s$ refers to the rate of entropy production and $S = \rho s$ is the entropy per unit volume. The entropy flux can be written in terms of the heat flux and velocity field as follows:

$$\boldsymbol{F} = \rho \boldsymbol{v} s + \boldsymbol{q}/T \tag{3.10}$$

where s is the specific entropy. The specific entropy, s, is determined from the Gibbs equation as follows:

$$ds = \frac{1}{T} de + \frac{p}{\rho^2 T} d\rho \tag{3.11}$$

where e represents the internal energy per unit mass, p refers to the pressure and ρ is the density. By integrating the Gibbs equation between two state points, the change in specific entropy can be expressed as

$$\Delta s = \int_{T_r}^{T_t} C_v \frac{dT}{T} + \int_{\rho_r}^{\rho_t} \frac{p}{\rho^2 T} d\rho \tag{3.12}$$

where the subscripts *r* and *t* represent a reference state and the current state, respectively. The variable C_v denotes the specific heat, which is assumed to be constant. This formulation is limited to incompressible gas or liquid flows over small or moderate temperature differences.

For an incompressible fluid, Equation (3.12) becomes:

$$\Delta s = s - s_r = C_v \ln\left(\frac{T_t}{T_r}\right) \tag{3.13}$$

For an ideal gas,

$$s = C_v \ln\left(\frac{T_t}{T_r}\right) - R \ln\left(\frac{\rho_t}{\rho_r}\right) + s_r \tag{3.14}$$

Substituting the ideal gas law into Equation (3.14),

$$s = C_v \ln\frac{(p_t/p_r)}{(\rho_t/\rho_r)^\gamma} + s_r = C_v \ln\left(\frac{p^*}{\rho^{*\gamma}}\right) + s_r \tag{3.15}$$

where γ refers to the ratio of the specific heats. When combined with the Gibbs equation, the entropy transport equation provides a way of evaluating the local entropy production for an open system. Alternatively, the entropy generation rate can be formulated as [1]:

$$\dot{P}_s = \frac{k}{T^2}\left(\frac{\partial T}{\partial x_i}\right)^2 + \frac{\tau_{ij}}{T}\frac{\partial u_i}{\partial x_j} \geq 0 \tag{3.16}$$

where k denotes the thermal conductivity and τ_{ij} represents the viscous stress due to velocity gradients in the fluid flow,

$$\tau_{ij} = \mu\left[\left(\frac{\partial u_i}{\partial x_j} + \frac{\partial u_j}{\partial x_i}\right) - \frac{2}{3}\frac{\partial u_k}{\partial x_k}\delta_{ij}\right] \tag{3.17}$$

Here μ refers to the dynamic viscosity and δ_{ij} is the Kronecker delta. Under the assumption of incompressibility, the divergence term in Equation (3.17) will disappear.

In Equation (3.16), Fourier's law has been used to represent heat conduction. In addition, the fluid was assumed to be Newtonian for the viscous stress term. As a result of these models, Equation (3.16) becomes a positive-definite equation for the rate of entropy generation, as it represents a sum of squared terms. The positive-definite expression applies

to both incompressible and compressible Newtonian fluids. The temperature, T, is expressed in absolute (Kelvin) units.

The resulting form of the positive-definite equation for the rate of entropy production can be expressed as

$$\dot{P}_{s,pd} = \frac{k}{T^2}\left[\left(\frac{\partial T}{\partial x}\right)^2 + \left(\frac{\partial T}{\partial y}\right)^2\right] + \frac{\mu}{T}\Phi \geq 0 \tag{3.18}$$

where Φ refers to the viscous dissipation rate due to the velocity gradients in the fluid motion. The first term in Equation (3.18) represents the entropy production due to heat transfer across the temperature difference in the fluid. The second term refers to the local entropy production due to viscous dissipation. This inequality form of the Second Law is known as the positive-definite entropy equation because it consists of a sum of squared terms which, therefore, must yield a positive-definite result. The equation is obtained by combining the differential transport equations for thermal energy and mass with the Gibbs equation. The viscous dissipation, Φ, is defined as

$$\Phi = \left(\frac{\partial u}{\partial y} + \frac{\partial v}{\partial x}\right)^2 + 2\left(\frac{\partial u}{\partial x}\right)^2 + 2\left(\frac{\partial v}{\partial y}\right)^2 \tag{3.19}$$

The inequality in Equation (3.18) confirms that entropy is produced for irreversible processes according to the Second Law,

$$\dot{P}_s \geq 0 \tag{3.20}$$

The inequality holds for irreversible processes, while the equality applies to reversible processes.

For a nearly isothermal process, the entropy generation due to thermal irreversibilities is neglected. As a result, the entropy production equation, representing the contribution from viscous dissipation alone to flow irreversibilities, can be expressed by the second term on the right-hand side of Equation (3.18),

$$\dot{P}_{s,pd} = \frac{\mu}{T}\left[\left(\frac{\partial u}{\partial y} + \frac{\partial v}{\partial x}\right)^2 + 2\left(\frac{\partial u}{\partial x}\right)^2 + 2\left(\frac{\partial v}{\partial y}\right)^2\right] \geq 0 \tag{3.21}$$

In the numerical model, the local entropy production can be computed based on post-processing of the velocity and temperature fields to determine their spatial gradients.

Equation (3.18) can be expressed in a non-dimensional form by defining the following dimensionless parameters:

$$U = \frac{uH}{\alpha},\ V = \frac{vH}{\alpha},\ X = \frac{x}{H},\ Y = \frac{y}{H},\ \theta = \frac{T - T_c}{T_h - T_c} \tag{3.22}$$

$$\dot{P}_S^* = \left[\left(\frac{\partial \theta}{\partial X}\right)^2 + \left(\frac{\partial \theta}{\partial Y}\right)^2\right] + \varphi\left[2\left(\frac{\partial U}{\partial X}\right)^2 + 2\left(\frac{\partial V}{\partial Y}\right)^2 + \left(\frac{\partial U}{\partial Y} + \frac{\partial V}{\partial X}\right)^2\right] \tag{3.23}$$

$$\varphi = \frac{\mu T_o}{k}\left(\frac{\alpha}{L(T_h - T_c)}\right)^2,\quad T_o = \frac{T_h - T_c}{2} \tag{3.24}$$

where φ is the ratio of the viscous and thermal irreversibilities, and T_o is a reference temperature. The total entropy production ($\dot{P}_{s,t}^*$) is obtained by integration of the local entropy production $\left(\dot{P}_s^*\right)$ over a control volume, *V*,

$$\dot{P}^*_{s,t} = \int_V \dot{P}^*_s dV \tag{3.25}$$

The values of entropy production are obtained based on the spatial derivatives of temperature and velocity calculated within the control volume. A piecewise linear profile will be assumed for the temperature and velocity derivatives inside the control volume. The local rate of entropy generation will be approximated as the average local rate of entropy produced within a control volume.

3.2.2 Entropy Transport Equation

According to the Second Law, the rate of entropy production is either zero (for reversible processes) or positive (for irreversible processes) for an isolated system. Processes such as heat transfer, chemical reactions, and friction are irreversible because the state of the system and its environment following the process cannot be returned to their initial thermodynamic state without energy expenditure. Entropy is a scalar quantity that is transported by heat and fluid flow, similar to the mass, momentum, and energy equations. The entropy balance for a differential control volume can be written as:

$$\rho \frac{\partial s}{\partial t} + \rho u \frac{\partial s}{\partial x} + \rho v \frac{\partial s}{\partial y} = -\boldsymbol{\nabla} \cdot \left(\frac{\boldsymbol{q}}{T}\right) + \dot{P}_S \tag{3.26}$$

The first term on the left side is the change in entropy of a fluid element with respect to time; the second and third terms on the left side represent the change in entropy with respect to space; and the first and second terms on the right-hand side denote the entropy flux due to heat flow and the rate of entropy production, respectively. This results in Equation (3.27), which is a “transport form” of the Second Law,

$$\dot{P}_{s,te} = \rho \frac{Ds}{Dt} + \boldsymbol{\nabla} \cdot \left(\frac{\boldsymbol{q}}{T}\right) \tag{3.27}$$

where $\frac{D}{Dt}$ refers to the total or substantive derivative including both temporal and convective components.

Another useful form can be obtained if the Gibbs equation and Fourier's law are used to rewrite Equation (3.27) in terms of temperature as follows:

$$\dot{P}_{s,T} = \frac{\rho C_p}{T} \frac{DT}{Dt} - \frac{k}{T} \left(\frac{\partial^2 T}{\partial x^2} + \frac{\partial^2 T}{\partial y^2}\right) \geq 0 \tag{3.28}$$

From the Second Law, the right side of Equation (3.28) must be equal or greater than zero. However, negative entropy production due to numerical discretization may be obtained due to approximation errors. Any negative entropy production is anticipated to lead to physically unrealistic results that violate the Second Law. This could offer a valuable insight into the physical viability of numerical predictions when experimental data is unavailable to validate the simulation results.

3.2.3 Apparent Entropy Production Difference

Two distinct formulations of the entropy production have been derived in the previous sections: positive-definite and transport equation forms of the Second Law. The two models can be computed independently from each other, for example, Equation (3.18) can be obtained by post-evaluation of the temperature and velocity fields from the momentum and energy equations, while Equation (3.27) can be calculated from an entropy balance and the Gibbs equation. The positive-definite form represents a sum of squared terms and an

inequality, which necessarily complies with the Second Law, but on the other hand, the transport form is obtained from an entropy balance within a control volume that is subject to numerical approximation errors and does not enforce a positivity requirement. The two different forms of the entropy generation rate will be represented by the subscripts "pd" and "te" for the positive-definite and transport forms, respectively.

Ideally, both forms of the Second Law should produce the same results for the entropy production rate. However, in practice, they may produce different results since they are computed separately and independently of each other using different procedures of numerical approximations. Therefore, the difference between the two forms of entropy expressions may be nonzero. The underlying hypothesis of this work proposes to characterize the error in the numerical solution with respect to this apparent entropy production difference. By subtracting Equation (3.18) from Equation (3.27), and using the quotient rule of calculus to combine and cancel temperature derivative terms, the following expression for the "apparent entropy production difference" is obtained,

$$\Delta \dot{P}_s = \dot{P}_{s,te} - \dot{P}_{s,pd} = \rho \frac{Ds}{Dt} - \frac{k}{T}\left[\frac{\partial^2 T}{\partial x^2} + \frac{\partial^2 T}{\partial y^2}\right] - \frac{\Phi}{T} \tag{3.29}$$

The apparent entropy production equation can be normalized as follows:

$$\Delta \dot{P}_{s,n} = \frac{\Delta \dot{P}_s - \Delta \dot{P}_{s,min}}{\Delta \dot{P}_{s,max} - \Delta \dot{P}_{s,min}} \tag{3.30}$$

The difference between the two forms of the entropy expressions would ideally be zero in an exact solution. However, in practice, numerical approximation errors may produce a nonzero apparent entropy production difference. In the case of the entropy transport equation, such errors may also yield negative computed entropy production rates, since

there is no enforced positivity requirement, and hence potentially non-physical results due to a local violation of the Second Law. Approximation errors through the numerical discretization may lead to a nonzero apparent entropy difference. Therefore, the importance of the apparent entropy production difference lies in its ability to potentially characterize the solution error differently or more accurately than conventional approaches such as grid refinements in the absence of experimental data to confirm the numerical model's accuracy. The discretization errors and implausible solution behavior in the numerical results may lead to local violations of the Second Law. This means that potentially in some control volumes, the rate of entropy production is less than zero, $\left(\dot{P}_s\right)_j < 0$. If there exists a local violation of the Second Law, then a quantitative indication of the artificial viscosity is required to correct the solution [2]. In section 3.2.4, an entropy-based artificial viscosity is formulated using the Prandtl number with a previous transport entropy production equation to implement an algorithm corrective mechanism for numerical accuracy improvement.

3.2.4 Entropy-Based Artificial Viscosity

As discussed previously, negative entropy production due to numerical discretization may be obtained due to approximation errors. Any negative entropy production is anticipated to lead to physically unrealistic results that violate the Second Law. This could offer a valuable insight into the physical viability of numerical predictions when experimental data is unavailable to validate the simulation results. The post-processed temperature results can be used to obtain their physical plausibility based on the sign (positive or negative) predicted by Equation (3.28) and magnitude of the predicted entropy production difference. If the predicted rate of entropy production is negative due to discretization approximation

errors, and/or nonzero entropy production differences occur, then this provides a useful indicator for physical unrealistic results due to numerical discretization errors.

A corrective mechanism on the numerical algorithm is developed herein. The transport form of the entropy production will be used to calculate a parameter called an entropy-based artificial viscosity, which is obtained by remodeling of the diffusion coefficient in the momentum conservation equations to reduce the numerical error in the algorithm as well as compliance with the Second Law. This modification of the algorithm also ensures that the transport entropy production is no longer negative (or minimally negative).

From equation (3.18), the entropy-based artificial viscosity can be obtained as:

$$\mu_e = \frac{|\dot{P}_{s,te}|}{\left[\left(\frac{C_p \nabla T.\nabla T}{PrT^2}\right)+\left(\frac{\Phi}{T}\right)\right]} \tag{3.31}$$

where μ_e is the entropy-based artificial viscosity. The Prandtl number is defined as:

$$Pr = \frac{\mu C_p}{k} \tag{3.32}$$

and

$$\nabla T.\nabla T = \left(\frac{\partial T}{\partial x}\right)^2 + \left(\frac{\partial T}{\partial y}\right)^2 \tag{3.33}$$

The momentum conservation equations (3.3 and 3.4) become:

$$\rho\left[\frac{\partial u}{\partial t} + u\,\frac{\partial u}{\partial x} + v\,\frac{\partial u}{\partial y}\right] = -\frac{\partial p}{\partial x} + \left[\frac{|\dot{P}_{s,te}|}{\left[\left(\frac{C_p \nabla T.\nabla T}{PrT^2}\right)+\left(\frac{\Phi}{T}\right)\right]}\right]\left(\frac{\partial^2 u}{\partial x^2} + \frac{\partial^2 u}{\partial y^2}\right) \tag{3.34}$$

$$\rho\left[\frac{\partial v}{\partial t}+u\ \frac{\partial v}{\partial x}+v\ \frac{\partial v}{\partial y}\right]=-\frac{\partial p}{\partial y}+\rho\beta g(T-T_c)+\left[\frac{|\dot{P}_{s,te}|}{\left[\left(\frac{C_p\nabla T.\nabla T}{PrT^2}\right)+\left(\frac{\Phi}{T}\right)\right]}\right]\left(\frac{\partial^2 v}{\partial x^2}+\frac{\partial^2 v}{\partial y^2}\right)$$

(3.35)

The positive-definite entropy production in Equation (3.18) is greater or equal to zero, whereas the transport form of the entropy production equation may be negative. Therefore, the absolute value of the transport entropy production is used in Equation (3.31). A conventional approach would solve the momentum equations using the dynamic viscosity without consideration of the Second Law. However, the proposed entropy-based approach uses results from the Second Law to return and iteratively adjust the diffusion coefficient to ensure closer compliance with the Second Law. Sample pseudo-code for the conventional and modified algorithm steps are presented as follows

Conventional algorithm

For loop *i* = 1 to n

Solve mass equation

Solve momentum equation

Solve energy equation

End loop

Solve entropy equations $(\dot{P}_{s,pd}, \dot{P}_{s,te})$

(Based on post-processed u – velocity, v – velocity, and temperature)

Iterate until pressure/velocity converges

Entropy-based artificial viscosity correction

For loop i = 1 to n

Solve mass equation

Solve momentum equation

Solve energy equation

Solve entropy equations $(\dot{P}_{s,pd}, \dot{P}_{s,te})$

Calculate artificial viscosity, μ_e

Repeat until $\dot{P}_{s,te} \gtrsim 0$

End loop

In addition to the pressure/velocity convergence in the conventional algorithm, the corrective entropy-based algorithm adds a further convergence criterion that the transport entropy production should be approximately greater or equal to zero.

3.3 Numerical Formulation

A CVFEM (Control Volume Based Finite Element Method) will be used for discretization of the governing equations [141]. Each control volume is formed around the nodal points by assembling sub-control volumes from the neighbouring adjacent elements. The domain is subdivided into linear quadrilateral finite elements. The CVFEM uses a local coordinate system (s, t) with shape functions as well as other element properties, as shown in Figure

3.1. The sub-control volumes and sub-surfaces of the surrounding elements define the control volume. The sub-surfaces refer to the boundaries of the control volumes, which overlap with the external boundaries of the element. The discretized conservation equations are obtained by integrating the governing equations over the finite control volumes and time steps. The midpoint of a sub-surface is denoted by an integration point (ip).

The geometry and general scalar variable, ϕ (such as velocity or temperature), at a given point within the element can be obtained in terms of nodal values as follows:

$$x = \sum_{i=1}^{4} N_i x_i \tag{3.36}$$

$$y = \sum_{i=1}^{4} N_i y_i \tag{3.37}$$

$$\phi(s,t) = \sum_{i=1}^{4} N_i(s,t)\Phi_i \tag{3.38}$$

where Φ refers to the local nodal values and $N_i(s,t)$ are the shape functions defined as:

$$N_1(s,t) = \frac{1}{4}(1+s)(1+t) \tag{3.39}$$

$$N_2(s,t) = \frac{1}{4}(1-s)(1+t) \tag{3.40}$$

$$N_3(s,t) = \frac{1}{4}(1-s)(1-t) \tag{3.41}$$

$$N_4(s,t) = \frac{1}{4}(1+s)(1-t) \tag{3.42}$$

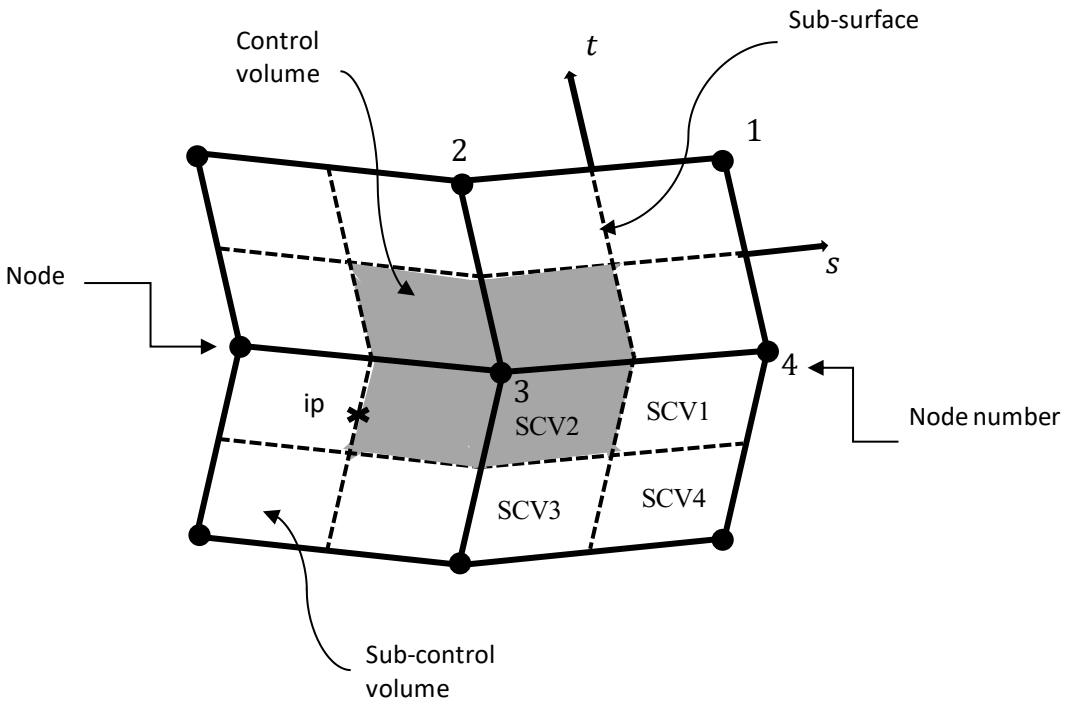

Figure 3-1: Schematic of finite elements and a control volume

The scalar spatial derivatives can be expressed as:

$$\frac{\partial \phi}{\partial x} = \sum_{i=1}^{4} \frac{\partial N_i}{\partial x} \Phi_i \tag{3.43}$$

$$\frac{\partial \phi}{\partial y} = \sum_{i=1}^{4} \frac{\partial N_i}{\partial y} \Phi_i \tag{3.44}$$

The shape function derivatives can be determined using the chain rule of calculus, given by:

$$\begin{Bmatrix} \frac{\partial N_i}{\partial x} \\ \frac{\partial N_i}{\partial y} \end{Bmatrix} = \frac{1}{|J|} \begin{pmatrix} \frac{\partial y}{\partial t} & -\frac{\partial y}{\partial s} \\ -\frac{\partial x}{\partial t} & \frac{\partial x}{\partial s} \end{pmatrix} \begin{Bmatrix} \frac{\partial N_i}{\partial s} \\ \frac{\partial N_i}{\partial t} \end{Bmatrix} \tag{3.45}$$

where $|J|$ represents the Jacobian determinant expressed as:

$$|J| = \frac{\partial x}{\partial s}\frac{\partial y}{\partial t} - \frac{\partial y}{\partial s}\frac{\partial x}{\partial t} \tag{3.46}$$

Also,

$$\frac{\partial x}{\partial s} = \sum_{i=1}^{4} \frac{\partial N_i}{\partial s} x_i; \quad \frac{\partial x}{\partial t} = \sum_{i=1}^{4} \frac{\partial N_i}{\partial t} x_i \tag{3.47}$$

$$\frac{\partial y}{\partial s} = \sum_{i=1}^{4} \frac{\partial N_i}{\partial s} y_i; \quad \frac{\partial y}{\partial t} = \sum_{i=1}^{4} \frac{\partial N_i}{\partial t} y_i \tag{3.48}$$

The local-global coordinate transformations and geometric information will be used to discretize the conservation equations.

3.3.1 General Transport Equation Discretization

Consider a general scalar quantity, ϕ, such as temperature, transported throughout a flow field by convection and diffusion. The CVFEM ensures a balance for the conserved scalar across the control volumes within the domain. The general two-dimensional scalar conservation equation can be written as:

$$\frac{\partial(\rho\phi)}{\partial t} + \nabla \cdot (\rho \boldsymbol{v}\phi) - \nabla \cdot (\Gamma \nabla\phi) = \dot{P} \tag{3.49}$$

Integrating Equation (3.49) over the sub-control volume, $SCVi$, enclosed by the surface area, S_i, and using the Gauss divergence theorem,

$$\int_t^{t+\Delta t} \int_{SCVi} \frac{\partial(\rho\phi)}{\partial t} dV dt + \int_t^{t+\Delta t} \int_{S_i} (\rho \boldsymbol{v}\phi) \cdot n \, dS dt$$

$$- \int_t^{t+\Delta t} \int_{S_i} (\Gamma \nabla\phi) \cdot n dS dt = \int_t^{t+\Delta t} \int_{SCVi} \dot{P} \, dV dt \tag{3.50}$$

where $\boldsymbol{v}$ represents the velocity vector at the surface, and $\boldsymbol{n}$ denotes the unit normal vector at the surface. The transient storage term is discretized based on a backward difference method. Given a reference sub-control volume, $SCVi$, the transient term is approximated as:

$$\int_t^{t+\Delta t} \int_{SCVi} \frac{\partial(\rho\phi)}{\partial t} dVdt = J_i\left(\rho\Phi_i^{t+\Delta t} - \rho\Phi_i^t\right) \tag{3.51}$$

where Φ represents the local nodal value, and J_i represents the Jacobian determinant for a given node i. To integrate the transient term over the entire control volume, the terms of the sub-control volume of other elements sharing the same node are added to the transient term.

The integration point variables, as well as their convective fluxes can be obtained by an upwinding differencing scheme (UDS), central differencing scheme (CDS), or exponential differencing scheme (EDS) [3,147]. In this thesis, the convection fluxes are determined by UDS for the values at the integration point. The integration point equations are obtained by pointwise approximations in Equation (3.50). For example, the transient term at each integration point, i, is approximated by a backward difference,

$$\left.\frac{\partial\phi}{\partial t}\right|_{ip_i} = \frac{\phi_{ip_i}^{t+\Delta t} - \phi_{ip_i}^{t}}{\Delta t} \tag{3.52}$$

3.3.2 Discretization of Convection and Diffusion Terms

The convection and diffusion terms in the discretized general transport equation are evaluated at the sub-surfaces (see Figure 3.1) using a midpoint approximation method. For the convection term in Equation (3.50),

$$\int_t^{t+\Delta t} \int_{S_i} (\rho \boldsymbol{v} \phi) \cdot n \, dS dt = \rho u^{ip} \emptyset^{ip} \Delta t \Delta y_i - \rho v^{ip} \emptyset^{ip} \Delta t \Delta x_i \tag{3.53}$$

Then the convective operator at the integration point can be expressed as:

$$\rho u \frac{\partial \phi}{\partial x} + \rho v \frac{\partial \phi}{\partial y}\Big|_{ip_i} = \rho V \left(\frac{\phi_{ip_i} - \phi_u}{L_c} \right) \tag{3.54}$$

where $V = \sqrt{u^2 + v^2}$ denotes the velocity magnitude of the fluid, ϕ_u refers to the upwind value of the variable ϕ, and L_c represents the convective length scale. The directional calculation of the line portion between ϕ_u and ϕ_{ip_i} is a skewed upwinding approach as shown in Figure 3.2.

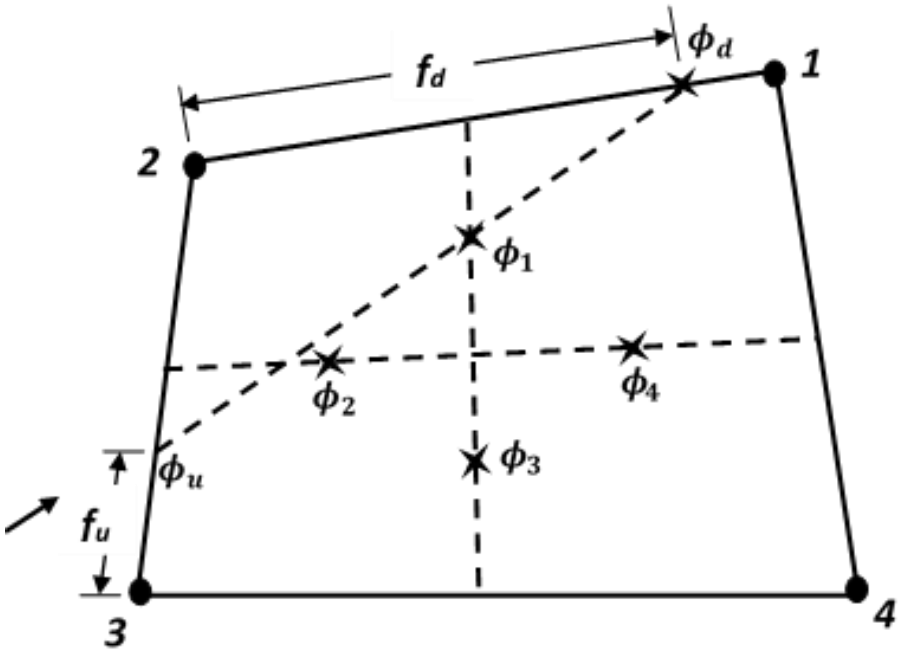

Figure 3-2: Schematic of skew upwinding

The exponential differencing scheme is used to evaluate the integration point scalar variables in the discretized general scalar transport equation, Equation (3.50). The EDS discretization is a hybrid scheme which provides a smooth transition from the central differencing scheme, for low Peclet numbers, to the upwind differencing scheme for high Peclet numbers. It can be written as [29]:

$$\phi^{ip} = \left(\frac{1+\propto}{2}\right)\phi_u + \left(\frac{1-\propto}{2}\right)\phi_d \tag{3.55}$$

where $\propto \simeq Pe^2/(5+Pe^2)$ [29] and the Peclet number is $Pe = \rho u_i \Delta x_i/\Gamma$. The upstream value, ϕ_u, is obtained by interpolation between local nodes where the upwind direction line and the quadrant edge intersect. For example, between local nodes *i* and *i+1*, the upstream value is:

$$\phi_u = f_u \Phi_i + (1-f_u)\Phi_{i+1} \tag{3.56}$$

where f_u represents the coefficient of the corresponding linear interpolation for ϕ_u with reference to the local nodes as illustrated in Figure 3.2. Similarly, the downstream value of the variable is obtained as:

$$\phi_d = f_d \Phi_i + (1-f_d)\Phi_{i+1} \tag{3.57}$$

where f_d represents the coefficient of the corresponding linear interpolation for ϕ_d with reference to Φ_i and Φ_{i+1}. The order of accuracy for the approximated interpolation variable between the local nodes and integration point variable in the convection and diffusion terms is second-order accurate [3].

The diffusion operator at the integration point is approximated by a CDS method [145],

$$\frac{\partial^2 u}{\partial x^2} + \frac{\partial^2 u}{\partial y^2}\Big|_{ip_i} = \frac{1}{L_d^2}\left(\sum_{j=1}^{4} N_i \Phi_i - \phi_{ip_i}\right) \tag{3.58}$$

where L_d represents the diffusion length scale. For an integration point 1, the diffusion length scale can be written as:

$$L_d^2 = \left(\frac{2}{\Delta x^2} + \frac{8}{3\Delta y^2}\right)^{-1} \tag{3.59}$$

The diffusion term in Equation (3.50) is computed at the bottom and left sub-surfaces relating to SCV1,

$$\int_t^{t+\Delta t} \int_S (\Gamma \nabla \phi) \cdot n \, dS \, dt = \Gamma \frac{\partial \phi}{\partial n}\Big|_{ip_i} \Delta t \Delta y_i - \Gamma \frac{\partial \phi}{\partial n}\Big|_{ip_i} \Delta t \Delta x_i \tag{3.60}$$

The scalar variable, temperature, and diffusion flux for the energy equation are related by Fourier's law. Equation (3.60) is calculated based on the midpoint approximation.

The lumped approximation method is used to evaluate the source term in Equation (3.50),

$$\int_t^{t+\Delta t} \int_{SCVi} \dot{P} \, dV \, dt = J_i \Delta t \dot{P}\Big|_{\left(\frac{1}{2},\frac{1}{2}\right)} \tag{3.61}$$

where the subscript, $\left(\frac{1}{2},\frac{1}{2}\right)$, refers to the local coordinate position in the middle of $SCVi$. The local source terms are obtained by directly substituting the corresponding variables at the integration point using the Boussinesq approximation. After the substitution of the integration point variables into Equation (3.50), the integration point variable is written explicitly in terms of nodal values through the local inverted matrices [148].

3.3.3 Assembly of Elemental Equations

The assembly of all elements is performed after the integration point and sub-control volume equations are obtained within an element. Consider node P, with four different neighbouring elements. The control volume for the node is produced by assembling the respective sub-control volume contribution from each of the four elements sharing node P.

For example, consider the heat conduction term of the energy equation at node 3 in Figure 3.1. The energy balance at local node 3 of sub-control volume 1 can be defined as:

$$\int_V \rho C_p \frac{\partial T}{\partial t} dV = Q_{2,1} + Q_{4,1} + Q_{e1,1} + Q_{e2,1} \tag{3.62}$$

where $Q_{e1,1}$ and $Q_{e2,1}$ refer to the exterior elements that also add heat flows to the energy balance for sub-control volume 1, while Q represents the heat flux across the sub-surface. Within the element $Q_{2,1}$, the heat flux at subsurface 1 can be determined as:

$$Q_{2,1} = \sum_{i=1}^{4} \left\{ \int_0^1 \left(k \frac{\partial N_i}{\partial x} \frac{\partial y}{\partial t} - k \frac{\partial N_i}{\partial y} \frac{\partial x}{dt} \right)_{s=0} dt \right\} T_i \tag{3.63}$$

where t denotes the local coordinate.

3.3.4 Entropy Formulation

In the previous section (3.3.3), a CVFEM was outlined. Results will be presented for velocity and temperature in a subsequent section based on numerical simulations with the CVFEM. These results can be post-processed to determine the velocity and temperature gradients, followed by the entropy production rates, with a CVFEM again or any other

numerical method. The resulting magnitude of the discretized entropy production and apparent entropy production difference will provide a useful numerical indicator for the selected numerical method under consideration. In some circumstances, it may be desirable or necessary to use a different numerical method for the Second Law analysis, for example, in post-processing of past results by the apparent entropy production difference to assess accuracy of a numerical model if experimental data was not available.

A Second Law analysis can be performed independently of the numerical method used to solve the conservation variables because it assesses the positivity of entropy production only within the numerical framework of how the Second Law is formulated. To demonstrate this versatility, a general method of numerical discretization will be used in this section to compute the apparent entropy production difference. A common and standard finite difference method will be adopted.

A typical finite difference grid is presented in Figure 3.3. The nodes are located at the points of intersection of the grid lines. Additional nodes can be created throughout the domain if required for higher accuracy. The location of an arbitrary point in the domain is denoted by the nodal coordinates (i, j), where i and j are counter indices in the x and y directions, respectively. The point above is $(i, j + 1)$, while the point below is $(i, j - 1)$. The point to the right is $(i + 1, j)$, while the point to the left is $(i - 1, j)$. In nonuniform grids, the spacing between nodal points in the x and y-directions varies, while, in uniform grids, the spacing between nodes is uniform. Grid refinements produce more accurate results; however, at the cost of more computer memory and computational time for a larger number of equations to be solved.

Using a standard central differencing approximation, the positive-definite entropy generation in Equation (3.18) at node (i, j) can be discretized as follows:

$$\dot{P}_{s,pd} = \frac{k}{T_{i,j}^2}\left(\left.\frac{\partial T}{\partial x}\right|_{i,j}^2 + \left.\frac{\partial T}{\partial y}\right|_{i,j}^2\right) + \frac{\mu}{T_{i,j}}\Phi_{i,j} \tag{3.64}$$

where

$$\Phi_{i,j} = \left(\frac{\partial u}{\partial y} + \frac{\partial v}{\partial x}\right)_{i,j}^2 + 2\left(\frac{\partial u}{\partial x}\right)_{i,j}^2 + 2\left(\frac{\partial u}{\partial x}\right)_{i,j}^2 \tag{3.65}$$

Here the subscript (i, j) refers to the discretized approximation at node (i, j) for terms in brackets using the local spatial gradients from the derivative expression.

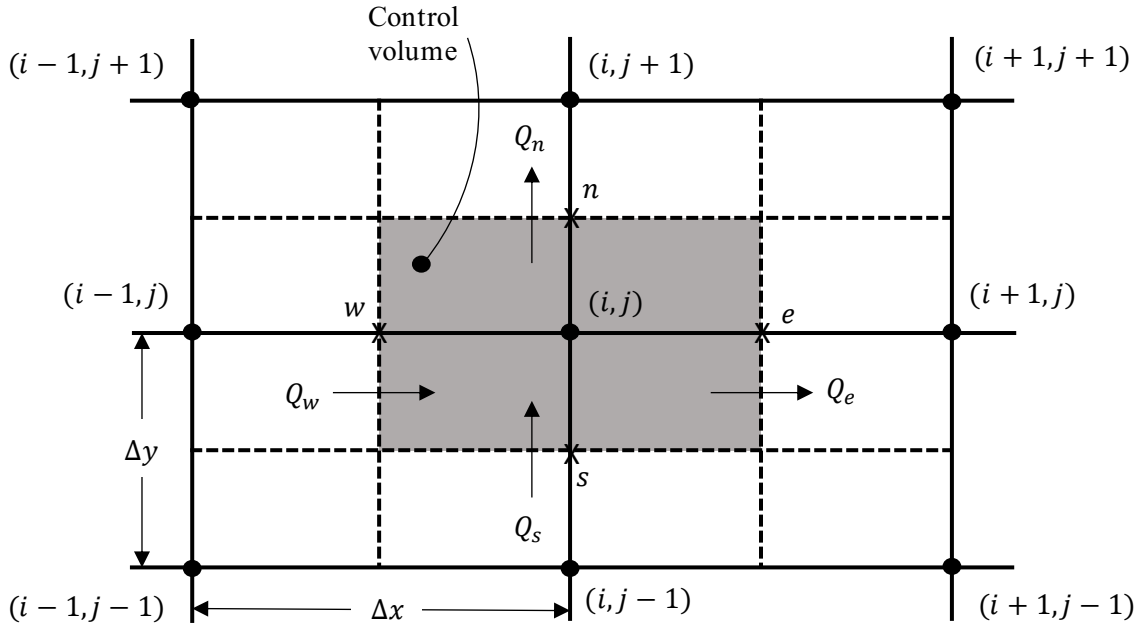

Figure 3-3: Schematic for finite difference formulation

The central difference approximation of the scalar derivative is second-order accurate since the truncation errors correspond to terms truncated above the second order from a Taylor series expansion, i.e.,

$$\left.\frac{\partial \theta}{\partial x}\right|_{i,j} = \frac{\theta_{i+1,j} - \theta_{i-1,j}}{2\Delta x^2} + O(\Delta x^2) \tag{3.66}$$

where Δx refers to the grid spacing in the x-direction. The magnitude of the truncation error decreases approximately quadratically with the square of the grid spacing.

Using Fourier's law of heat conduction in Equation (3.27) and the central differencing approximation, the entropy transport equation can be discretized as:

$$\dot{P}_{s,te} = \rho\left(\left.\frac{\partial s}{\partial t}\right|_{i,j} + u\left.\frac{\partial s}{\partial x}\right|_{i,j} + v\left.\frac{\partial s}{\partial y}\right|_{i,j}\right) - \frac{k}{T_{i,j}}\left(\left.\frac{\partial^2 T}{\partial x^2}\right|_{i,j} + \left.\frac{\partial^2 T}{\partial y^2}\right|_{i,j}\right) \tag{3.67}$$

where k is the thermal conductivity. The second derivative of the scalar variable is given as:

$$\left.\frac{\partial^2 \theta}{\partial x^2}\right|_{i,j} = \frac{\theta_{i+1,j} - 2\theta_{i,j} + \theta_{i-1,j}}{\Delta x^2} + O(\Delta x^2) \tag{3.68}$$

This approximation is also second-order accurate. The scalar variable at nodal point (i, j) for a uniform grid is expressed as:

$$\theta_{i,j} = \frac{1}{4}\left(\theta_{i+1,j} + \theta_{i-1,j} + \theta_{i,j+1} + \theta_{i,j-1}\right) \tag{3.69}$$

The magnitude of truncation errors and order of accuracy for the numerical approximation of the entropy production (positive-definite and transport equation) are both second order.

In the entropy transport equation, a piecewise logarithmic equation of state is used to compute entropy at the node:

$$s = s_r + C_p \log\left(\frac{T}{T_r}\right) \tag{3.70}$$

where the subscript r represents a reference state i.e., $s_r = 0$ at $T_r = 273$ K.

Using the above formulations, the positive-definite and transport forms of the Second Law can be computed, after which the apparent entropy production difference is found and normalized (non-dimensional). A new hypothesis is hereby proposed that the solution error is directly related to this normalized apparent entropy production difference, i.e.,

$$E_\phi = \Delta \dot{P}_{s,n} \tag{3.71}$$

where E_ϕ denotes the numerical solution error in the scalar variable, ϕ. In the following chapter, this hypothesis will be examined, tested, and further discussed.

3.4 Nanofluids Formulation

As discussed previously, nanofluids are fluids that contain nano-scale particles and typically have enhanced heat transfer characteristics and thermal conductivity when compared to a base fluid such as water, ethylene glycol or oil. Nanoparticles are made from the synthesis of metallic or non-metallic materials such as metals, nitrides, oxides, and graphite. They can be synthesized by various procedures such as gas condensation, chemical precipitation, or mechanical attrition. Nanofluids are formed through a colloidal mixture of nanoparticles and a base fluid. In fluids engineering applications, there can be

possible wall surface erosion, an increase in pumping power due to the presence of nanoparticles, and potential instability due to silts of particles.

Different possible transport mechanisms for the particle motion in the nanofluids include Brownian motion, diffusiophoresis, and thermophoresis. Brownian motion occurs due to the collision of nanoparticles with molecules of the base fluid. This is a random motion of the particle suspended in the gas or fluid. The Brownian motion is driven by an increase in temperature, while the thermal conductivity is enhanced by energy transfer from the collision of particles of higher temperatures with lower temperature particles. As the bulk viscosity increases, the Brownian motion effectiveness increases [149,150].

Thermophoresis (also known as a Soret effect) occurs due to the drifting of nanoparticles against a temperature gradient, from a high-temperature region to a region of low temperature. This phenomenon is most significant in a free convection process, in which the flow is driven by temperature and buoyancy. A reduction in bulk density increases the rate of heat transfer. In contrast, diffusiophoresis (or osmo-phoresis) is a transport mechanism which involves drifting of suspended nanoparticles from a zone of lower concentration to a zone of higher concentration. This is generally not a preferred method due to the agglomeration of the nanofluids [151].

Nanofluids are analogous to two-phase multicomponent fluids which consist of nanoparticles and a base fluid. The effective properties of nanofluids have been modelled in numerous past studies [94, 96, 145, 152]. For the effective density,

$$\rho_{nf} = (1 - \emptyset)\rho_f + \emptyset\rho_p \tag{3.72}$$

where Ø is the nanoparticle volume fraction. The specific heat capacity of the nanofluid can be expressed as:

$$C_{nf} = \frac{(1-Ø)(\rho C)_f + Ø(\rho C)_p}{(1-Ø)\rho_f + Ø\rho_p} \tag{3.73}$$

The effective dynamic viscosity can be predicted by the Brickman model [152],

$$\mu_{nf} = \frac{\mu_f}{(1-Ø)^{2.5}} \tag{3.74}$$

The effective thermal conductivity cannot be simply obtained by the volume fraction-weighted sum of the nanoparticle properties and the base fluid, as in the case of the effective density and specific heat capacity of the nanofluid, since there are typically no universal relations for the effective thermal conductivity of various nanofluids. The calculation of the effective thermal conductivity involves a more detailed formulation based on experimental correlations such as the Maxwell-Garnetts model [145],

$$\frac{k_{nf}}{k_f} = \frac{k_p + 2k_f - 2Ø(k_f - k_p)}{k_p + 2k_f + Ø(k_f - k_p)} \tag{3.75}$$

where k_f is the thermal conductivity of the base fluid, k_p is the thermal conductivity of the nanoparticle, and k_{nf} is the thermal conductivity of the nanofluid.

Also, the heat capacity of the nanofluid is given by:

$$(\rho C)_{nf} = (1 - Ø)(\rho C)_f + Ø(\rho C)_p \tag{3.76}$$

The effective thermal diffusivity is written as:

$$\alpha_{nf} = \frac{k_{nf}}{\rho C_{nf}} \tag{3.77}$$

For the thermal expansion coefficient,

$$(\rho\beta)_{nf} = (1 - \emptyset)(\rho\beta)_f + \emptyset(\rho\beta)_p \quad (3.78)$$

The physical principle of the general mixture rule is used to predict the effective density, effective heat capacity and effective thermal expansion coefficient. The rule of mixtures is a weighted mean used to estimate various properties of a composite material. It provides a theoretical lower and upper-bound on properties such as density and heat capacity. These effective properties of the nanofluids were theoretically calculated through their basefluid and nanoparticle properties, and both the working fluid and nanoparticles are assumed to be a mixed property [153]. The use of the rule of mixtures to predict effective density and effective thermal expansion coefficient is generally accepted by researchers. The only constraint to the use of this method is that it is generally applicable to a low and moderate volume fraction (0-10%) [154], and the nanofluids analyzed in this thesis fall in this category.

The correlation for the effective specific heat is a product of experimentally investigated values that considered nanofluids involving nanoparticles with 45 nm average particle diameter, a temperature range of 298.15K and 313.15K and volume fraction between 0 - 21.7%. It was concluded that the model can predict the value of effective specific heat of nanofluids well within the ±5% margin. This is the closest accurate correlation available for predicting the effective specific heat as research is currently ongoing to develop a more accurate model [155,156].

The Brinkman model used to calculate the effective dynamic viscosity was developed in 1952 as an extension of Einstein's equation suitable for use with moderate particle volume fractions. This examined the effect of a mixture of solute molecules with an existing

continuous medium of particle volume fraction less than 10 %. This correlation has broad acceptance among the researchers [157]. The theoretical calculation of the effective thermal diffusivity of nanofluids has been studied by very few published articles. From past literature, there appears to exist only one theoretical model for predicting the effective thermal diffusivity, which is generally used by researchers.

Maxwell's model for the prediction of the effective thermal conductivity of base fluid-nanoparticle mixtures with particles above 1 μm diameter shows reasonable agreement with experimental data at low and moderate nanoparticles volume fractions. Maxwell's model predicts that the thermal conductivity of the mixture depends on the thermal conductivity of the base fluid and spherical particle, as well as the solid particles volume fraction. More recent research has attempted to include other factors such as nanolayers between the base fluid and nanoparticles, clustering of particles, nonspherical particles, intermolecular interactions among distributed particles, thermophoresis, and Brownian motion. Due to the complexity of these processes, there have not been a generally applicable relations for all types of nanofluids [145]. These properties will be used in subsequent chapters for the formulation and analysis of fluid flow and heat transfer problems involving nanofluids.

3.5 Numerical Modelling

The modelling and discretization of the formulations described in Chapter 3 are implemented by developing a source code using the Python programming language. The Python code solves the entropy production equations by using post-processed velocity and temperature fields, which are obtained by using the Control-Volume-Based Finite Element Method (CVFEM) to solve the mass, momentum and energy conservation equations using

a C++ source code. Both Python and C++ source codes are interfaced through data recovery and a management program which is an enhanced Python version of a PHASES C++ function called filedata that is used to import problem and mesh parameters.

The typical simulation workflow can be broken down into three main components: the problem definition, the simulation, and the data analysis. The problem definition occurs where the problem parameters are defined. This includes the geometry of the problem, the initial and boundary conditions of the simulation, and the fluid properties. The second part is to simulate the fluid behavior and dynamics based on the problem parameters as stated in the problem definition. After the simulation is the data analysis stage, at which point the outputs from the simulation are presented visually so that they can be interpreted and analyzed by the user.

The first simulation input is the geometry of the problem. The problem domain is discretized by dividing into nodes and elements. For a CVFEM, each of these elements is a quadrilateral. Each element is defined by specifying the x and y coordinates of its four corners (nodal points). Other important parts of the mesh that need to be defined are the boundary edges, which are defined by a set of two nodes which lie on the boundary of the mesh.

In addition to the mesh geometry, the simulation requires initial conditions, boundary conditions, and fluid properties to be defined. Initial conditions are defined for each individual element, and represent the values of temperature, velocity, and concentration of the fluid at the time in which the simulation starts. Boundary conditions are defined for

each boundary. This is represented by a differential equation that has three coefficients which must be defined.

Boundary conditions appear in the form A (dG/dn) + B (G) = C where G represents a scalar (i.e. velocity, concentration, temperature, etc.). This equation permits three types of conditions.

1) Dirichlet condition; the scalar value of G is specified along the boundary nodes, i.e. A = 0, B = 1 and C = 1 implies G (concentration) = 1 along the boundary.
2) Neumann conditions: the scalar's first derivative, dG/dn (n=normal direction) is specified along the boundary nodes, i.e. A = 1, B = 0 and C = 0 implies an adiabatic boundary for G = temperature.
3) Robin conditions: this type refers to a combination of scalar (i) and flux specified (ii) conditions. For example, A = k (where k = conductivity), B = h (where h = convection coefficient) and C = T_0 (T_0 represents a reference value) refers to a mixed conduction /convection condition for T = temperature. Thirdly, the fluid properties must be defined.

The simulation will then produce output data for each node within the mesh. This can be done for five different types of data which are the temperature, u-velocity, v-velocity, entropy production, and concentration. This data is represented in discretized time steps, meaning that there will be output data for a finite number of points in time which must be defined.

Once the output data has been calculated it is necessary to visualize it graphically. The current implementation uses a package called matplotlib, which offers similar functionality to Matlab within the Python programming language. It can also be embedded into a Graphical User Interface (GUI), which makes it stratightforward to generate graphs efficiently. The output data for the velocities, temperature and entropy production can be visualized using contour plots and vector fields.

The results and discussion of this work are presented in the following chapters, Chapters 4, 5 and 6.

4 ENTROPY PRODUCTION IN NATURAL AND MIXED CONVECTION HEAT TRANSFER

4.1 Introduction

Natural convection heat transfer in enclosures occurs in various engineering applications. For example, heating, cooling and ventilation in buildings, cooling of microelectronic assemblies, heat transfer between glass panes in double-pane windows, fluid-filled cavities surrounding a nuclear reactor core, and solar collectors, involve natural convection. Several studies on natural convection have been reported in the literature, although only a relatively few studies have considered the related importance of entropy and the Second Law in natural and mixed convection applications.

A specified rate of heat transfer can be achieved in natural convection problems, but with varying degrees of frictional and thermal irreversibilities, depending on the temperature difference across which heat transfer occurs and the surface area. For example, the convective cooling of a microelectronic assembly involves natural convection from the heat sink; however, pressure losses occur due to forced convection of air past the internal components. In this case, each unit of entropy generation (or exergy destruction) gives rise to a corresponding level of heat flow which should be removed but cannot due to entropy generation. This entropy generation leads to pressure losses and dissipation of kinetic energy into internal energy which opposes the desired aim of the component cooling.

Another example is the addition of nanoparticles to a base fluid, in a mixed convection setting, which increases the effective thermal conductivity of the nanofluid, giving rise to a reduction in the temperature gradient and entropy production due to heat transfer

irreversibilities. But the addition of nanoparticles to the base fluid will increase the effective fluid viscosity and result in an increase of the entropy production due to friction. As the wall velocity increases, heat is removed from the system, thereby reducing entropy production due to thermal irreversibilities. But the increase in the wall velocity will enhance the fluid friction and produce higher entropy production due to friction irreversibilities.

The study of nanofluids has become an area of interest to many researchers due to the unique heat transfer potential of such a new category of fluids. Nanofluids are suspension of nanoparticles, which are usually metal oxides, within a working fluid such as oil, glycol, or water. The mixture of nanoparticles with a base fluid leads to the increase of its thermal conductivity; in particular, nanoparticles contribute to enhance the heat transfer capabilities of nanofluids when compared to the base fluids such as water, oil, or glycol. On the other hand, the viscosity of the suspension also increases, and the viscosity of the fluid impact on its flow configuration such as pumping power. Hence, there is a competing behavior of viscosity and thermal conductivity which both increase with nanoparticles concentration, therefore it is necessary to obtain an optimal value.

The nanofluid properties are modelled differently from the base fluids by using well established and suitable effective nanofluid property models which are described in Section 3.4. There may be other phenomena that drive the nanoparticle transport and thermal enhancement. However, as an emerging field, several investigations are currently ongoing to develop a more robust effective properties model for all nanofluids types, but this is not a scope of this research.

The essence of this research to perform a numerical investigation of entropy generation and Second Law analysis for Cu-water, TiO_2-water, and Al_2O_3-water nanofluids in natural and mixed convection enclosure, in order to understand the optimal working conditions of the system. For example, the investigation of the optimum nanoparticle volume fraction for which entropy production is minimized is essential for pumping power optimization.

Different flow conditions, such as, wall velocity, wall temperature, heat flux, and particle concentrations are considered in order to understand their impact on the entropy production. The information presented in this work is believed to be useful in the pursuit of the design optimization of thermal and fluid devices.

Past studies have indicated that numerical solutions involving natural convection in a cavity can be successfully determined by finite elements, finite volumes, or finite differences [158,159,160,161]. The buoyancy term is based on the local temperature; therefore, coupled flow solutions with the energy equation are needed. Previous benchmark solutions provide useful data for the validation of predictive results for variations of heat transfer and flow patterns [158, 159]. Entropy production models have also been applied to system optimization involving natural convection in an inclined cavity [162], laminar natural convection across a heated rotating cylinder [163], and irreversibilities at the onset of free convection in a square enclosure [73]. In contrast to these previous studies, this thesis will present a new approach for determining local entropy production rates, thereby providing a new useful design tool for energy efficiency improvement in natural and mixed convective systems.

A numerical study is performed to analyze the heat transfer and entropy production for both natural and mixed convection in a rectangular enclosure filled with water-based nanofluids. This study presents a new approach for minimizing the entropy production rate in different flow configurations with nanofluids. The governing equations are discretized with a control-volume-based finite-element method (CVFEM). The thermophysical properties of the nanofluids will be evaluated based on experimental data. The analysis considers the effects on entropy production due to variations of the volume fraction ($0 \leq \emptyset \leq 0.12$) of the nanofluid, aspect ratio (AR) of the enclosure, and moving wall velocity (v_w). The study compares the entropy production rates and heat transfer rates for three different nanofluids. The number of timesteps in the simulations of the problems in Chapters 4 and 5 is normally 30. The timesteps are each of 1s duration, although results are steady-state, so the timestep progression of the transient formulation serves like an iterative solver.

The results for a natural convection case indicate a reduction in the rate of entropy production as the nanoparticle volume fraction increases. Results for the mixed convection case establish the optimal nanoparticle volume fraction that minimizes the total entropy production. Through this numerical study, the distribution of nanoparticles and cavity aspect ratio can be more effectively controlled to minimize the entropy production rates.

4.2 Problem Configuration: Natural Convection

Schematic diagrams for the natural convection studies in the rectangular enclosure are illustrated in Figures 4.1 and 4.2. The problem setup is a square enclosure of height H, and width L, filled with water-based nanofluids. A cartesian coordinate system is used so that

the x-axis represents the horizontal axis, and the y-axis refers to the vertical axis in the upwards direction. It is assumed that the nanoparticles and the working fluid are in thermal equilibrium and there is no chemical reaction. Radiative heat transfer, as well as heat transfer due to nanoparticle motion relative to the working fluid, are neglected.

The buoyancy induced flow is assumed to be two-dimensional of a Newtonian fluid. The thermophysical properties of the nanofluid are assumed to be constant. The variation of density in the buoyancy term is determined based on the Boussinesq approximation [146]. The nanofluids are assumed Newtonian with constant properties based on the nanoparticle shape, nanofluid shear rate which is a function of particles volume fraction, the temperatures, and the choice of nanofluids. Nanofluids which contains nanotubes show non-Newtonian behavior, however, nanofluids with spherical nanoparticles exhibit Newtonian flow behavior [164]. A spherical shaped nanoparticles is assumed for this study. Studies demonstrate that certain nanofluids show Newtonian and constant property behaviour when the particle volume fraction is less that 10.5 percent [164,165,166,167], hence, this study focuses on cases of nanoparticle concentrations between 0 and 10 percent.

The physical model of this study considers a steady natural convection boundary layer along the heated walls, as well as a uniform heat flux density. The model uses sufficiently small temperature gradients across the boundary layer, such that thermophysical properties of the nanofluids, can be assumed to be constant with exception of the density variation in the buoyancy force, which is modeled using Boussinesq approximation based on incompressibility. Small solid particles with dimensions <50 nm are assumed, hence, believed to fluidize easily, and these particles are considered to have a fluid-like

characteristics [168,169]. One may expect that the basic theory for single-phase fluids can be applied to nanofluids.

The development of nanofluids is generally faced with some challenges such as a higher pressure drop especially at higher thermal conductivity, higher production and operational cost, higher viscosity, increased pumping power, and long-term stability of nanoparticles in engineering applications. Since knowledge of nanofluids is still at elementary stages, it seems extremely difficult to have a precise idea on how the use of nanofluids acts in natural and mixed convection heat transfer, so further research is needed and ongoing in the area of nanofluids development and this is not a scope of this thesis.

Under the above assumptions, the governing equations to be solved for this problem include the continuity, Navier-Stokes, and energy equations as follows:

$$\frac{\partial u}{\partial x} + \frac{\partial v}{\partial y} = 0 \tag{4.1}$$

$$\rho_{nf}\left[\frac{\partial u}{\partial t} + u\,\frac{\partial u}{\partial x} + v\,\frac{\partial u}{\partial y}\right] = -\frac{\partial p}{\partial x} + \mu_{nf}\left(\frac{\partial^2 u}{\partial x^2} + \frac{\partial^2 u}{\partial y^2}\right) \tag{4.2}$$

$$\rho_{nf}\left[\frac{\partial v}{\partial t} + u\,\frac{\partial v}{\partial x} + v\,\frac{\partial v}{\partial y}\right] = (\rho\beta)_{nf} g(T - T_c) + \mu_{nf}\left(\frac{\partial^2 v}{\partial x^2} + \frac{\partial^2 v}{\partial y^2}\right) \tag{4.3}$$

$$\left(\rho C_p\right)_{nf}\left[\frac{\partial T}{\partial t} + u\,\frac{\partial T}{\partial x} + v\,\frac{\partial T}{\partial y}\right] = k_{nf}\left(\frac{\partial^2 T}{\partial x^2} + \frac{\partial^2 T}{\partial y^2}\right) \tag{4.4}$$

where ρ_{nf} represents the density, μ_{nf} denotes the dynamic viscosity, $\left(\rho C_p\right)_{nf}$ refers to the heat capacity, $(\rho\beta)_{nf}$ is the thermal expansion coefficient, and k_{nf} represents the thermal conductivity. The subscript *nf* refers to the nanofluid.

The Nusselt number is used to estimate the convective heat transfer at a fluid boundary. It was obtained as the ratio of the heat flux across the enclosure to the heat flux resulting from conduction. The heat flux across the cavity was evaluated as the mean heat flux on the hot and cold walls of the enclosure since the formulation is conservative. The Nusselt number is calculated by determining temperature gradients at the sub-control volume for boundary elements. The Nusselt number can be defined as:

$$Nu = \frac{hH}{k_{nf}} \tag{4.5}$$

The heat transfer coefficient is calculated from:

$$h = \frac{q_0^{"}}{T_h - T_c} \tag{4.6}$$

The thermal conductivity of the nanofluid can be written as:

$$k_{nf} = -\frac{q_0^{"}}{\partial T/\partial x} \tag{4.7}$$

By substituting Equations (4.6) and (4.7) into Equation (4.5), the local Nusselt number on the hot (left) wall can be expressed as:

$$Nu = -\left(\frac{\partial T}{\partial x}\right).\frac{H}{T_h - T_c} \tag{4.8}$$

The average Nusselt number is determined by integrating the local Nusselt number on the hot wall:

$$Nu_{avg} = \int_0^1 Nu(y)dy \tag{4.9}$$

The thermophysical properties of the nanofluids are presented in Table 4.1. The parameters for the base case simulation are $Ra = 10^5$, $AR = 1$, $\emptyset = 0.02$, $Pr = 6.2$, and the base case nanofluid is Al_2O_3 – water. The rate of entropy production will be presented in non-dimensional form.

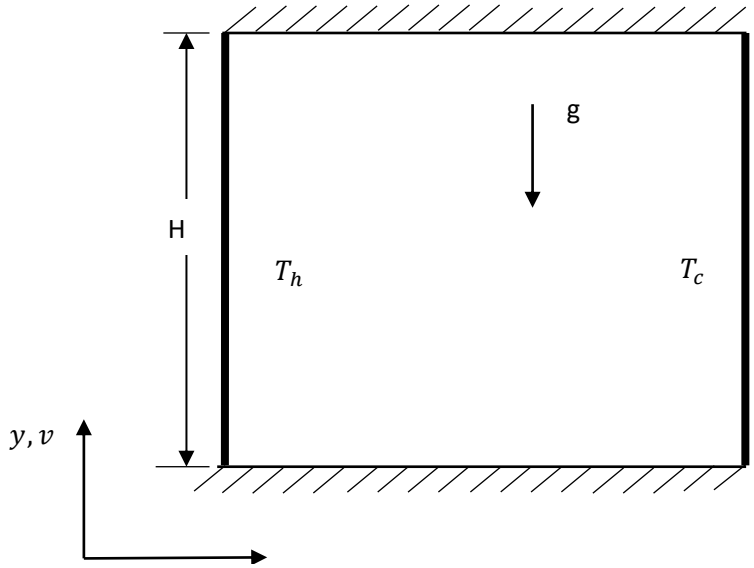

Figure 4-1: Problem configuration for natural convection case 1

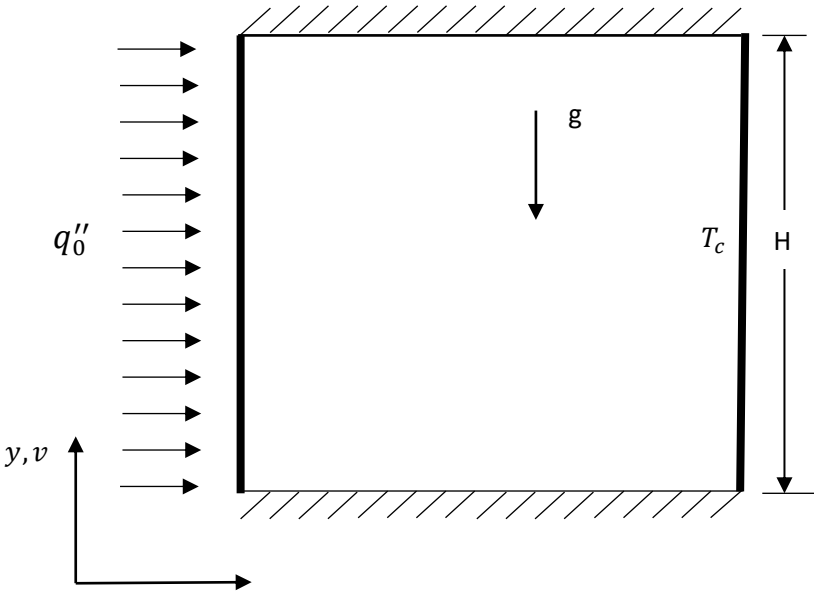

Figure 4-2: Problem configuration for natural convection case 2

Table 4-1: Thermophysical properties of nanoparticles and water

Physical Property	Al_2O_3	Cu	TiO_2	H_2O
Density, ρ (kg/m^3)	3970	8933	4250	993
Thermal Conductivity, K (W/m K)	40	400	8.953	0.613
Specific Heat Capacity, C_p (J/kg K)	765	385	687	4179
Thermal expansion coefficient, β (1/K)	8.5×10^{-6}	1.7×10^{-5}	9.0×10^{-6}	2.1×10^{-6}
Dynamic Viscosity, μ (Pa.s)				8.9×10^{-4}

The thermophysical properties of the nanofluids depend on the models used, the thermophysical properties of the nanoparticles, the thermophysical properties of the basefluid, and the nanoparticle volume fraction. The thermophysical properties of the nanofluids are presented in Table 4.2. These thermophysical properties are obtained based on the models presented in section 3.4, and the thermophysical properties of the basefluid and nanoparticles presented in Table 4.1, at the nanoparticle volume fraction of 0.02.

Table 4-2: Thermophysical properties of nanofluids

Physical Property	$Al_2O_3 – H_2O$	$Cu – H_2O$	$TiO_2 – H_2O$
Density, ρ (kg/m^3)	1053	1152	1058
Thermal Conductivity, K (W/m K)	0.649	0.650	0.644
Specific Heat Capacity, C_p (J/kg K)	3921	3590	3898
Thermal expansion coefficient, β (1/K)	2.059×10^{-4}	2.061×10^{-4}	2.060×10^{-4}

4.3 Grid Refinement Study and Validation of Results

A mesh convergence study was performed for the numerical results. The solutions of temperature and velocity at the local nodes were compared for 11 x 11, 21 x 21, 41 x 41, and 81 x 81 grids. Four different grid sizes were considered for the case of $Ra = 10^4$ and $Pr = 0.71$. As shown in Figures 4.3 and 4.4, the difference between the results of the variables for 41 x 41 and 81 x 81 is infinitesimal, therefore the mesh convergence study shows that grid independent results were obtained with the 41 x 41 grid. It was observed that the values of the variables at the local nodes in the central region (y = 0.004, and y = 0.006) of the problem domain reached convergence earlier than values of the variables at the local nodes in the outer region (y = 0.002, and y = 0.008) of the problem domain.

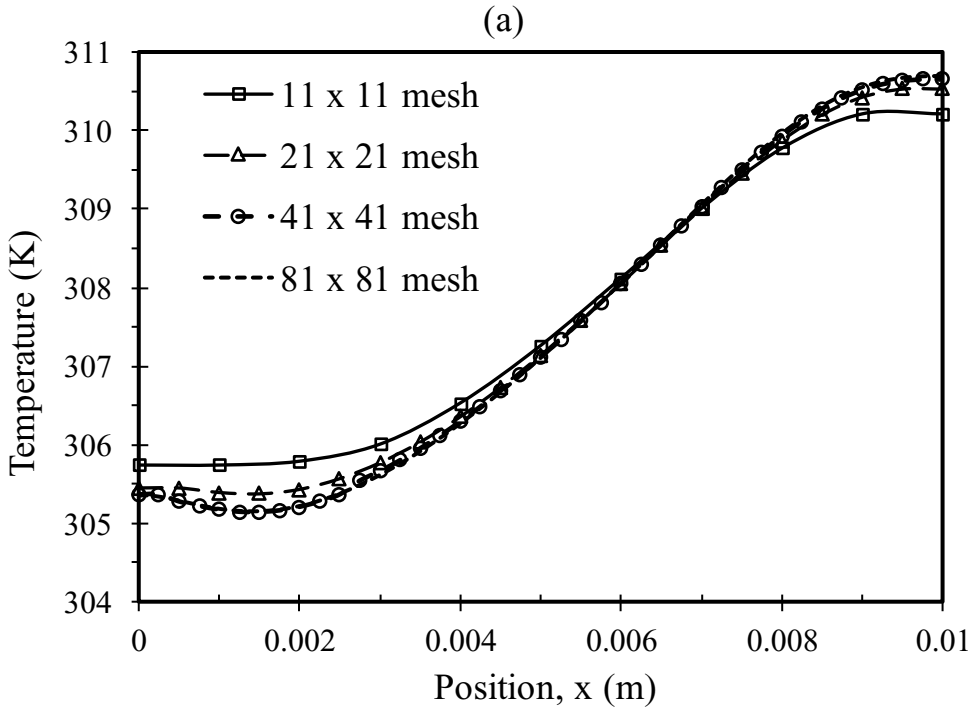

(b)

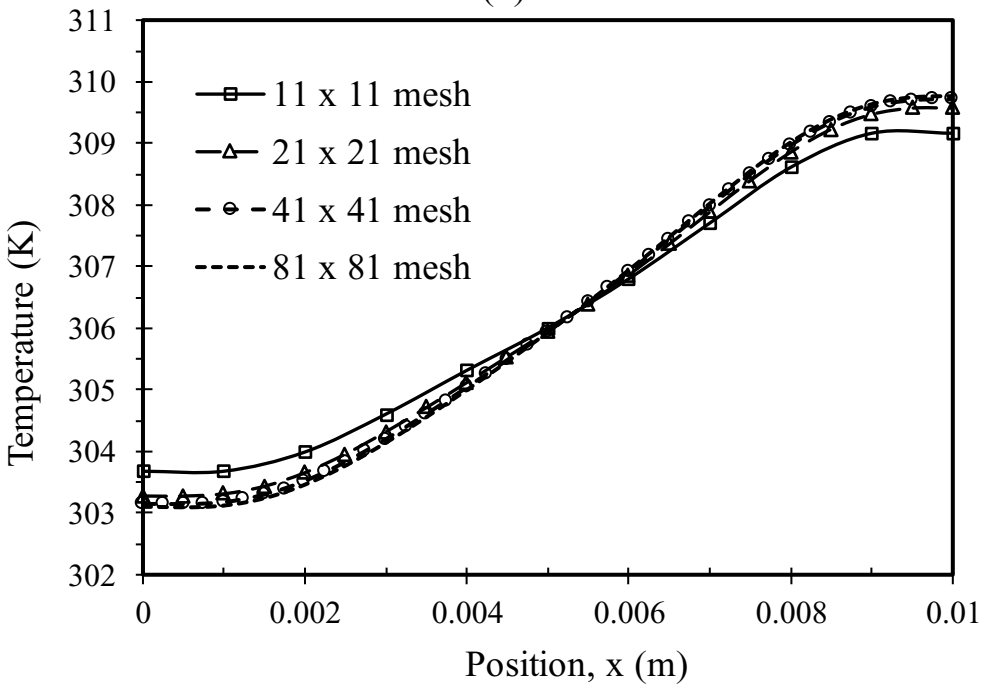
311
310
309
308
307
306
305
304
303
302
Temperature (K)
11 x 11 mesh
21 x 21 mesh
41 x 41 mesh
81 x 81 mesh
0
0.002
0.004
0.006
0.008
0.01
Position, x (m)

(c)

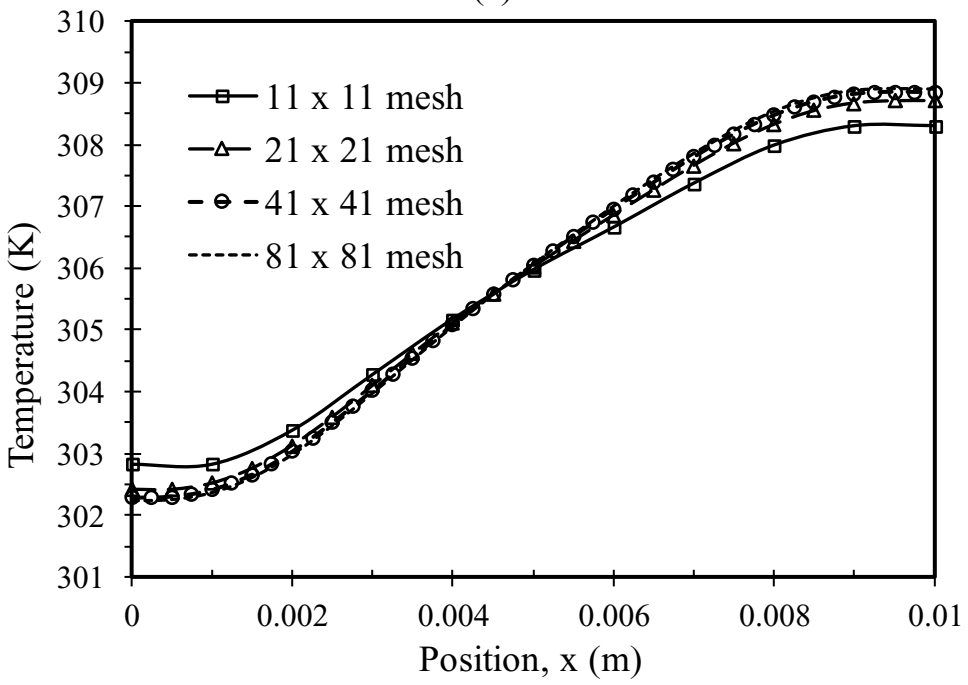
310
309
308
307
306
305
304
303
302
301
Temperature (K)
11 x 11 mesh
21 x 21 mesh
41 x 41 mesh
81 x 81 mesh
0
0.002
0.004
0.006
0.008
0.01
Position, x (m)

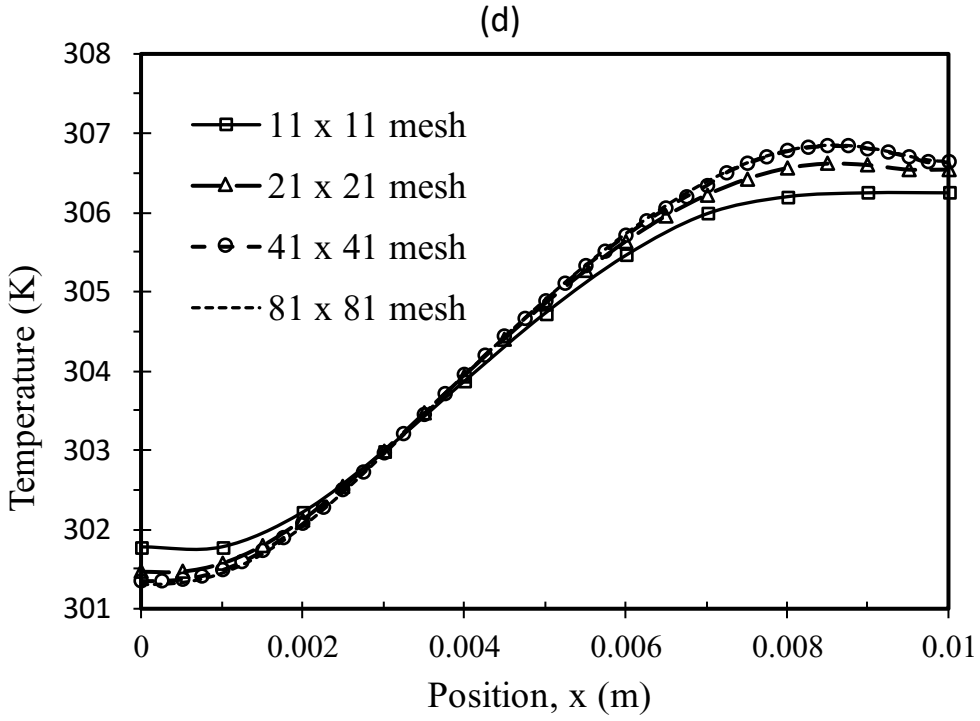

Figure 4-3: Temperature profiles along the length of the enclosure for different grid refinements at (a) y = 0.002, (b) y = 0.004, (c) y = 0.006, (d) y = 0.008 (Ra = 10^4, Pr = 0.71)

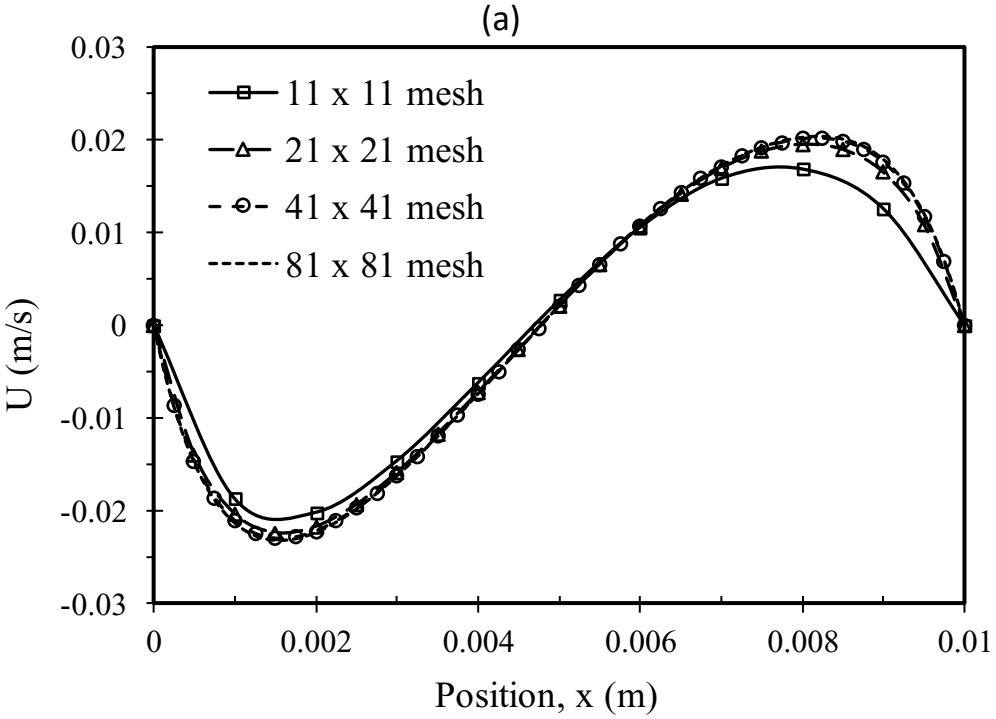

(b)

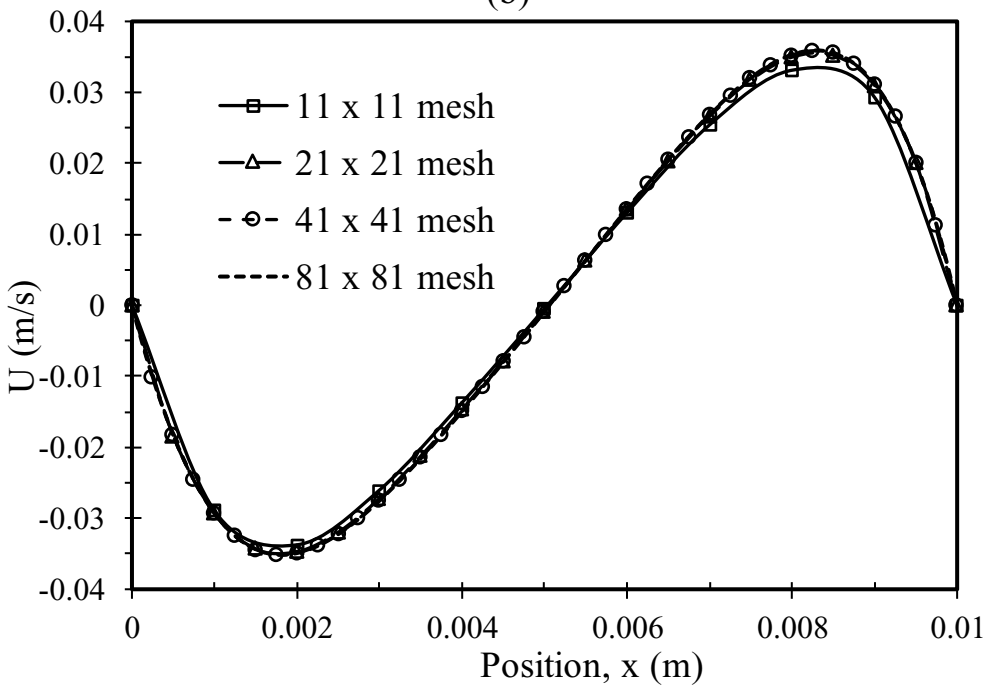
0.04
0.03
0.02
0.01
0
-0.01
-0.02
-0.03
-0.04
U (m/s)
11 x 11 mesh
21 x 21 mesh
41 x 41 mesh
81 x 81 mesh
0
0.002
0.004
0.006
0.008
0.01
Position, x (m)

(c)

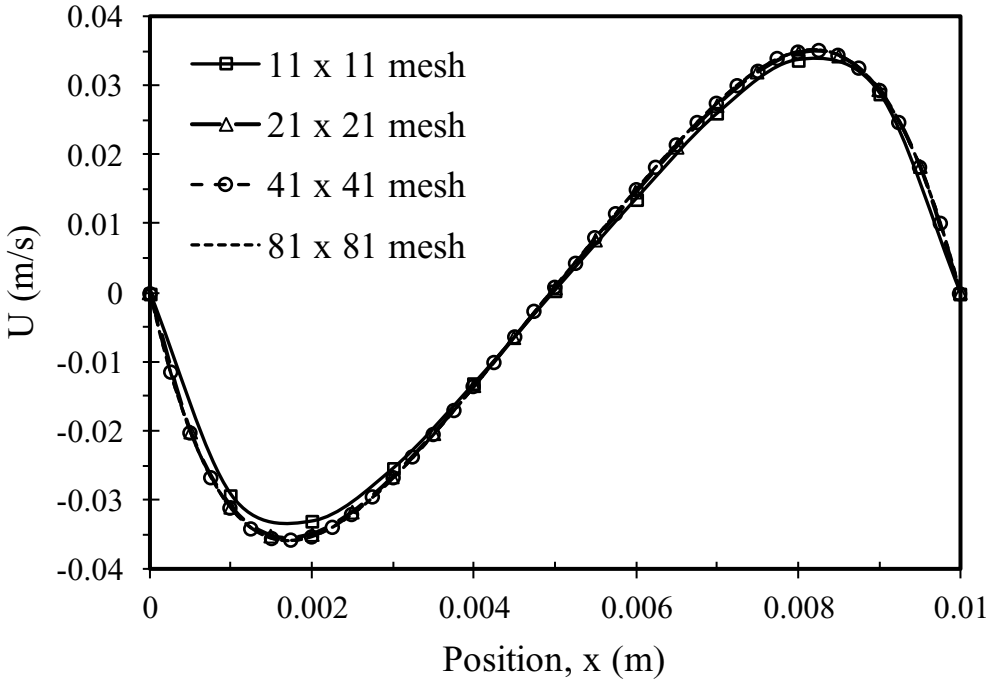
0.04
0.03
0.02
0.01
0
-0.01
-0.02
-0.03
-0.04
U (m/s)
11 x 11 mesh
21 x 21 mesh
41 x 41 mesh
81 x 81 mesh
0
0.002
0.004
0.006
0.008
0.01
Position, x (m)

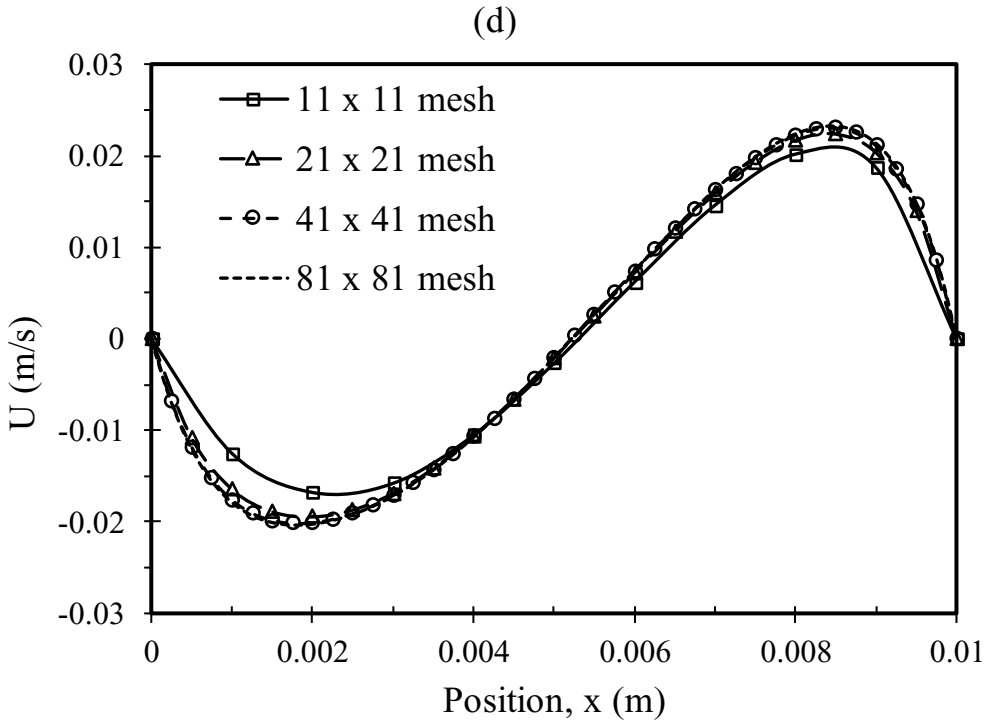

Figure 4-4: *Velocity profiles along the length of the enclosure for different grid refinements at (a) y = 0.002, (b) y = 0.004, (c) y = 0.006, (d) y = 0.008 (Ra = 10^4, Pr = 0.71)*

For example, in the case of the velocity profile, the results at the local nodes around the central region (y = 0.004, and y = 0.006) reach a grid independent solution for a 21 X 21 grid. The results around the outer region (y = 0.002, and y = 0.008) of the problem domain reach a grid independent solution at a 41 X 41 grid. Generally, the temperatures and velocities converge towards the grid independent solution as the mesh is refined.

Figure 4.5 presents a validation of this work by comparing the numerical results with experimental work by Krane and Jesse [177] and a numerical study by Khanafer et al. [94]. The validation results were derived from a case of a square cavity with differential wall temperatures as illustrated in Figure 4.1. A Rayleigh number of 1.89 x 10^{-5} and Prandtl number of 0.71 was considered for this problem. The temperature values were obtained

from local nodes along the horizontal centreline. In this case, the validation of the numerical results is limited to the local nodes along the horizontal centreline because of unavailability of experimental data in other regions of the domain. In such problems, only validation of along the centreline is often published.

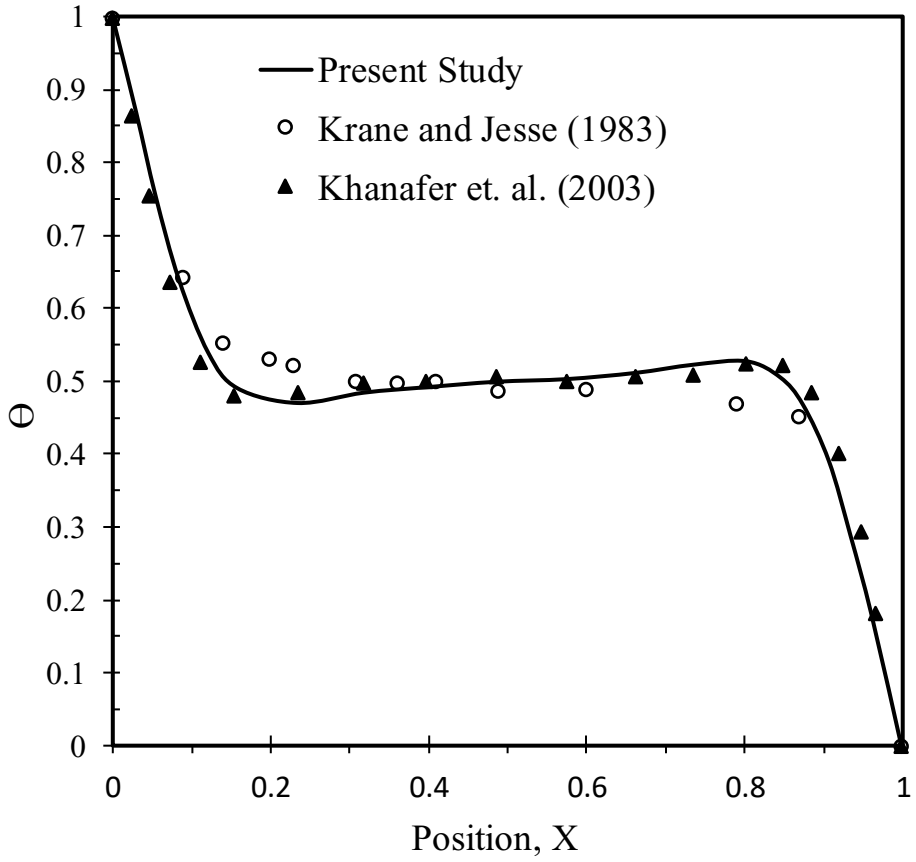

*Figure 4-5: Comparison of temperature distribution with past experimental work (*Ra = *1.89 X 10^5,* Pr = *0.71)*

Although there is a slight discrepancy between the numerical and experimental results, in general, the results show good agreement. The slight discrepancy is likely due to numerical discretization approximations. In Chapter 6 of this thesis, the use of entropy-based artificial

viscosity as a corrective mechanism to potentially reduce solution errors and enhance numerical accuracy will be discussed.

Also, the results were verified by comparisons with benchmark solutions [158,170]. Tables 4.3 and 4.4 show the predicted values of the maximum horizontal velocity along the vertical centerline (u_{max}) of the enclosure with its position (y), and the maximum vertical velocity (v_{max}) along the horizontal centerline with its position (x). A comparison of the values with the given benchmark solutions for $\mathrm{Ra} = 10^3$ and $\mathrm{Ra} = 10^4$ shows good agreement overall. The percentage error difference for the predicted values of the maximum horizontal velocity along the vertical centerline (u_{max}) of the enclosure, and the maximum vertical velocity (v_{max}) along the horizontal centerline with the benchmark solutions of de Vahl Davis [158], ranges from 0.01% to 3.60 %, which is good. However, for positions (x), the percentage error difference is 11%. The percentage difference is indicative of potential numerical discretization approximation errors.

The variables in Tables 4.3 and 4.4 are non-dimensional. The dimensionless values of the positions were obtained by dividing the positions by the cavity height, while the non-dimensional velocities were calculated by dividing the product of the velocities and the cavity height by the thermal diffusivity. The equations used to determine the non-dimensional parameters are presented in Equation (3.22).

*Table 4-3: Comparison of horizontal velocity (with position) and vertical velocity (with position) with benchmark solutions (*Ra = 10^3*)*

S/n	Source	u_{max} (Ra = 10^3)	Position (y)	v_{max} (Ra = 10^3)	Position (x)
1	Present study	3.621	0.80	3.835	0.20
2	de Vahl Davis [158]	3.649	0.813	3.697	0.178
3	de Vahl Davis and Jones [170]	2.10 – 3.75	0.75 – 0.88	2.10 – 3.77	0.125 – 0.205
4	Wan, et al. [171]	3.489	0.813	3.686	0.188
5	Sarler [172]	3.544	-	3.566	-
6	Kosec and Sarler [173]	3.653	0.812	3.699	0.177
7	Markatos and Pericleous [174]	3.544	0.832	3.593	0.168
8	Tian et al. [175]	3.605	-	3.689	-
9	Projahn et al. [176]	3.7	0.825	3.770	0.175

*Table 4-4: Comparison of horizontal velocity (with position) and vertical velocity (with position) with benchmark solutions (*Ra = 10^4*)*

S/n	Source	u_{max} (Ra = 10^4)	Position (y)	v_{max} (Ra = 10^4)	Position (x)
1	Present study	16.01	0.80	19.62	0.10
2	de Vahl Davis [158]	16.18	0.823	19.62	0.119
3	de Vahl Davis and Jones [170]	15.24 - 21	0.781 – 0.883	19.17 – 26.30	0.094 – 0.145
4	Wan et al. [171]	16.17	0.823	19.79	0.120
5	Sarler [172]	15.80	-	19.04	-
6	Kosec and Sarler [173]	16.27	0.825	19.83	0.120
7	Markatos and Pericleous [174]	16.18	0.832	19.44	0.113
8	Tian et al. [175]	16.16	-	19.63	-
9	Projahn et al. [176]	16.20	0.883	19.56	0.110

The results of velocity, temperature, and the position at which they occur from the numerical model were obtained locally at the specified node positions and compared with benchmark solutions of de Vahl Davies [158] along with other publications that validated their results against de Vahl Davies [158]. The benchmark solution by de Vahl Davies [158] is numerical, but popular and widely used by researchers as benchmark results. Also, the results of the benchmark solution were validated with experimental work by Krane and Jesse [177]. The percentage error for the compared data is calculated and tabulated along with results in Tables 4.5 and 4.6.

Table 4-5: Percentage difference for comparison of horizontal velocity (with position) and vertical velocity (with position) with benchmark solutions (Ra = 10^3)

Source	u_{max} (Ra = 10^3)	Position (y)	v_{max} (Ra = 10^3)	Position (x)
Present study	3.621	0.80	3.835	0.20
de Vahl Davis [158]	3.649	0.813	3.697	0.178
Percentage difference (%)	0.77	1.61	3.66	11.64

Table 4-6: Percentage difference for comparison of horizontal velocity (with position) and vertical velocity (with position) with benchmark solutions (Ra = 10^4)

Source	u_{max} (Ra = 10^4)	Position (y)	v_{max} (Ra = 10^4)	Position (x)
Present study	16.017	0.829	19.619	0.110
de Vahl Davis [158]	16.178	0.823	19.617	0.119
Percentage difference (%)	1.00	0.73	0.01	7.86

The percentage error is calculated by taking a ratio between the absolute difference between the numerical solution and the benchmark solution and the average of the benchmark

solution and the numerical solution. The percentage difference equation is presented in Equation (4.10).

$$\text{Percentage difference} = \left(\frac{|\emptyset_n - \emptyset_b|}{\left[\frac{\emptyset_n + \emptyset_b}{2}\right]}\right) \times 100 \tag{4.10}$$

where $\emptyset_n$ and $\emptyset_b$represent results of the numerical variable (velocity, temperature), and results of the benchmark variable (velocity, temperature), respectively. The validated results are non-dimensional and calculated in-line with non dimensional variables used in the benchmark solution of de Vahl Davies [158].

Recent studies in second law analysis have indicated that entropy has both traditional physical characteristics and computational characteristics. In addition to physical processes of heat transfer and viscous dissipation, CFD procedures may destroy (or produce) computational entropy due to artificial dissipation, discretization errors, and implausible numerical results [3,4]. The differential equations solutions for the conservation of mass, momentum, and energy that do not satisfy the second law could be characterized by oscillations, a lack of uniqueness, or other unusual behavior [121]. The total entropy generation computed from a numerical formulation entails a sum of the computational and physical entropy production. This unique characteristic of the entropy can potentially serve as a physically based parameter which can indicate physically unrealistic solutions and discretization errors in computational thermofluids.

This perspective has been demonstrated by various entropy computations applications. For example, entropy computations have been applied to numerical error, convergence criteria, and time-step constraints. The second law analysis was used to show that the condition for

which the Courant, Freidrichs, and Lewy (CFL) parameter attains numerical stability directly relates to the second law under conditions that the diffusive transport is negligible and source term is constant.

The discretized entropy equation can be used as a method of ensuring nonlinear stability. Merrian [127] showed that a restrictive condition based on a positive entropy generation rate in each control volume is adequate to guarantee the stability of a scheme. Numerical experiments have been presented to indicate that stable solutions which do not satisfy the entropy constraint may obtain quantitatively incorrect results [5]. The second law can also be used to improve the reliability of upwinding schemes.

In Chapter 5 of this thesis, a Second Law formulation based on a new parameter called the "apparent entropy production difference" will be presented and applied to numerical error characterization [7,178]. In Chapter 6 the use of entropy-based artificial viscosity as a corrective mechanism to potentially reduce solution errors and enhance numerical accuracy will also be discussed.

The temperature field from the simulations with a Grashof number of 10^4, Prandtl number of 6.2, and nanoparticle volume fraction of 20%, were examined, as well as a Grashof number of 10^5, Prandtl number of 6.2, and nanoparticle volume fraction of 5%. The results were compared and validated against past published data by Khanafer et al. (2003), as shown in Figure 4.6.

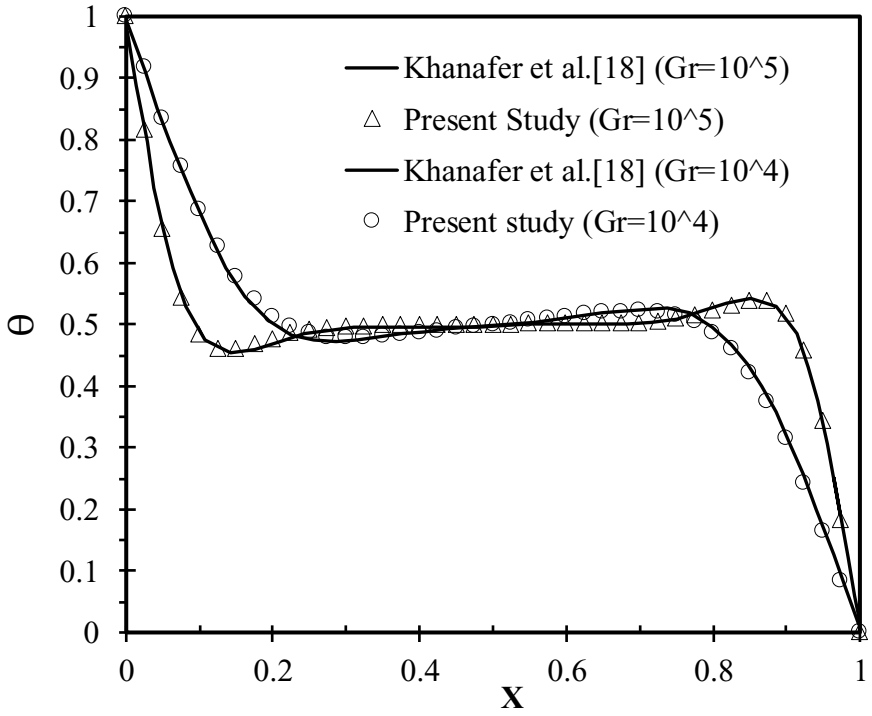

*Figure 4-6: Comparison of temperature distribution with past published results (*Gr = *10^4, Ø=20%,* Pr = *6.2 and* Gr = *10^5, Ø=5%,* Pr = *6.2)*

Predictions were validated with experimental results of Krane and Jesse (1983). The results are validated locally as the temperature results were obtained locally from nodal points along the horizontal mid-plane. The validation is done at the local nodes along the mid-plane based on available experimental/benchmark results.

4.4 Cases 1 and 2: Natural Convection in Cavity

Two case studies were considered for natural convection (Figures 4.1 and 4.2). An adiabatic boundary condition is assumed for the top and bottom walls of the enclosure for both cases. The vertical walls for Case 1 are maintained at isothermal conditions. The left wall is held at a constant high temperature, while the right wall is maintained at a constant low temperature. For Case 2, the left wall is maintained at a constant heat flux while the right

wall boundary is maintained at a low temperature. The boundary conditions for the natural convection case studies are defined as follows.

$$\frac{\partial T}{\partial \vec{n}} = 0, v = u = 0 \qquad for\ y = 0, H\ and\ 0 \le x \le L$$

$$T = T_h, v = u = 0\ \ or\ \ v = u = 0,\ \frac{\partial T}{\partial \vec{n}} = -\frac{k_f}{k_{nf}} \quad for\ x = 0\ and\ 0 \le y \le H$$

$$T = T_c, v = u = 0 \quad or \quad v = u = 0, T = T_c \qquad for\ x = L\ and\ 0 \le y \le H$$

(4.11)

For Case 1, the effects of the nanoparticle volume fraction on the effective thermal conductivity and dynamic viscosity are presented in Figure 4.7. The results illustrate that the effective thermal conductivity of the nanofluid increases when the nanoparticle volume fraction is increased. When the effective thermal conductivity of the nanofluid is increased, the heat transfer rates also increase [79]. The results indicate that the heat transfer of the nanofluid is significantly enhanced by the addition of Aluminium oxide nanoparticles to the base fluid (water) to form the Al_2O_3-water nanofluid. A 10% increase in the nanoparticle volume fraction yields a 31.7% increase in the effective thermal conductivity of the nanofluid.

The variation of dynamic viscosity with nanoparticle volume fraction is also presented in Figure 4.7. It can be observed that an increase in the nanoparticle volume fraction enhances the dynamic viscosity. Furthermore, the dynamic viscosity increases by 30.1% with a 10% increase in the nanoparticle volume fraction. Since fluid friction is a function of viscosity, and a source of flow irreversibility, the result implies that an increase in the dynamic

viscosity due to the addition of nanoparticles will yield an increase in the rate of entropy production due to fluid friction irreversibilities. The effective thermal conductivity is the ratio of the thermal conductivity of the nanofluid and the thermal conductivity of the base fluid. It is dimensionless.

A schematic for Case 2 is presented in Figure 4.2. The effect of the nanoparticle volume fraction on the effective thermal conductivity and entropy production is compared for different nanofluids (Al_2O_3-water, Cu-water, and TiO_2-water) and presented in Figures 4.8 and 4.9. The aspect ratio sensitivity is also studied for this case.

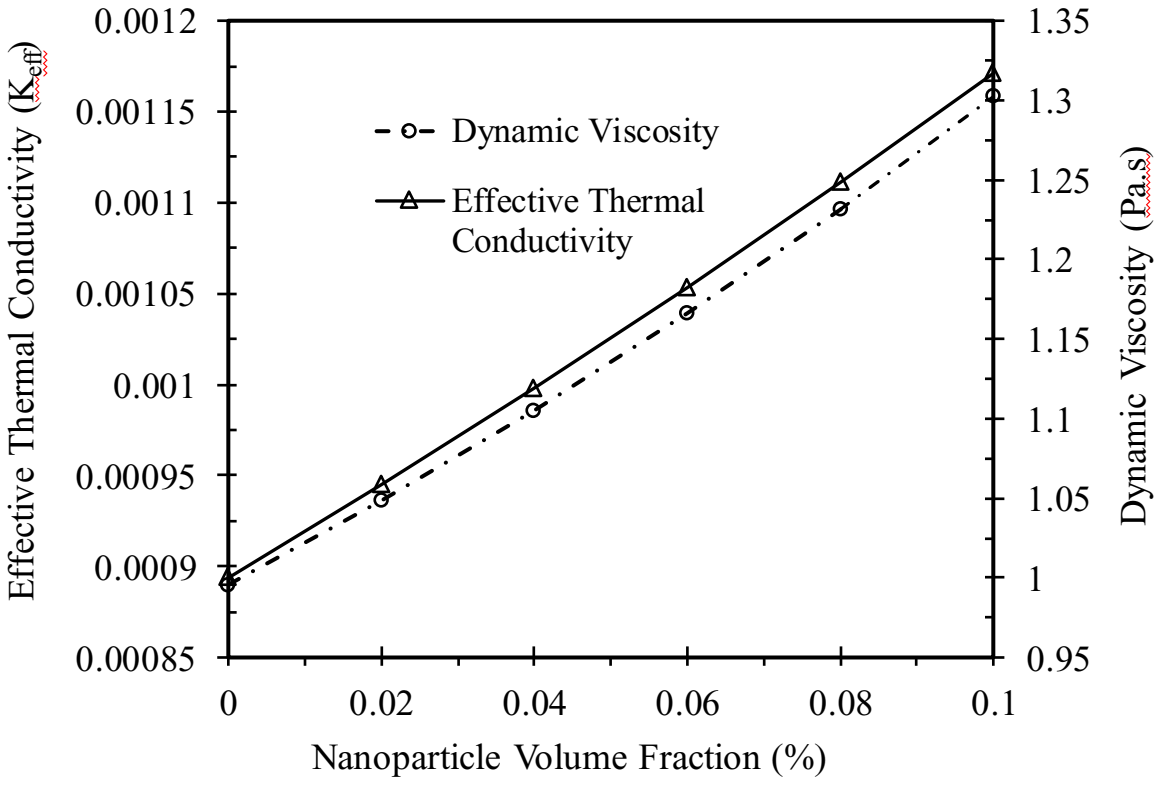

Figure 4-7: Variation of effective thermal conductivity and dynamic viscosity with nanoparticle volume fraction

Figure 4.8 compares the effective thermal conductivity for the different nanofluids. It can be observed that the Cu-water nanofluid has the highest effective thermal conductivity, and next is the Al_2O_3-water nanofluid, while the TiO_2-water nanofluid has the lowest effective thermal conductivity. Therefore, the Cu-water nanofluid yields the most effective heat transfer relative to other nanofluids, followed by the Al_2O_3-water nanofluid, while the TiO_2-water nanofluid yields the least heat transfer.

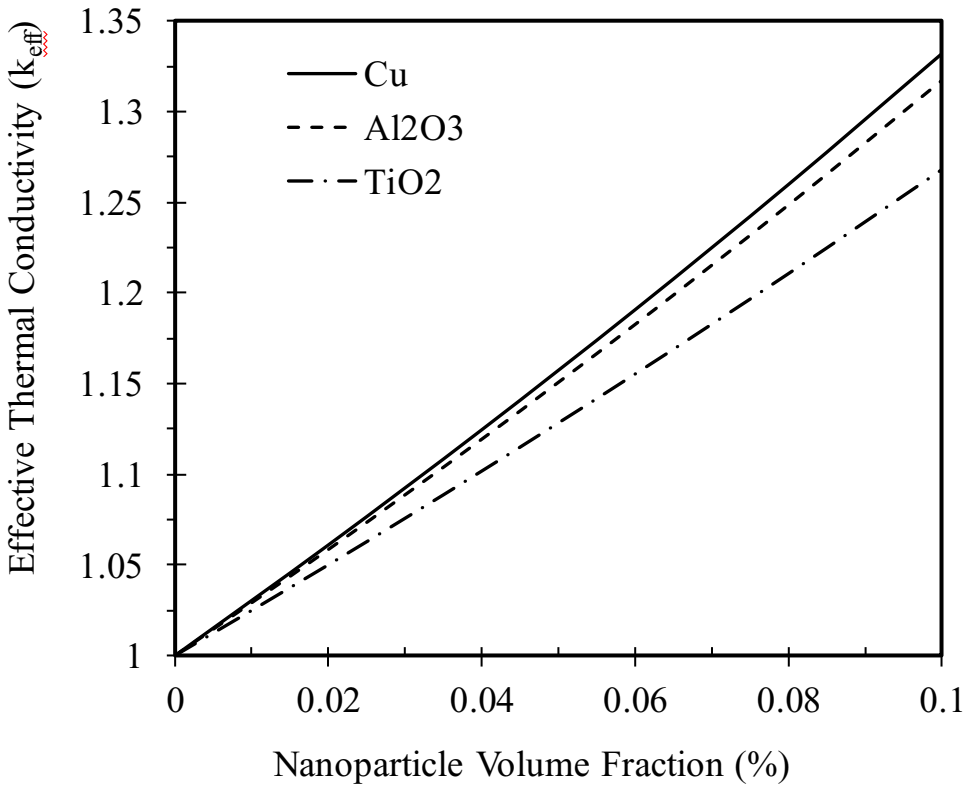

Figure 4-8: Variation of effective thermal conductivity with nanoparticle volume fraction for different nanoparticle types

Figure 4.9 compares the results of the variation of total entropy production as the nanoparticle volume fraction is increased. The total entropy production decreases with an

increase in the nanoparticle volume fraction. In contrast to the effective thermal conductivity results in Figure 4.8, the Cu-water nanofluid yielded the minimum total entropy production among the nanofluids, followed by the Al_2O_3-water nanofluid. The TiO_2-water nanofluid produced the highest total entropy production over the range of nanoparticle volume fractions. When the nanoparticles are added to the base fluid, there will be a corresponding increase in the effective thermal conductivity, leading to a reduction in the temperature gradient, thereby resulting in a decrease of the total entropy production.

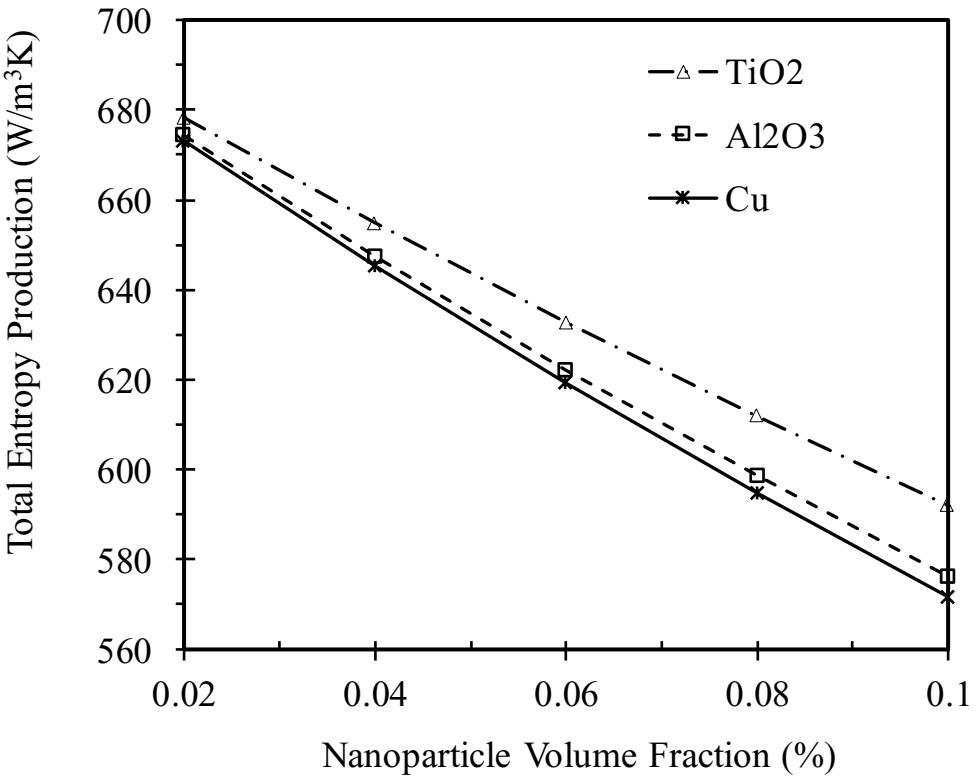

Figure 4-9: Variation of entropy production with nanoparticle volume fraction for different nanoparticle types

In this case, the entropy production due to thermal irreversibilities is higher than fluid friction irreversibilities as a result of weak buoyancy induced flow and the enhanced thermal conductivity. The rate of entropy production with units of W/m^3K is volumetric entropy, which is entropy production per unit volume.

From Figures 4.8 and 4.9, it can be seen that, generally, for all nanofluid types, the variation of the nanoparticle volume fraction produces an opposite effect on the effective thermal conductivity and the total entropy production. While the effective thermal conductivity increases with an increase in the nanoparticle volume fraction, the total entropy production decreases.

Figure 4.10 presents results of the average Nusselt number (Nu_{avg}) on the hot wall for various nanoparticle volume fractions and Grashof numbers. A linear variation of the average Nusselt number with the nanoparticle volume fraction is observed in Figure 4.10. The trend in Figure 4.10 indicates that the addition of nanoparticles to the fluid enhances the heat transfer rate, hence this increases the Nusselt number by 17% for a Grashof number of 10^3, and 19% for a Grashof number of 10^5. This enhancement of the average Nusselt number by nanofluids plays a potentially significant role in cooling system applications such as electronics cooling.

The Nusselt number of nanofluids usually depends on a few factors such as thermal conductivity, the nanoparticle volume fraction, the heat capacitance of both the nanoparticles and pure fluid, the flow structure, the nanofluid viscosity, and the dimensions of the particles.

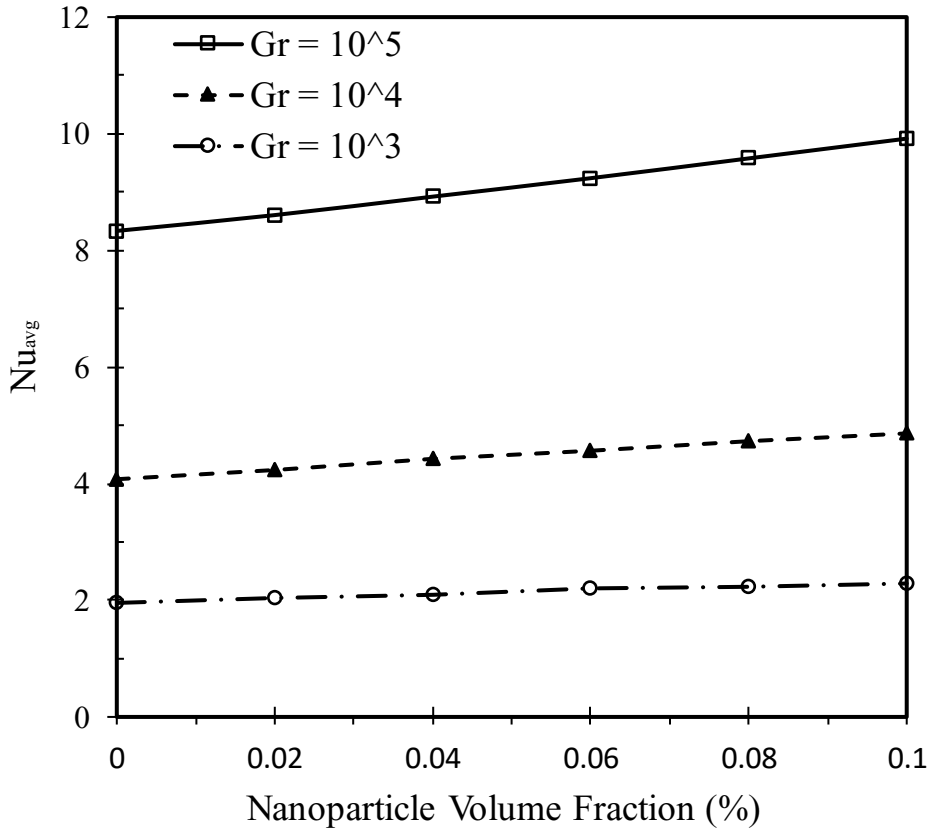

Figure 4-10: Variation of average Nusselt number with nanoparticle volume fraction for different Grashof number

Figure 4.11 illustrates the effect of aspect ratio on entropy production for the different nanofluids. It is observed that an increment in the aspect ratio of the enclosure increases the rate of entropy production. When the aspect ratio of the rectangular enclosure is increased, the area with a constant heat flux and low wall temperature (left and right walls) is increased, while the insulated area (upper and bottom walls) is reduced. Consequently, an increase in the heat flux area relative to the insulated area will produce a higher temperature gradient, larger heat transfer irreversibilities, and a higher entropy production rate.

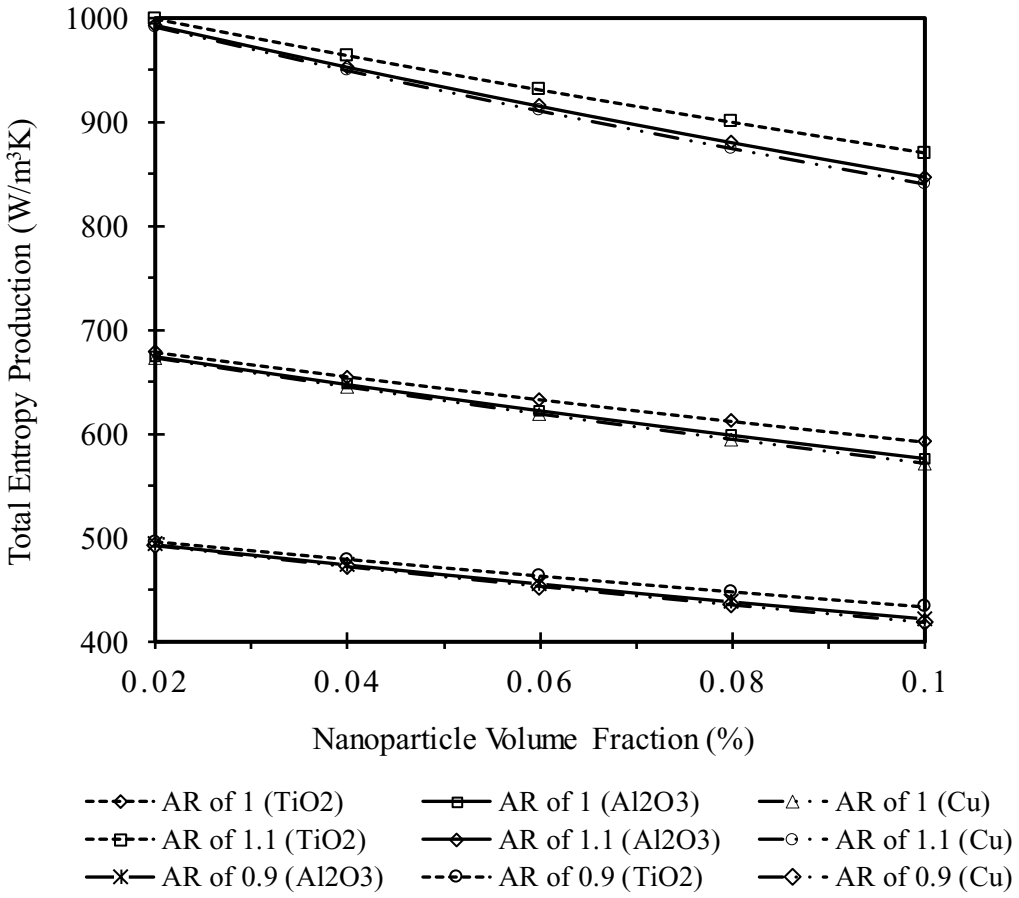

Figure 4-11: Effect of aspect ratio on total entropy production for different nanoparticle types

Figure 4.12 shows the isotherms of the simulation for the case of $\mathrm{Ra} = 10^3 - 10^5$ and $\mathrm{Pr} = 0.71$. The temperature profile is almost linear at the smallest Rayleigh number (10^3). An increase in the Rayleigh number leads to a corresponding increase in the convection flow where the profiles exhibit a more progressive departure from linearity. The isotherms flatten as the Rayleigh number increases, with the highest temperature drop observed closer to the wall. This trend arises due to the increasing buoyancy-induced motion of the fluid.

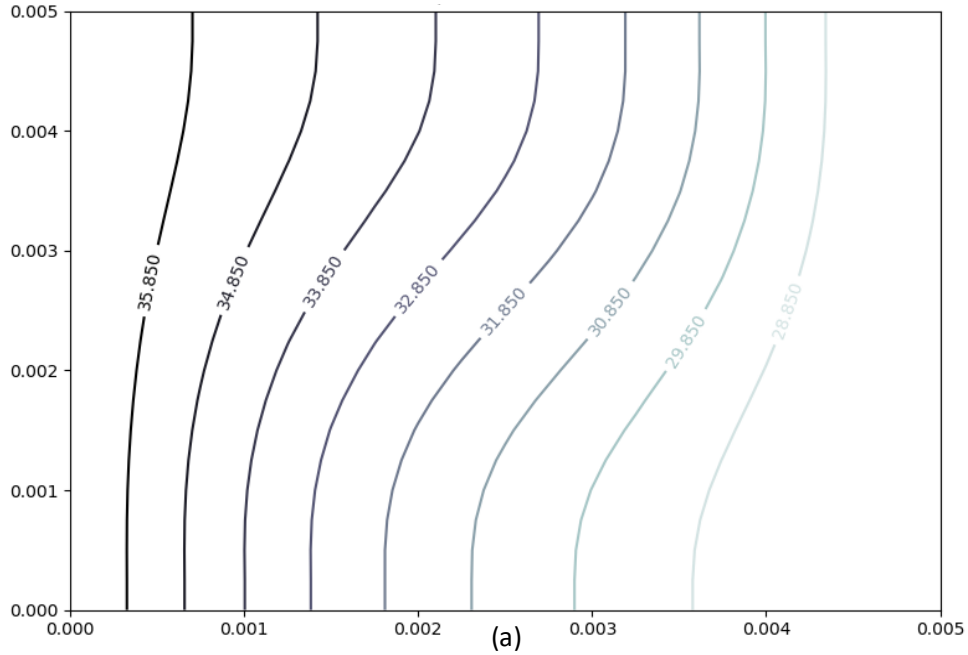
0.005
0.004
0.003
0.002
0.001
0.000
0.000
0.001
0.002
0.003
0.004
0.005
35.850
34.850
33.850
32.850
31.850
30.850
29.850
28.850

(a)

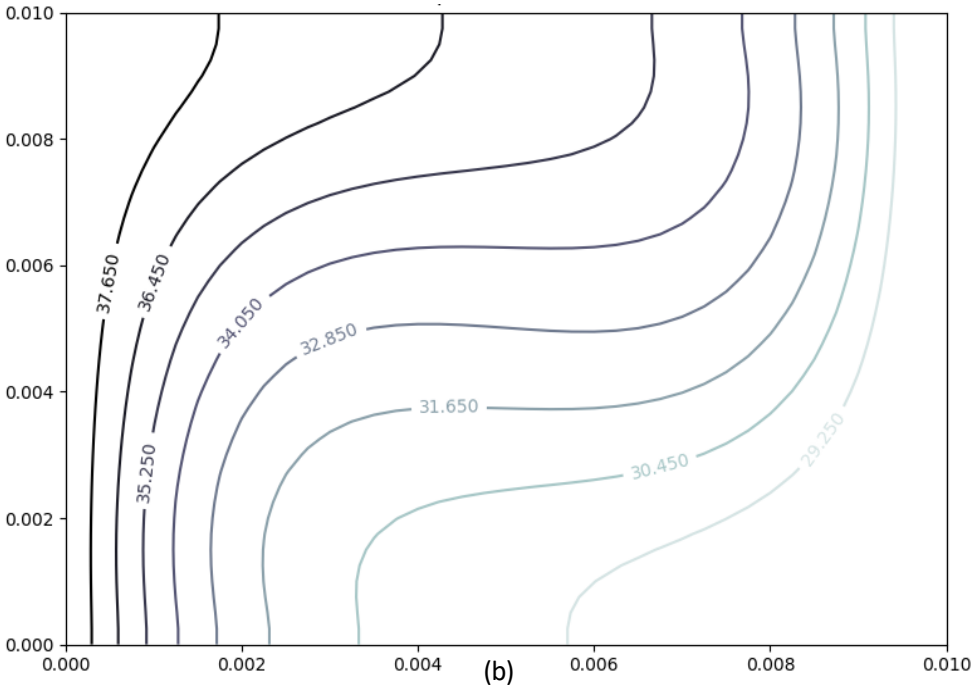
0.010
0.008
0.006
0.004
0.002
0.000
0.000
0.002
0.004
0.006
0.008
0.010
37.650
36.450
35.250
34.050
32.850
31.650
30.450
29.250

(b)

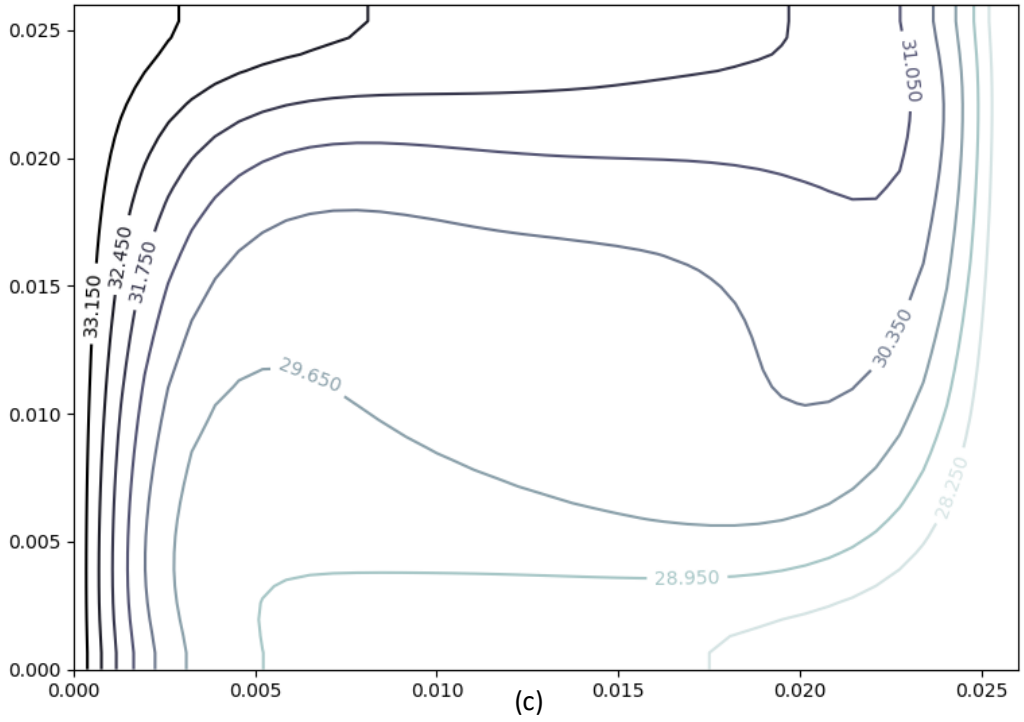

Figure 4-12: Isotherms for (a) Ra=10^3 *(b)* Ra=10^4 *and (c)* Ra=10^5 *with Pr = 0.71*

Figure 4.13 shows the predicted velocity field for Rayleigh numbers of $10^3 - 10^5$ and $\mathrm{Pr} = 0.71$. At the lowest Rayleigh numbers in Figure 4.13 (a), the fluid flow is nearly symmetrical about the center point. An increase in the Rayleigh number results in a more elliptical recirculation which eventually separates into two regions at $\mathrm{Ra} = 10^5$, as illustrated by Figure 4.13 (c).

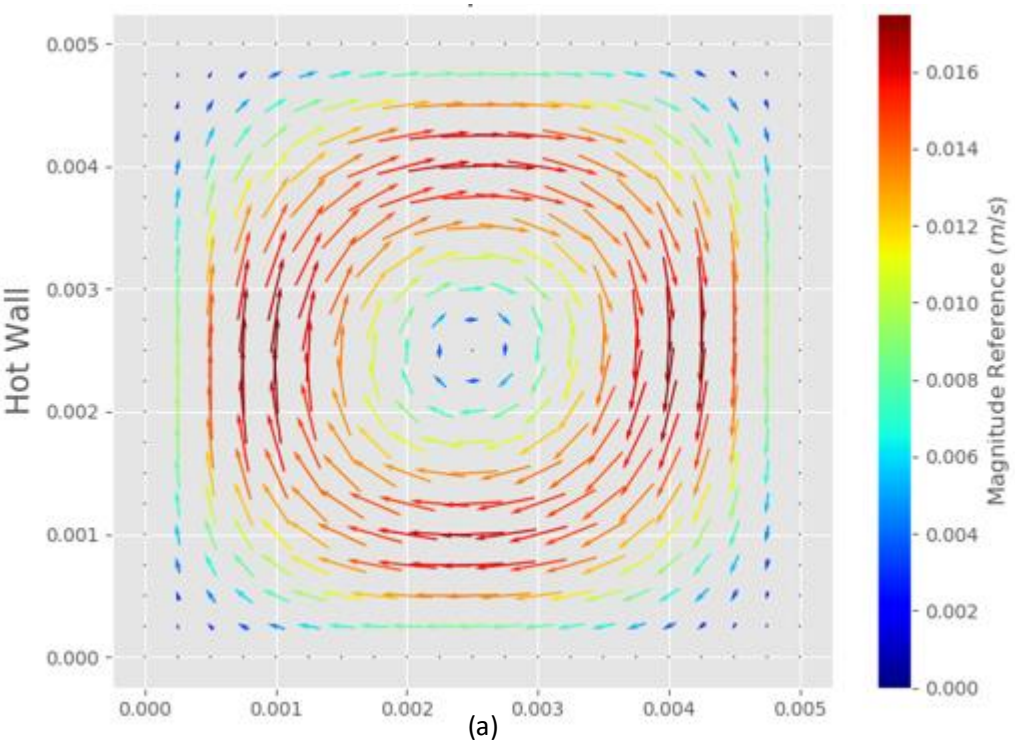
Hot Wall
0.005
0.004
0.003
0.002
0.001
0.000
0.000
0.001
0.002
0.003
0.004
0.005
Magnitude Reference (m/s)
0.016
0.014
0.012
0.010
0.008
0.006
0.004
0.002
0.000

(a)

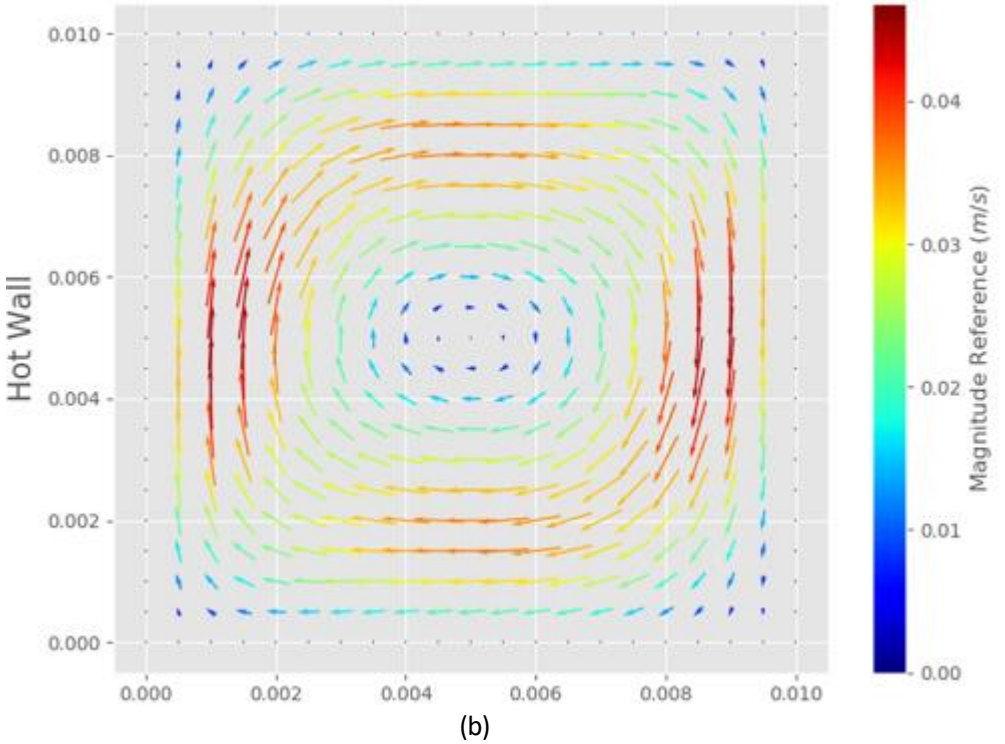
Hot Wall
0.010
0.008
0.006
0.004
0.002
0.000
0.000
0.002
0.004
0.006
0.008
0.010
Magnitude Reference (m/s)
0.04
0.03
0.02
0.01
0.00

(b)

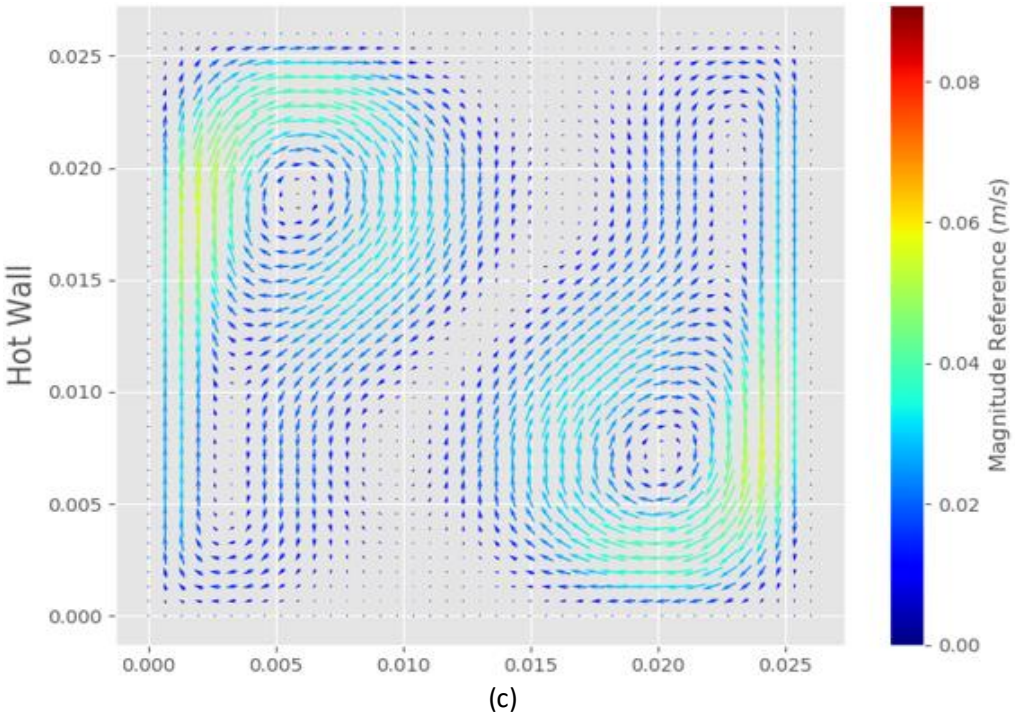

Figure 4-13: Velocity fields for (a) Ra=10^3 *(b)* Ra=10^4 *and (c)* Ra=10^5 *with* Pr = *0.71*

Error! Reference source not found. presents the predicted local positive definite entropy p roduction field for isothermal walls and a temperature difference of (a) 10 °C, (b) 15 °C, and (c) 20 °C at Pr = 0.71. The temperature difference is obtained as the difference between the temperature of the hot wall, T_h and that of the cold wall, T_c. It was observed that more entropy is produced in the regions with a higher temperature difference in the fluid and in regions with viscous dissipation due to buoyancy-induced motion of the fluid. The results also indicate that as the temperature difference across the isothermal walls increases, the rate of entropy production also increases.

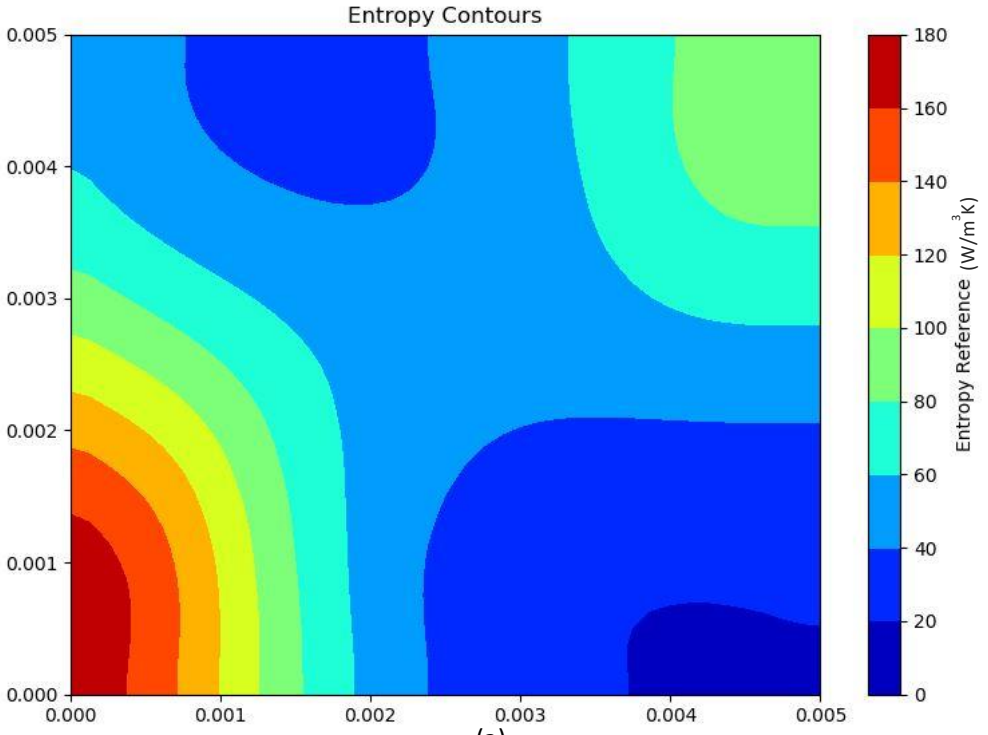
Entropy Contours
0.005
0.004
0.003
0.002
0.001
0.000
0.000
0.001
0.002
0.003
0.004
0.005
180
160
140
120
100
80
60
40
20
0
Entropy Reference (W/m3K)

(a)

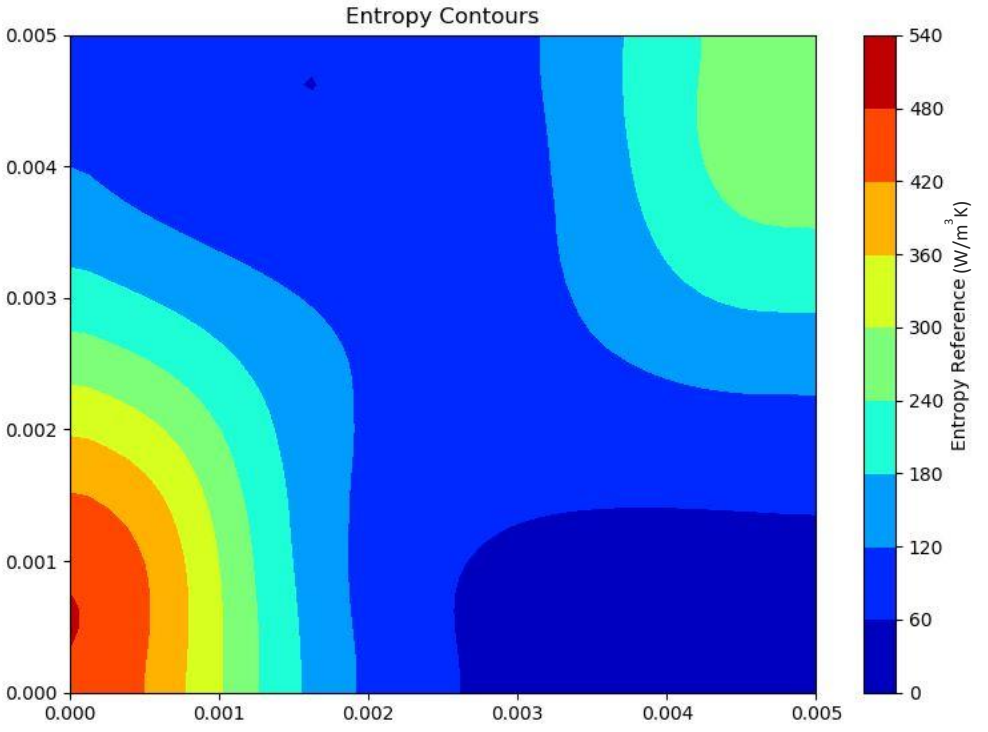
Entropy Contours
0.005
0.004
0.003
0.002
0.001
0.000
0.000
0.001
0.002
0.003
0.004
0.005
540
480
420
360
300
240
180
120
60
0
Entropy Reference (W/m3K)

(b)

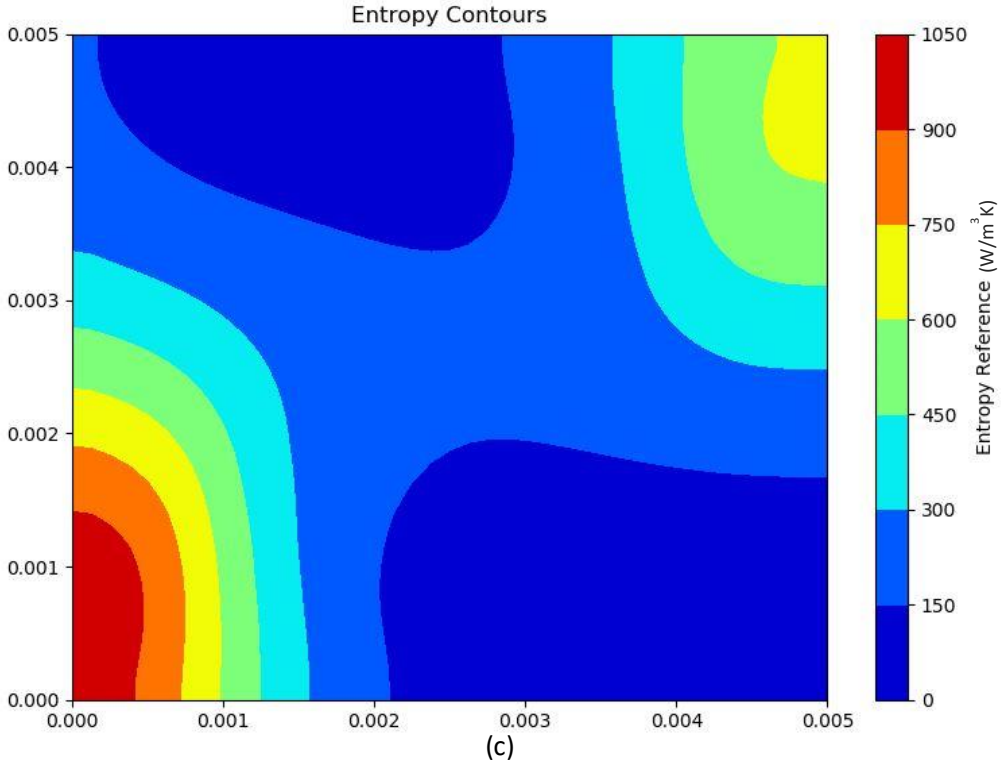

Figure 4-14: Positive definite entropy production field maps for isothermal walls and temperature difference of (a) 10 °C, (b) 15 °C, and (c) 20 °C at Pr = 0.71

4.5 Case 3 and 4: Mixed Convection in Cavity

Schematic diagrams for the mixed convection case studies (Cases 3 and 4) are presented in Figures 4.15 and 4.16. Case 3 is mixed convection of nanofluids in a lid-driven cavity (Figure 4.15). The top and bottom walls of the cavity are insulated. The lid of the cavity is driven at a constant initial velocity, u_o. The vertical walls are isothermal. The right wall is kept at a constant low temperature, while the left wall is maintained at a constant high temperature. The boundary conditions for this problem are defined as follows:

$$\frac{\partial T}{\partial \boldsymbol{n}} = 0; \quad v = u = 0 \qquad for\ y = 0\ and\ 0 \leq x \leq L$$

$$\frac{\partial T}{\partial \boldsymbol{n}} = 0; \quad v = 0, u = u_o \qquad for\ y = H\ and\ 0 \le x \le L$$

$$T = T_h; \quad v = u = 0 \qquad for\ x = 0\ and\ 0 \le y \le H$$

$$T = T_c; \quad v = u = 0 \qquad for\ x = L\ and\ 0 \le y \le H$$

(4.12)

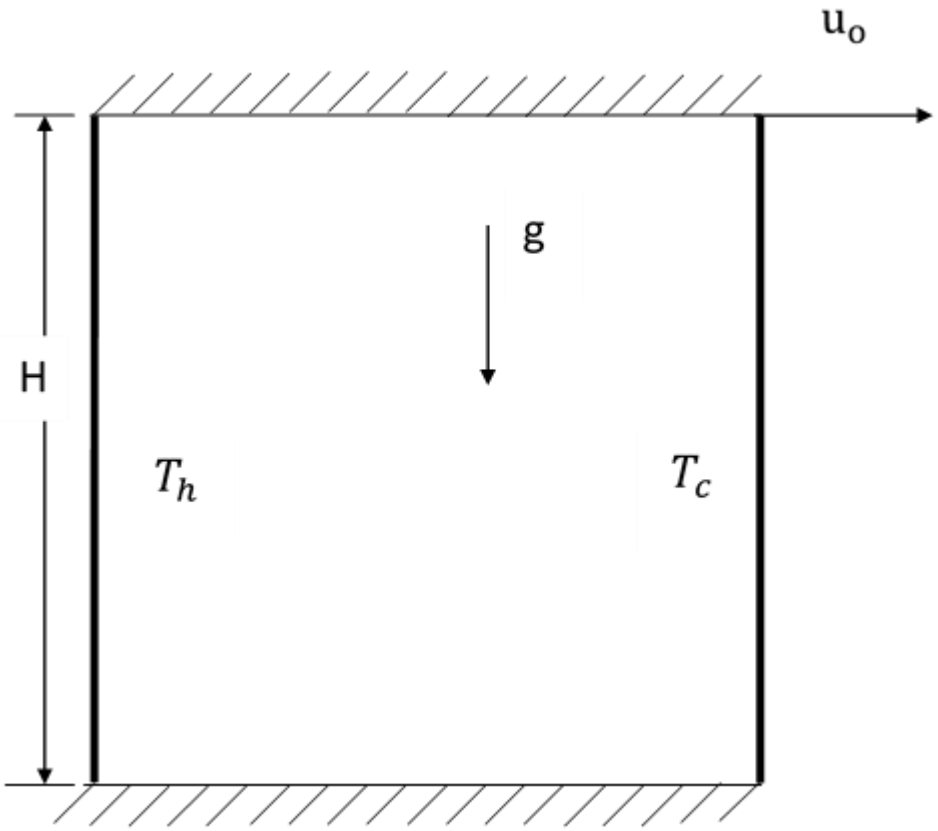

Figure 4-15: Schematic for Lid-Driven Cavity - Case 3 (Pr = 6.2)

In Case 4 (Figure 4.16), the upper and lower boundary walls are insulated. The left boundary is held at a constant low temperature as a moving wall with a constant velocity

v_w, while the right boundary wall is maintained at a constant heat flux. The boundary conditions for this mixed convection case are defined as follows.

$$\frac{\partial T}{\partial \vec{\boldsymbol{n}}} = 0, v = u = 0 \qquad for\ y = 0, H\ and\ 0 \le x \le L$$

$$T = T_c, v = v_w, u = 0 \qquad for\ x = 0\ and\ 0 \le y \le H$$

$$\frac{\partial T}{\partial \vec{n}} = -\frac{k_f}{k_{nf}}, v = u = 0 \qquad for\ x = L\ and\ 0 \le y \le H$$

(4.13)

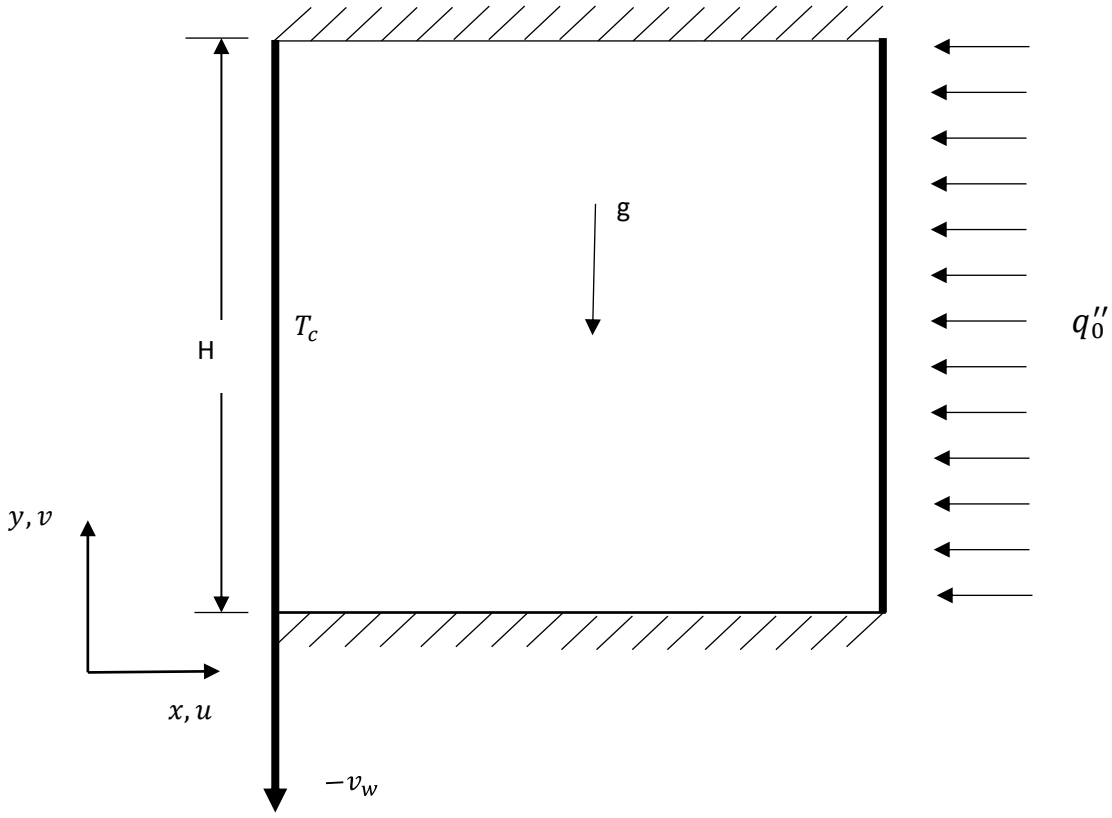

Figure 4-16: Schematic of mixed convection case study – case 4

Figures 4.17 (a) and (b) show the change in the average Nusselt number on the hot wall (left wall) with the nanoparticle volume fraction as a function of Rayleigh number and Reynolds number. Figure 4.17 (a) illustrates the variation in average Nusselt number with nanoparticle concentration at Re =10. Figure 4.17 (b) presents the change in average Nusselt number with nanparticle volume fraction when Re = 100. The increase of the nanoparticle concentration enhances the effective thermal conductivity and therefore the heat transfer. As nanoparticles are added to the base fluid, the flow intensity increases, and the heat transfer rate is induced, hence increasing the Nusselt number. In addition, an increase in the Reynolds number means a higher velocity of the top lid, which leads to increased forced convection, and thus the Nusselt number.

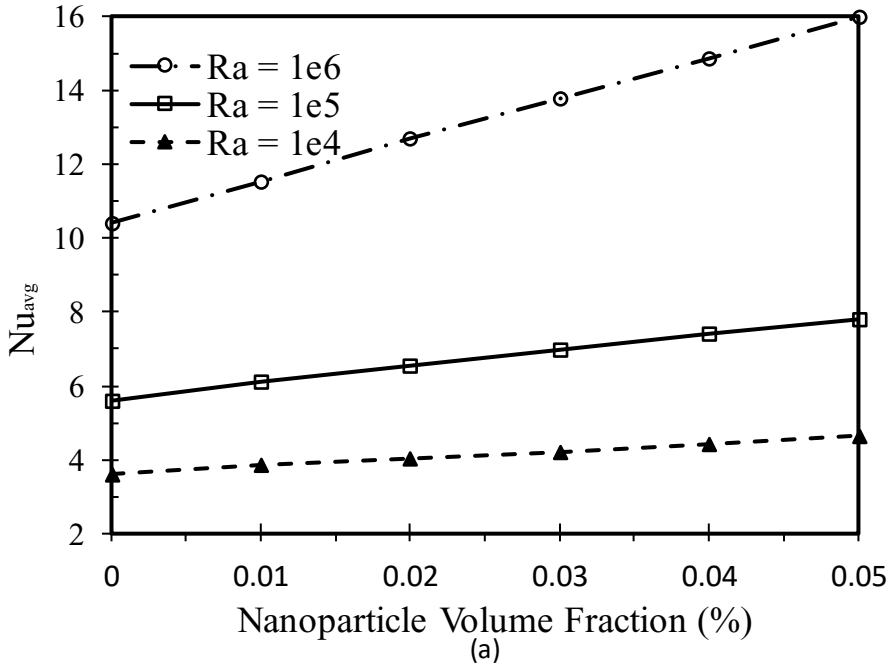

(a)

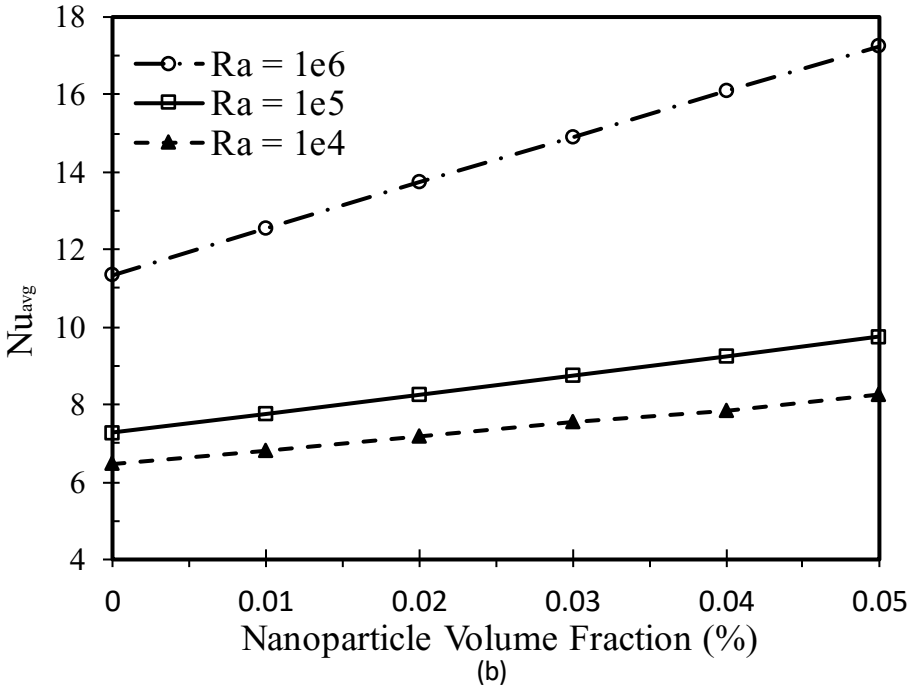

Figure 4-17: Variation of Nusselt number with nanoparticle volume fraction for different Rayleigh numbers and Reynolds numbers (a) Re =10 (b) Re = 100

The use of nanofluids instead of a base fluid, by increasing the nanoparticle volume fraction from 0 to 5%, significantly enhances the Nusselt number by 53% at Ra = 10^6 and 29% at Ra = 10^4 for Re = 10. For Re = 100, the use of nanofluids instead of a base fluid enhances the Nusselt number by 52% at Ra = 10^6 and 27% at Ra = 10^4.

A Second Law analysis is performed to find the optimal nanoparticle fraction for which the entropy production is minimized. Figure 4.18 illustrates the variation of entropy production with nanoparticle volume fraction as a function of the wall velocity, v_w. The results for the optimal nanoparticle volume fraction that minimizes the entropy production are presented in Table 4.7.

The addition of nanoparticles to the base fluid increases the effective thermal conductivity of the nanofluid, leading to a reduction in the temperature gradient and entropy production due to thermal irreversibilities. This explains the downward trend in the curve. On the other hand, the addition of nanoparticles to the base fluid will enhance the fluid viscosity and result in an increase of the entropy production due to friction irreversibilities which leads to the other upward trend in the curve. The temperature gradients, as well as the entropy generation due to heat transfer across the temperature difference in the fluid is computed by the first term in Equation (3.18). The second term refers to the local entropy production due to viscous dissipation. The results of total entropy production presented in Figure 4.18 are calculated by Equation (3.18).

As the wall velocity increases, heat is removed from the system, thereby reducing entropy production due to thermal irreversibilities, whereas the increase in the wall velocity will enhance the fluid friction and produce higher entropy production due to friction irreversibilities. This explains the different trends observed in Figure 4.18.

The optimal wall velocity for which the total entropy production is minimized was also predicted. As shown in Table 4.7, a wall velocity of approximately -0.50 m/s produced the minimum entropy production of 388,213 W/m^3K. It is observed that the optimal wall velocity also represents an inflection point in the total entropy production rate as illustrated in Table 4.7 and Figure 4.18. The aim of studying the entropy production rate in a mixed convention of nanofluids is to obtain the optimum nanoparticle concentration and wall velocity for which the entropy production is minimized in a mixed convection system.

These optimum parameters are important because they can be used to maintain the minimum irreversibilities in a system, as shown in Tables 4.7 and 4.18.

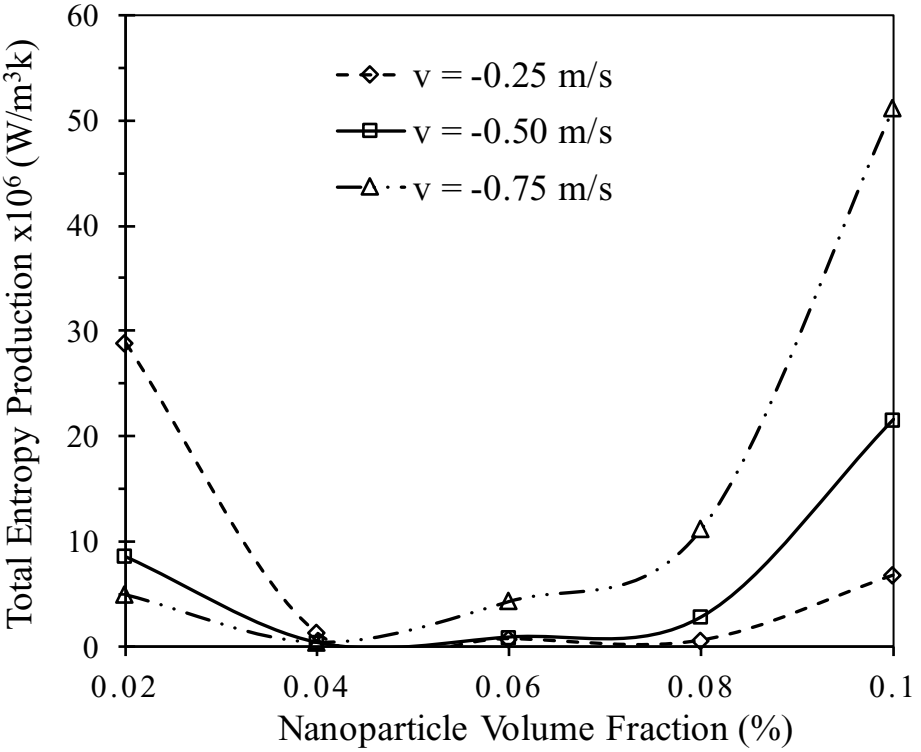

Figure 4-18: Variation of entropy production with nanoparticle volume fraction as a function of wall velocity

Table 4-7: Optimal values of nanoparticle volume fraction and entropy production as a function of wall velocity

Wall Velocity (m/s)	Optimal Volume Fraction (%)	Minimum Entropy Production (W/m^3K)
-0.25	0.04	410205
-0.50	0.04	388213
-0.75	0.08	624532

The entropy and Second Law analysis for natural and mixed convection systems involving nanofluids can be potentially applied to nanofluid-based solar thermal collectors. For example, based on the minimum entropy production, an optimum nanoparticle volume fraction can be obtained, and the pumping power of a nanofluid-based solar thermal collector can potentially be optimized. Also, the entropy production studies can be applicable in comparing the heat transfer enhancement and measure of irreversibilities at various nanoparticle concentrations for different nanofluids types. This is essential for the selection of a nanofluid type that is best suited (for example, a nanofluid type with high heat transfer enhancement, and minimum entropy production) for a system.

4.6 Conclusion

This chapter presented a new approach for how entropy and the Second Law of Thermodynamics can be used as effective tools for the energy efficiency improvement and numerical modeling of thermofluid systems. Previous conventional methods generally detect energy losses on a system-wide basis. With such approaches, the margins for improving the efficiency for existing devices are often relatively small. However, entropy-based methods track energy losses locally and therefore can offer higher levels of system efficiency and energy savings in various applications.

A numerical investigation of heat transfer and entropy production for natural and mixed convection in rectangular enclosures using air, water, as well as nanofluids as the working fluid was reported in this chapter. For the study with nanofluids, an optimum nanoparticle volume fraction for which entropy production is minimized was determined. The chapter also presented comparisons of the natural convection heat transfer and entropy production

for different nanofluids in the cavity to obtain the optimal nanofluid that is best suited for each system. The heat transfer rates and entropy production for Cu-water, Al_2O_3-water, and TiO_2-water nanofluids in the enclosure were compared. The results showed an increase in heat conduction and a reduction in the rate of entropy production when the nanoparticle volume fraction increases. Among the nanofluids compared, Cu-water was found to produce the best heat transfer performance and lowest entropy production.

The results for an aspect ratio sensitivity study were also presented. It was also observed that the total entropy generation increases with an increase in the aspect ratio of the cavity. The analysis for the mixed convection case was presented in this chapter. It showed that an optimum value of the nanoparticle volume fraction can be achieved, as well as a wall velocity, for which the total rate of entropy production is minimized.

In general, Chapter 4 presented a new approach for the application of the Second Law, entropy generation minimization and heat transfer enhancement in mixed and natural convection of nanofluids in cavities. The next chapter will present the application of the Second Law and entropy production as a numerical error indicator in numerical heat transfer.

5 ENTROPY-BASED ERROR CHARACTERIZATION IN NUMERICAL HEAT TRANSFER

5.1 Overview

This section presents another novel application of the entropy production formulation. An entropy-based error indicator will be used to assess the solution accuracy of fluid flow simulations with heat transfer using the Second Law. The control-volume-based finite-element method (CVFEM) is used to discretize and solve the governing equations. Then the numerical procedure computes and compares the local entropy production rates obtained from the two forms of the discretized Second Law – or the transport and positive-definite forms of the entropy transport equation. The computed local entropy generation rates from both methods are compared and related to expected numerical errors from the benchmark solutions.

In previous chapters, each of the case studies have offered a unique perspective of how entropy generation and the Second Law can provide useful design insights for the improvement of system thermal performance. Furthermore, entropy generation has both physical and computational characteristics. In addition to the physical processes of heat transfer and viscous dissipation, CFD models may destroy or produce entropy due to numerical discretization through approximation errors that lead to non-physical numerical results, artificial dissipation, and other discretization errors [3, 4]. Numerical simulations which do not satisfy a prescribed entropy constraint may yield non-physical results [6]. Appropriate steps may be adopted to overcome these anomalies, for example, the specific

form of a convective upwinding scheme can be modified appropriately to satisfy the entropy constraint and improve the overall accuracy of the model [3]. The entropy constraint is constructed based on alternate positive-definite and entropy transport forms of the Second Law along with the Gibbs equation [6].

In this chapter, a Second Law formulation will be analyzed based on different forms of the positive-definite and entropy transport equations. In order to assess the numerical error, a new parameter called the "apparent entropy production difference" will be computed based on the difference between the transport and positive-definite forms of the entropy production rate. A relationship between this difference and numerical errors in each control volume will be developed and discussed. The present study considers mixed convection in lid-driven and isothermal wall cavities. It is observed that the apparent entropy production difference is related to the numerical error. The normalized peak apparent entropy production difference shows a reasonable agreement with the normalized peak numerical error at corresponding nodes. Although the results are obtained for limited application problems, it is anticipated that similar trends exist for other flow conditions and geometrical configurations.

This section presents results for the apparent entropy production difference and numerical error analysis for mixed and natural convection of various fluids in a lid-driven cavity and isothermal wall enclosure. The analysis focuses on the determination of the apparent entropy production difference, numerical errors, and a potential relationship between these variables. The results also include grid refinement studies and their effects on the apparent

entropy production difference. The thermophysical properties of the fluids are presented in Table 5.1 [116].

Table 5-1: Thermophysical properties of fluids

Physical Property	Air	Water
Density, ρ (kg/m^3)	1.180	993
Thermal Conductivity, K (W/m K)	0.027	0.613
Thermal expansion coefficient, β (1/K)	0.031	2.1 x 10^{-6}
Specific Heat Capacity, C_p (J/kg K)	1004	4179
Dynamic Viscosity, μ (Pa.s)	1.9 x 10^{-5}	8.9 x 10^{-4}

The numerical model is applied to two test problems. The first example is a lid-driven cavity containing a working fluid with a Prandtl number of Pr = *5.23,* and lid Reynolds number, Re = *100,* as shown in Figure 5.1. The second problem is an isothermal wall enclosure containing a working fluid with a Prandtl number of Pr = *0.71*, and Rayleigh number of Ra = 10^4. The assumptions include: (i) a Newtonian fluid; (ii) incompressible, laminar flow; (iii) two-dimensional flow; (iv) density variation in the buoyancy force term that is approximated by the Boussinesq method; and (v) a fluid with constant thermophysical properties. Under these assumptions, the governing equations include the conservation of mass, Navier-Stokes, and energy equations as follows:

$$\frac{\partial u}{\partial x} + \frac{\partial v}{\partial y} = 0 \tag{5.1}$$

$$\rho\left[\frac{\partial u}{\partial t} + u\,\frac{\partial u}{\partial x} + v\,\frac{\partial u}{\partial y}\right] = -\frac{\partial p}{\partial x} + \mu\left(\frac{\partial^2 u}{\partial x^2} + \frac{\partial^2 u}{\partial y^2}\right) \tag{5.2}$$

$$\rho\left[\frac{\partial v}{\partial t}+u\ \frac{\partial v}{\partial x}+v\ \frac{\partial v}{\partial y}\right]=\rho\beta g(T-T_c)+\mu\left(\frac{\partial^2 v}{\partial x^2}+\frac{\partial^2 v}{\partial y^2}\right) \tag{5.3}$$

$$\rho C_p\left[\frac{\partial T}{\partial t}+u\ \frac{\partial T}{\partial x}+v\ \frac{\partial T}{\partial y}\right]=k\left(\frac{\partial^2 T}{\partial x^2}+\frac{\partial^2 T}{\partial y^2}\right) \tag{5.4}$$

Dimensionless velocities are defined for the test problems as follows:

$$U=\frac{u}{\sqrt{g\beta\Delta TH^3}} \tag{5.5}$$

$$V=\frac{v}{\sqrt{g\beta\Delta TH^3}} \tag{5.6}$$

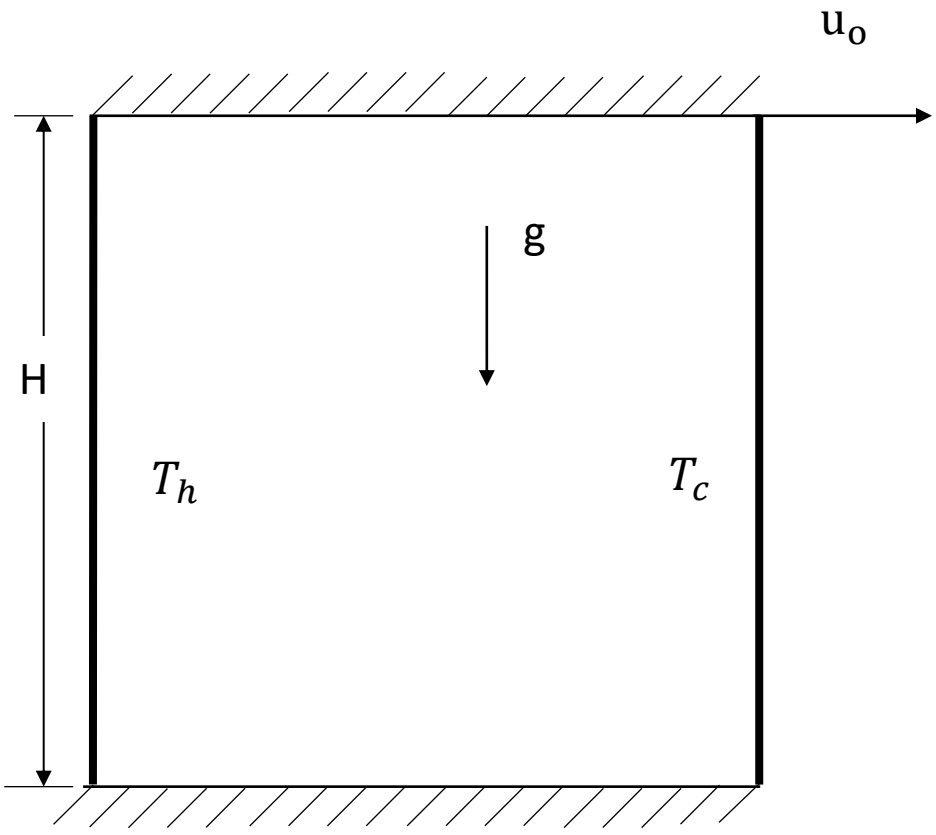

Figure 5-1: Schematic for Lid-Driven Cavity - Problem 1 (Pr = 5.23, Re = 100)

5.2 Problem 1: Lid-Driven Cavity Flow

The first test problem is mixed convection of water in a lid-driven cavity (Figure 5.1). The top and bottom walls of the cavity are insulated. The lid of the cavity is driven at a constant initial velocity, u_o. The vertical walls are isothermal. The right wall is kept at a constant low temperature, while the left wall is maintained at a constant high temperature. The boundary conditions for this problem are defined as follows:

$$\frac{\partial T}{\partial \boldsymbol{n}} = 0; \quad v = u = 0 \qquad for\ y = 0\ and\ 0 \le x \le L$$

$$\frac{\partial T}{\partial \boldsymbol{n}} = 0; \quad v = 0, u = u_o \qquad for\ y = H\ and\ 0 \le x \le L$$

$$T = T_h; \quad v = u = 0 \qquad for\ x = 0\ and\ 0 \le y \le H$$

$$T = T_c; \quad v = u = 0 \qquad for\ x = L\ and\ 0 \le y \le H \tag{5.7}$$

The horizontal component velocity, *u*, along the vertical axis is presented in Figure 5.2. The results are compared against past data presented by Ghia et al. [179]. The comparison shows good agreement. The results show the effects of the initial lid velocity on the fluid in the top region of the cavity. The horizontal component velocity of the fluid in the upper region of the enclosure is higher than other regions. The numerical error in the u-velocity is determined by the difference between the values of u-velocity from the numerical computations and past data of Ghia et al. (1982).

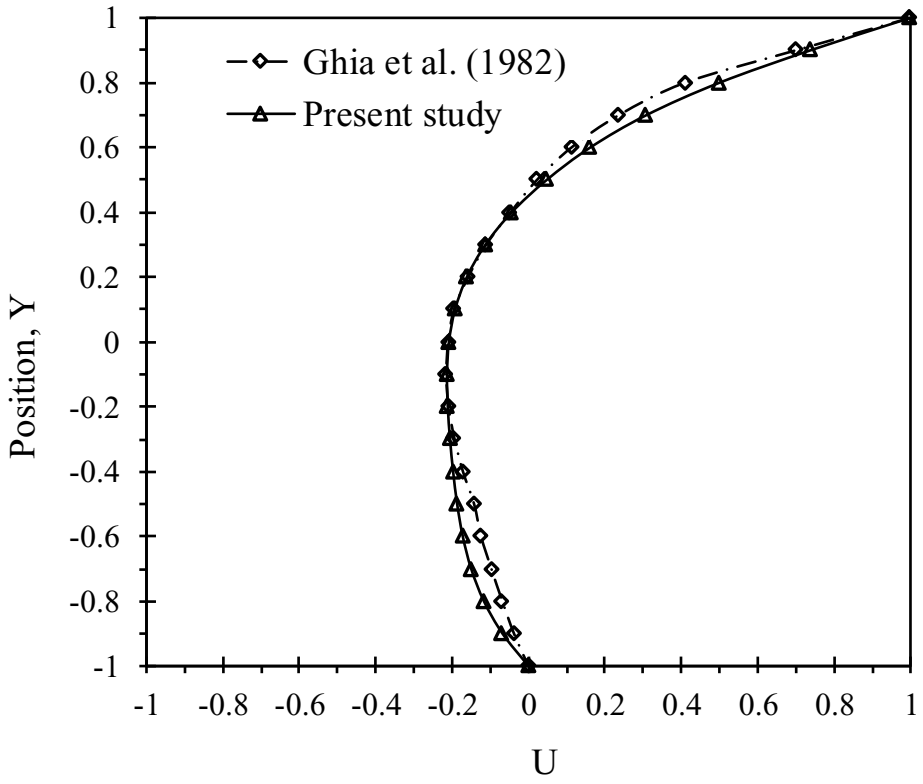

Figure 5-2: Comparison of dimensionless u-velocity with Ghia et al. (1982)

The data from Ghia et al. (1982) is based on a model validated with experimental work by Durst et al. (1974) in which a laser anemometer was used to determine the local values of the velocity. The work had indicated that with an uncertainty of less than 1 mm/s, velocities as low as 4mm/s within 0.15mm of walls can be measured using this technique. The velocity measurements were augmented with studies of flow visualization which were recorded on film.

Table 5-2 presents the first level u-velocity and how it was processed to obtain the dimensionless parameter which was compared with data from Ghia et al. [179]. The dimensionless values are obtained by dividing the product of the nodal velocity and height of the cavity by the thermal diffusivity.

Table 5-2: Dimensionless velocity calculation from first level results

U-Velocity (m/s)	Height of Cavity (m)	Thermal Diffusivity (m^2/s)	Dimensionless Parameter $\left(\frac{uH}{\propto}\right) * 10^{-2}$
0	0.01	$2.3x10^{-5}$	0
-0.020	0.01	$2.3x10^{-5}$	-0.087
-0.031	0.01	$2.3x10^{-5}$	-0.138
-0.036	0.01	$2.3x10^{-5}$	-0.159
-0.036	0.01	$2.3x10^{-5}$	-0.160
-0.033	0.01	$2.3x10^{-5}$	-0.146
-0.028	0.01	$2.3x10^{-5}$	-0.123
-0.022	0.01	$2.3x10^{-5}$	-0.095
-0.015	0.01	$2.3x10^{-5}$	-0.064
-0.0074	0.01	$2.3x10^{-5}$	-0.032
0	0.01	$2.3x10^{-5}$	0
0.007	0.01	$2.3x10^{-5}$	0.031
0.014	0.01	$2.3x10^{-5}$	0.063
0.021	0.01	$2.3x10^{-5}$	0.094
0.028	0.01	$2.3x10^{-5}$	0.123
0.033	0.01	$2.3x10^{-5}$	0.146
0.037	0.01	$2.3x10^{-5}$	0.160
0.036	0.01	$2.3x10^{-5}$	0.160
0.032	0.01	$2.3x10^{-5}$	0.138
0.020	0.01	$2.3x10^{-5}$	0.087
0	0.01	$2.3x10^{-5}$	0

Figure 5.3 shows the positive-definite and transport forms of entropy production along the vertical axis. Since the positive-definite entropy equation is given by a sum of squared terms, it is expected that the results are all positive values. It is also expected that the highest entropy production occurs in the upper region of the enclosure, due to friction irreversibilities caused by the high velocity of the moving lid of the cavity. The results of the transport form of entropy production have a similar trend as the positive-definite entropy production. However, entropy production values are not all positive due to numerical errors.

A negative entropy production is an indication of numerical error and a local violation of the second law [6]. However, the presence of numerical entropy destruction makes it challenging to evaluate the generalized entropy generation without quantifying the proportion of the actual (physical) entropy generation. Although a positive entropy generation may suggest numerical stability and a physically realistic solution, it does not quantify the possible entropy destruction in the CFD formulation.

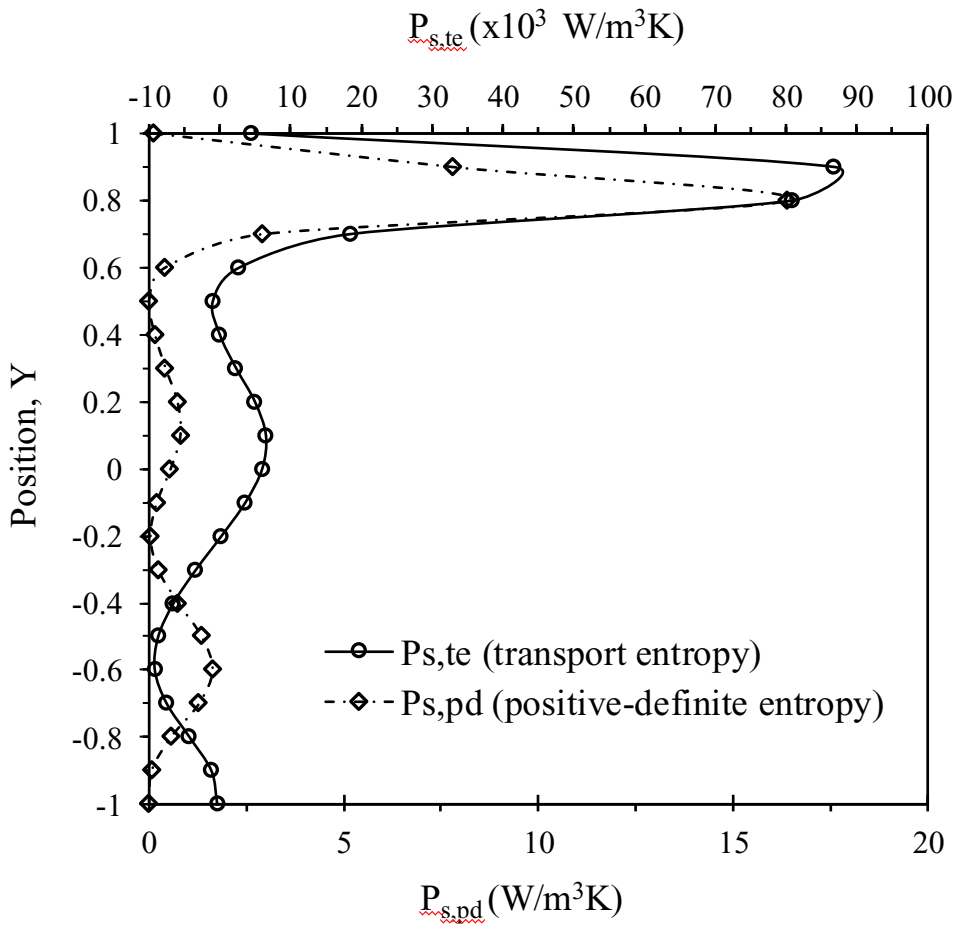

Figure 5-3: Transport and positive-definite entropy production along the height of the enclosure.

The numerical formulation of both the positive definite and transport forms of the entropy production equations involve numerical approximation which is prone to discretization error. Though the positive definite entropy computation produces non-negative entropy in the solution, there is still the possibility of numerical error in the solution due to discretization approximations. On the other hand, negative entropy generation may be obtained from the computation of the transport entropy.

By looking at the results from both entropy computations, it is difficult to determine which of the formulations possess less numerical errors or higher accuracy. However, the apparent entropy production difference, which is the difference between the positive definite and transport form of the entropy production equations is an important parameter for predicting the magnitude and trend of the numerical error in the solution because in an ideal situation with an exact solution, the difference between the transport form and positive-definite entropy equations should be equal to zero. Hence, the apparent entropy production difference is an important parameter for predicting the magnitude and trend of the numerical error in the solution. For numerical algorithm correction, this parameter is used in Chapter 6 to model an entropy-based artificial viscosity which is used to develop a corrective mechanism for the numerical algorithm.

Figure 5.4 shows a comparison between the error in u-velocity and apparent entropy production difference. Recall that the apparent entropy production difference is the change between the entropy production as computed and normalized by the transport and positive-definite forms of the entropy equation. The results in Figures 5.3 and 5.4 show a similar

trend, whereby a relationship appears to exist between the numerical error in u-velocity and the apparent entropy production difference.

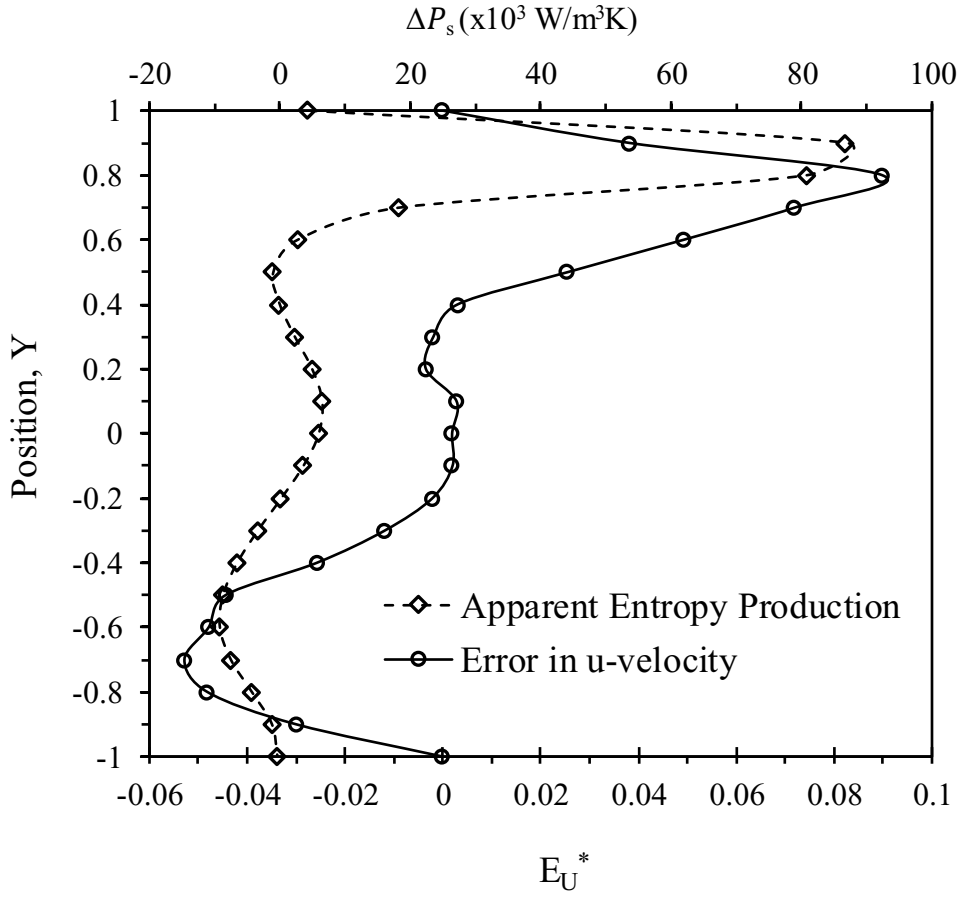

Figure 5-4: Apparent entropy production difference and numerical error in u-velocity along the height of the enclosure.

Figure 5.5 presents a comparison between the normalized numerical error in u-velocity and the normalized apparent entropy production difference. It is observed that the normalized peak error in u-velocity and the normalized peak apparent entropy production difference are nearly equal. This result suggests that the difference between computed entropy production rates can characterize the magnitude of solution errors. If the discretized entropy

transport equation yields negative rates of entropy production, this suggests non-physical erroneous results that scale approximately in relation to the magnitude of the solution error.

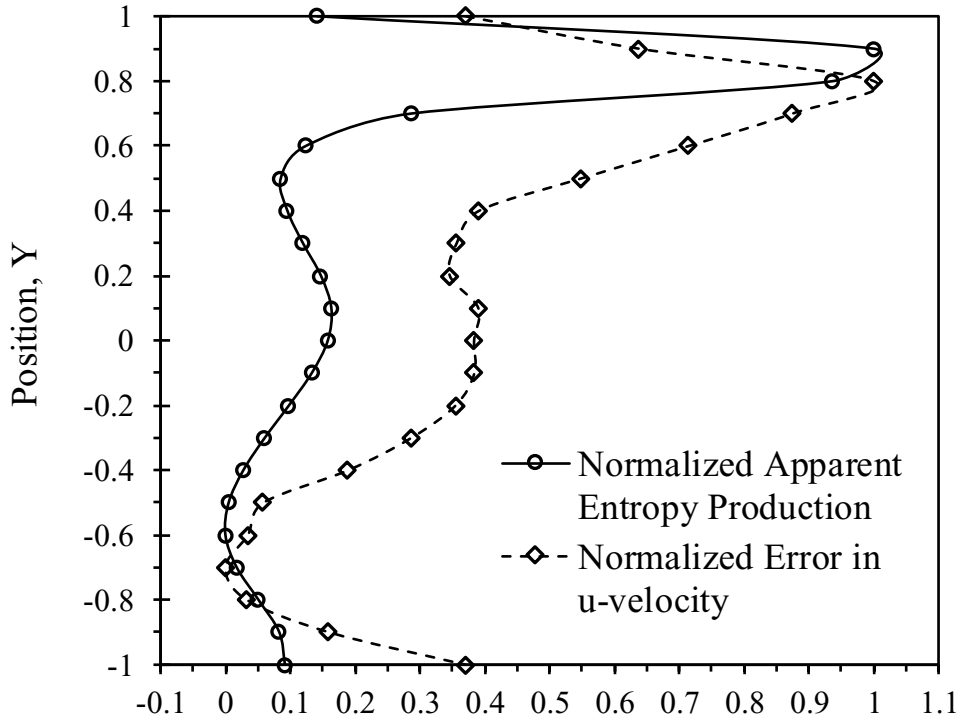

Figure 5-5: Normalized apparent entropy production difference and numerical error in u-velocity along the height of the enclosure.

The apparent entropy production difference is normalized by using Equation (5.10). The dimensionless temperature is normalized using Equation (5.9). Other variables such as velocity and error are normalized using Equation (5.11).

Table 5-3 shows the first level results of apparent entropy production difference. The apparent entropy production difference is the difference between the positive definite and transport forms of entropy production.

Table 5-3: Normalized apparent entropy production from first level results

Apparent Entropy Production Difference (W/m^3K)	Minimum Apparent Entropy Production Difference (W/m^3K)	Maximum Apparent Entropy Production Difference (W/m^3K)	Normalized Apparent Entropy Production Difference
4414.97	-9198.66	86856.60	0.142
86856.60	-9198.66	86856.60	1
80831.43	-9198.66	86856.60	0.937
18417.28	-9198.66	86856.60	0.288
2730.60	-9198.66	86856.60	0.124
-1000.39	-9198.66	86856.60	0.085
-10.25	-9198.66	86856.60	0.096
2291.32	-9198.66	86856.60	0.120
4949.57	-9198.66	86856.60	0.147
6500.34	-9198.66	86856.60	0.163
5972.60	-9198.66	86856.60	0.158
3607.00	-9198.66	86856.60	0.133
223.29	-9198.66	86856.60	0.098
-3361.57	-9198.66	86856.60	0.061
-6539.80	-9198.66	86856.60	0.028
-8717.25	-9198.66	86856.60	0.005
-9198.66	-9198.66	86856.60	0
-7517.33	-9198.66	86856.60	0.018
-4294.59	-9198.66	86856.60	0.051
-1209.48	-9198.66	86856.60	0.083
-373.03	-9198.66	86856.60	0.092

The results of the apparent entropy production difference are normalized to have a value between 0 and 1 by calculating the ratio of the difference between the apparent entropy production difference at a nodal point and the minimum value of apparent entropy production difference in the distribution ($\Delta \dot{P}_s - \Delta \dot{P}_{s,min}$) to the difference between the

maximum value of apparent entropy production difference in the distribution and the minimum value of apparent entropy production difference in the distribution ($\Delta\dot{P}_{s,max} - \Delta\dot{P}_{s,min}$). Equation (5.10) was used to obtain the normalized apparent entropy production difference. The normalized apparent entropy production difference is dimensionless.

Table 5-4 shows how the normalized error in u-velocity is processed. The error in u-velocity is obtained as the difference between the present results and past published data.

Table 5-4: Normalized error calculation from first level results

Error in U-Velocity	Minimum Error in U-Velocity	Maximum Error in U-Velocity	Normalized Error in U-Velocity
0	-0.053	0.090	0.370
0.038	-0.053	0.090	0.638
0.090	-0.053	0.090	1
0.072	-0.053	0.090	0.875
0.049	-0.053	0.090	0.715
0.026	-0.053	0.090	0.549
0.003	-0.053	0.090	0.391
-0.002	-0.053	0.090	0.357
-0.003	-0.053	0.090	0.346
0.003	-0.053	0.090	0.390
0.002	-0.053	0.090	0.384
0.002	-0.053	0.090	0.384
-0.002	-0.053	0.090	0.355
-0.012	-0.053	0.090	0.287
-0.026	-0.053	0.090	0.190
-0.044	-0.053	0.090	0.059
-0.048	-0.053	0.090	0.035
-0.053	-0.053	0.090	0
-0.048	-0.053	0.090	0.033
-0.030	-0.053	0.090	0.160
0	-0.053	0.090	0.370

The error in u-velocity is then normalized by dividing the difference between the error in u-velocity at a nodal point and the minimum value of the error in u-velocity by the difference between the maximum value of the error in u-velocity and the minimum value of the error in u-velocity. The normalized error in u-velocity is a dimensionless parameter.

5.3 Problem 2: Free Convection in a Cavity

The second test problem is natural convection of air in an isothermal wall cavity. The problem configuration is presented in Figure 5.6. The upper and bottom walls of the cavity are assumed adiabatic. The vertical walls are maintained at isothermal conditions. The left wall is maintained at a constant high temperature, while the right wall is kept at a constant low temperature. In this case, the numerical errors in temperature and u-velocity are considered. The boundary conditions for the isothermal wall cavity test problem are defined as follows:

$$\frac{\partial T}{\partial \vec{n}} = 0; \quad v = u = 0 \quad for\ y = 0, H\ and\ 0 \le x \le L$$

$$T = T_h; \quad v = u = 0 \quad for\ x = 0\ and\ 0 \le y \le H$$

$$T = T_c; \quad v = u = 0 \quad for\ x = L\ and\ 0 \le y \le H \tag{5.8}$$

The dimensionless temperature is evaluated as follows:

$$\theta = \frac{T - T_c}{T_h - T_c} \tag{5.9}$$

The normalized apparent entropy production difference is calculated as follows:

$$\Delta \dot{P}_{s,n} = \frac{\Delta \dot{P}_s - \Delta \dot{P}_{s,min}}{\Delta \dot{P}_{s,max} - \Delta \dot{P}_{s,min}} \tag{5.10}$$

The variable, ϕ (such as velocity or temperature) is normalized by the equation given below:

$$\phi_n = \frac{\phi - \phi_{min}}{\phi_{max} - \phi_{min}} \tag{5.11}$$

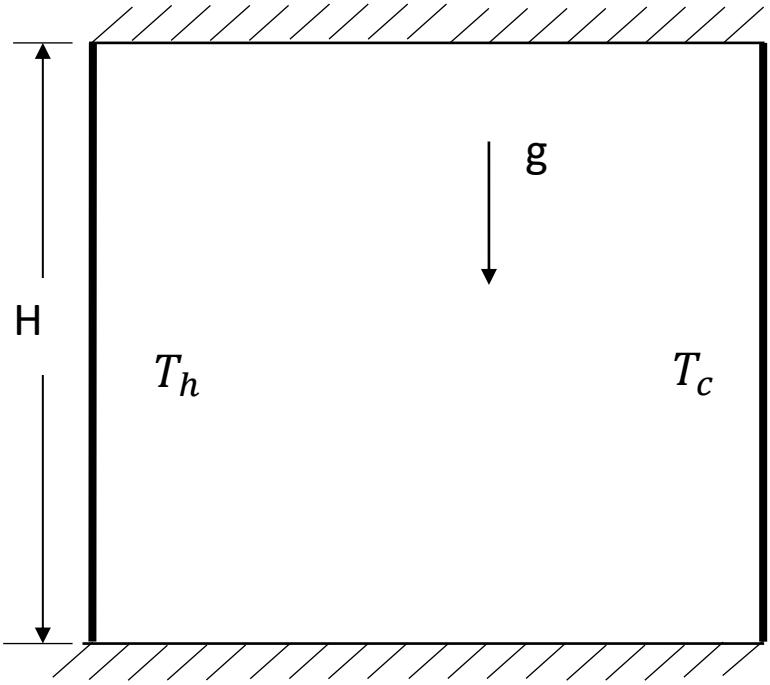

*Figure 5-6: Configuration for Natural Convection - Problem 2 (*Ra=10^4, Pr =*0.71).*

Figure 5.7 (a) shows a comparison of temperature distributions with past data presented by Khanafer et al. [94]. Figure 5.7 (b) presents a comparison of u-velocity with past results of Engelman [181]. Figure 5.8 shows the numerical error in temperature and u-velocity as computed by values obtained from numerical computations and past data. The dimensionless temperature, Θ is evaluated using Equation (5.9).

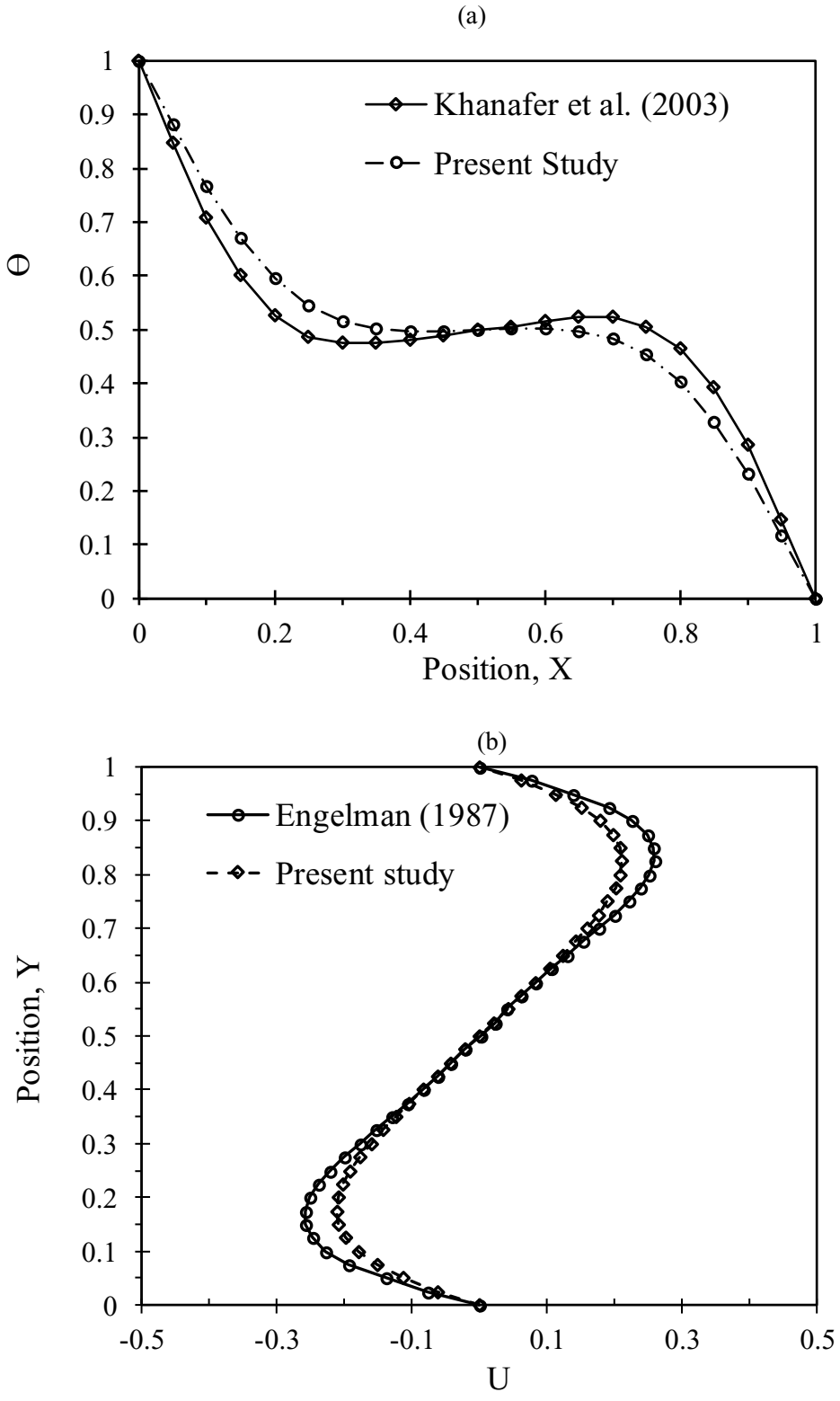

Figure 5-7: (a) Temperature and (b) u-velocity in the cavity

The result from this model is validated with published numerical benchmark data that are widely referenced and generally accepted by researchers in the field of thermofluids. The results presented in Figures 5.2, 5.7(a), and 5.7(b) are comparisons with numerical work of Ghia et al. (1982), Khanafer et al. (2003), and Engelman (1987), respectively, which was originally validated with experimental work of Durst et al. (1974) and Krane and Jesse (1983).

Table 5-5: Dimensionless temperature calculation from first level results

Temperature (K)	Minimum Temperature (K)	Maximum Temperature (K)	Dimensionless Temperature
312.00	300	312	1
310.58	300	312	0.881
309.21	300	312	0.768
308.04	300	312	0.670
307.14	300	312	0.595
306.54	300	312	0.545
306.19	300	312	0.516
306.02	300	312	0.501
305.96	300	312	0.496
305.96	300	312	0.497
305.99	300	312	0.499
306.02	300	312	0.502
306.03	300	312	0.502
305.97	300	312	0.497
305.79	300	312	0.483
305.45	300	312	0.454
304.85	300	312	0.404
303.96	300	312	0.330
302.78	300	312	0.232
301.42	300	312	0.118
300.00	300	312	0

Hence, the benchmark solutions which were used to calculate the errors are considered to be exact solutions. The uncertainty of experimental work was obtained by measurement

deviation of the parameters. The measuring error of T_h is ± 0.001 °C, the measuring error of T_c is ± 0.001 °C, and the measuring errors of the width and the length are ± 0.5 mm.

Table 5-5 presents the first level results of the temperature distribution. The dimensionless temperature is processed to lie between 0 and 1 by calculating the ratio of the difference between the temperature at a nodal point and the minimum value of temperature in the distribution ($T - T_{min}$) to the difference between the maximum value of temperature in the distribution and the minimum value of temperature in the distribution ($T_{max} - T_{min}$). Equation (5.9) was used to obtain the dimensionless temperature.

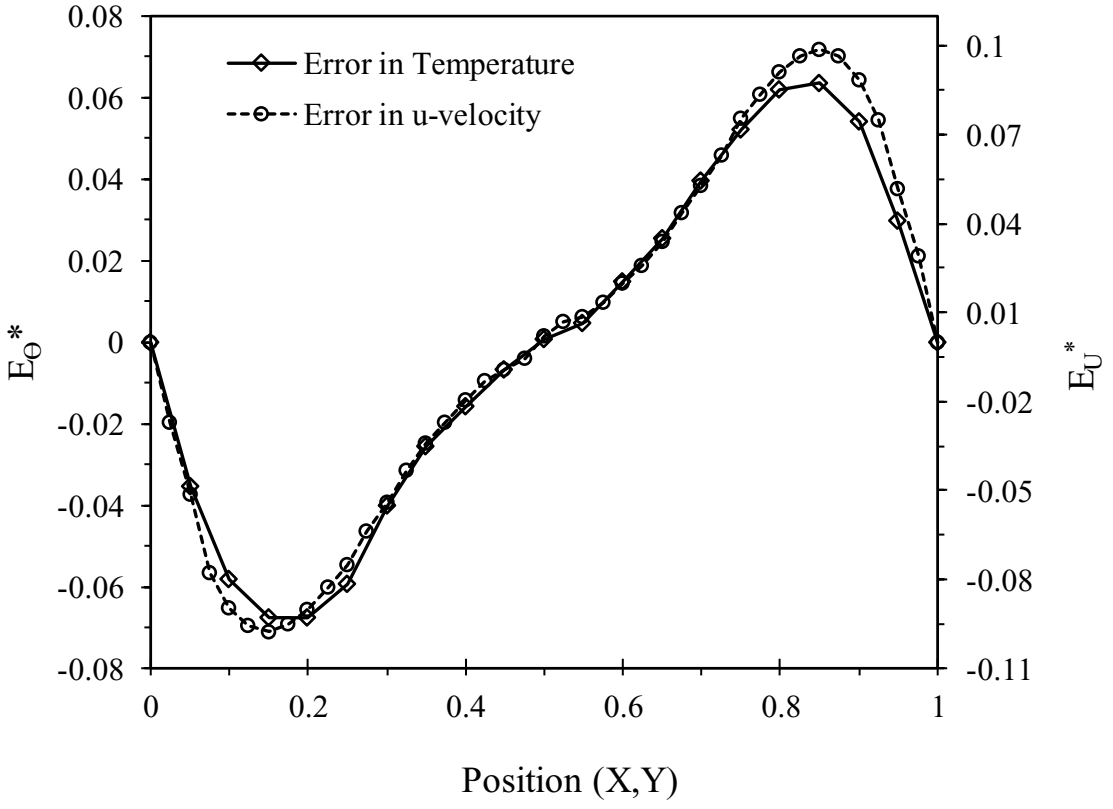

Figure 5-8: Numerical error in temperature (x-direction) and u-velocity (y-direction) along the length and height of the enclosure, respectively.

The apparent entropy production difference and numerical error in the temperature distribution along the cavity length are compared in Figure 5.9 (a). Figure 5.9 (b) compares the apparent entropy difference with the error in u-velocity along the cavity height. Again, the results show a similar trend between the numerical error and the apparent entropy production difference (in both cases of temperature and u-velocity distribution). This further suggests a relationship between these variables. Errors in numerical solutions are normally due to numerical approximations, artificial dissipation, and discretization methods, hence, the discrepancy between the results of this study and the benchmark solutions is due to numerical discretization approximations. The numerical error in the variable (velocity and temperature) is determined by the difference between the values of the variables from the numerical computations and past benchmark solutions. The variable ϕ (such as velocity or error) is then normalized by Equation (5.11).

A new hypothesis is proposed in this thesis that the solution error is directly related to the normalized apparent entropy production difference as illustrated by the different case studies presented in this Chapter. The correlation hypothesis presented in Equation (3.71) suggests that the numerical solution error in the scalar variable E_ϕ is equal to the normalized apparent entropy production difference $\Delta \dot{P}_{s,n}$.

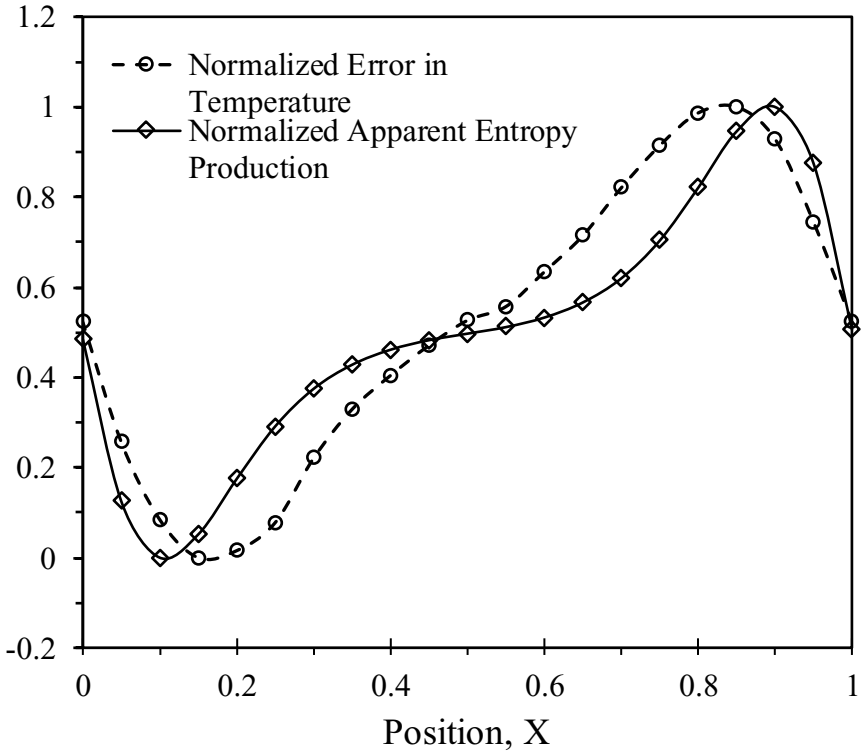

(a)

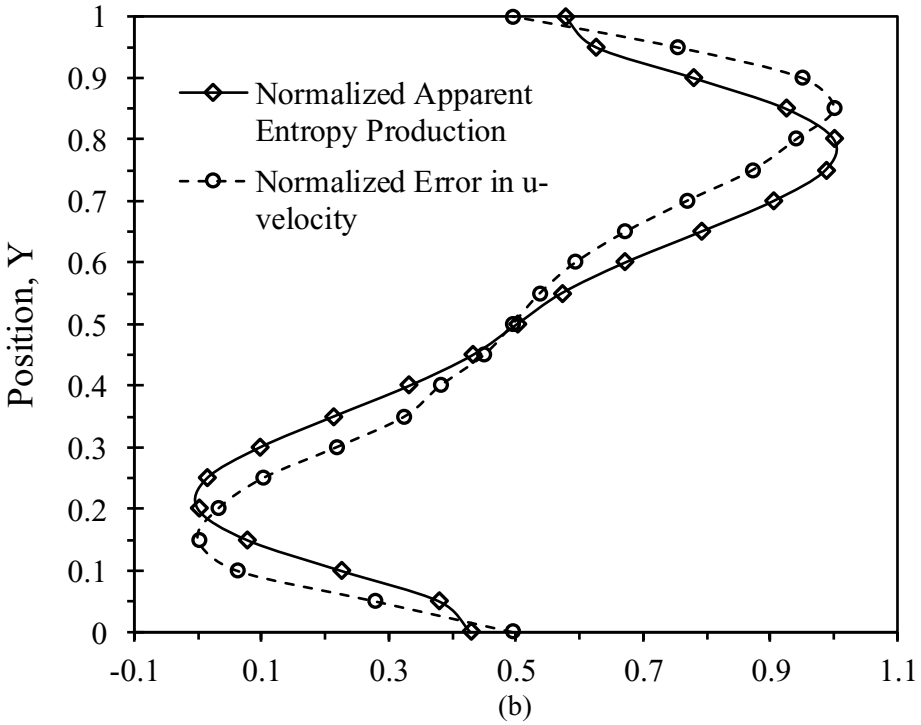

(b)

Figure 5-9: Comparison of normalized entropy production difference and solution error in (a) temperature and (b) u-velocity.

Figure 5.10 (a) shows a comparison between the normalized error in temperature and the normalized apparent entropy production difference. The normalized peak error in temperature and the normalized peak apparent entropy production difference are nearly equal. Also, results of the normalized error in u-velocity and normalized apparent entropy production difference along the height of the enclosure are compared in Figure 5.10 (b). Again, the normalized peak error in the u-velocity and the normalized peak apparent entropy production difference are nearly equal.

But additionally, the present results have provided a unique insight into the potential relationship between the apparent entropy production difference, solution error and convergence criteria. The results have indicated that the apparent entropy production difference approaches the solution error upon grid refinement in a manner that appears consistent with the rate of convergence of the numerical method. Additional studies on other flow problems and geometrical configurations are recommended to further explore this relationship between numerical entropy generation and error indicators in computational heat and fluid flow.

Based on these results, it is anticipated that the normalized peak solution error can be predicted using the normalized apparent entropy production difference. In the previous case studies, they were approximately equal, although this may have occurred due to the relatively simple nature of the test problems. Likely a correlation factor or higher order relationship among the two variables may be required for more complex flow configurations and geometries. Nevertheless, there appears to be a promising potential to

characterize solution errors with respect to entropy indicators without the prior availability of experimental data to confirm a numerical model's accuracy.

A grid refinement study was also performed for the velocity and temperature distributions to demonstrate independence of the results with respect to the grid spacing. Three successively refined grids were considered for the case of $\mathrm{Ra} = 10^4$ and $\mathrm{Pr} = 0.71$. The results in Figures 5.11 (a) and 5.11 (b) illustrate convergence and grid independence of the results with the 41 × 41 mesh. Finer grids yield an increasingly accurate and close relationship between the normalized apparent entropy production difference and solution error.

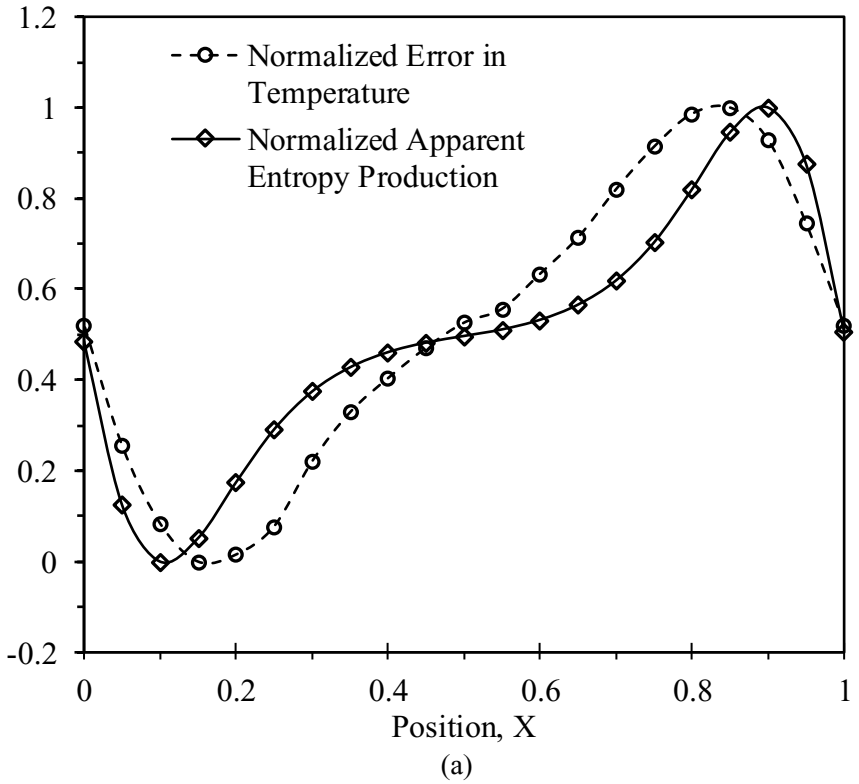

(a)

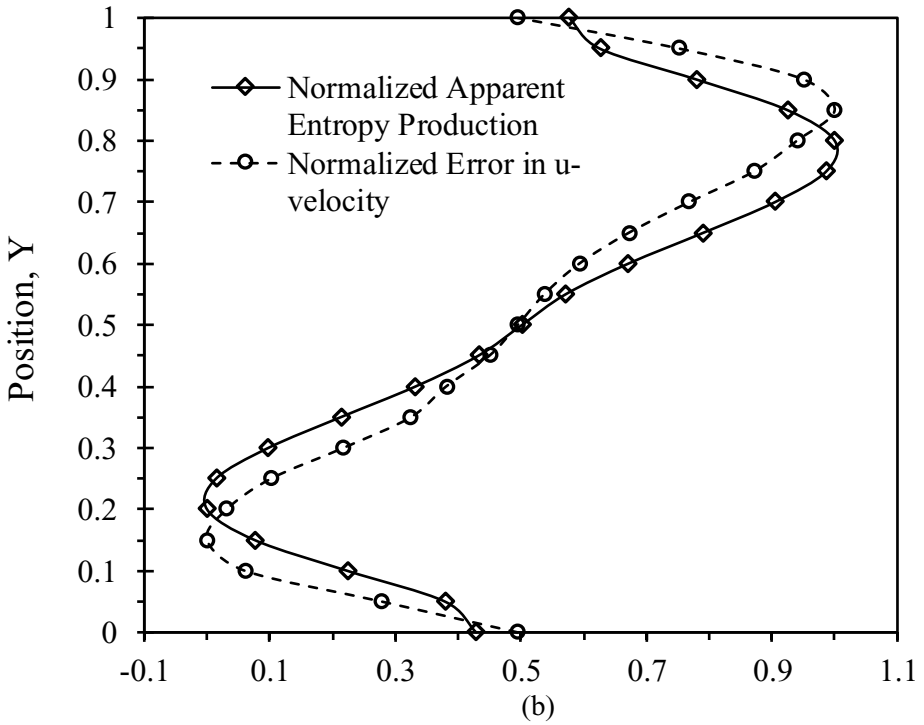

Figure 5-10: Comparison of normalized entropy production difference and solution error in (a) temperature and (b) u-velocity

Verification and validation of the numerical predictions were presented in earlier figures through comparisons with past data of Ghia et al. (1982) and Khanafer et al. (2003). The present results have provided a unique insight into the potential relationship between the apparent entropy production difference, solution error and convergence criteria. The results have indicated that the apparent entropy production difference approaches more closely to the solution error upon grid refinement in a manner that appears consistent with the rate of convergence of the numerical method. Additional studies on other flow problems and geometrical configurations would further explore this relationship between entropy generation due to numerical discretization and error indicators in computational heat and fluid flow.

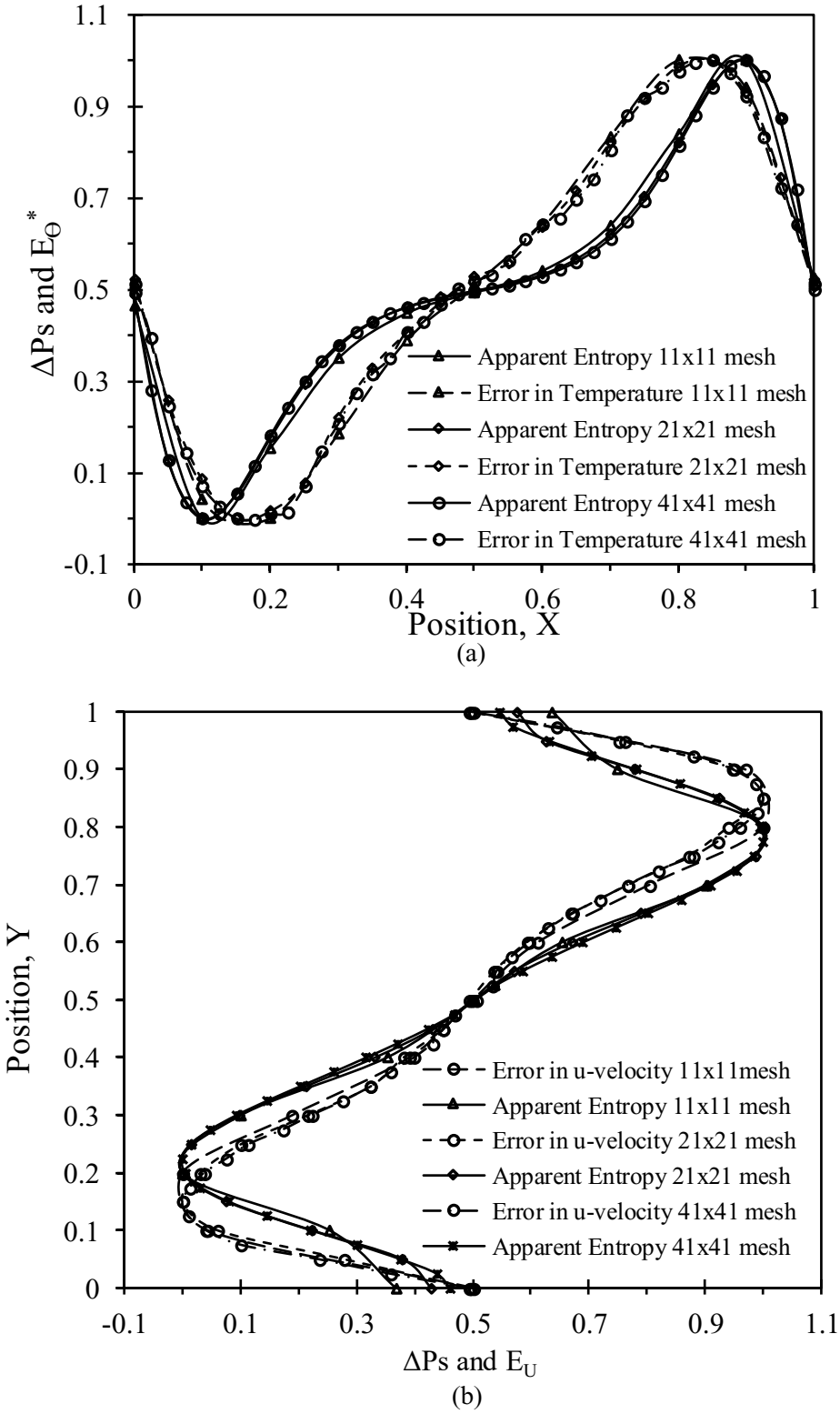

Figure 5-11: Grid refinement comparison of normalized entropy production difference and solution error in (a) temperature and (b) u-velocity

5.4 Conclusions

This chapter examined both physical and computational attributes of entropy production. A Second Law formulation based on different forms of the positive-definite and entropy transport equations was analyzed and presented in this chapter. To evaluate the numerical error, a new parameter called the "apparent entropy production difference" was defined based on the difference between the positive-definite and transport forms of the entropy production rate. A trend between this difference and numerical errors in each control volume was developed and discussed.

In addition, this chapter presented the analysis of entropy production of mixed convection in lid-driven and isothermal wall cavities filled with various fluids. It was found that the apparent entropy production difference is related to the numerical error. The results of the normalized peak apparent entropy production difference showed a reasonable agreement with the normalized peak numerical error at corresponding nodes. It is anticipated that similar trends exist for other geometrical configurations and flow conditions.

Furthermore, this chapter presented a new model of the apparent entropy production difference, numerical solution errors, and a new trend between these variables. The normalized peak values of apparent entropy production and numerical error were connected. The results from the lid-driven cavity problem suggested a relationship between the apparent entropy production difference and the numerical error of the u-velocity. Similar results for velocity and temperature were obtained for natural convection in a cavity. Grid refinement studies were performed, and their effects on the apparent entropy production difference were analyzed and reported in this chapter.

The next chapter will discuss the use of entropy-based artificial viscosity as a corrective mechanism to potentially stabilize the numerical results, reduce solution errors, and enhance numerical accuracy.

6 ENTROPY-BASED ARTIFICIAL VISCOSITY

6.1 Overview

In this chapter, the momentum equations will be modified by introducing an artificial viscosity as a coefficient of the diffusion terms to potentially stabilize the numerical results, reduce solution errors in the numerical results, and ultimately enhance the overall compliance of the results with the Second Law. This modification of the algorithm aims to ensure that the transport entropy production is minimally or non-negative.

As discussed earlier, the application of artificial viscosity to solve the conservation equations was pioneered by von Neumann and Richtmyer [128] in 1950. Over the past decades, artificial viscosity has evolved and been used in several numerical modelling applications to stabilize shock wave predictions and enhance the accuracy of numerical results and their efficiency. The concept of artificial viscosity has also been applied to numerical modelling in hydrodynamic, elastic, magneto, and plastic simulations [130, 131], as well as large eddy simulation of turbulent flow [134], staggered-grid Lagrangian hydrodynamics [135], discontinuous Galerkin methods [139], convection-diffusion-reaction modelling with nonlinear reaction mechanisms [140], nonlinear conservation laws [142], and the Euler equations [144].

The artificial viscosity method has been used by previous researchers, for example, to obtain shock wave prediction stabilization which leads to the improvement of numerical accuracy. The application of artificial viscosity is based on different methods. For example, past studies considered the following artificial viscosity based methods: residual-based

artificial viscosity; a posteriori error estimation; higher order, state-based artificial viscosity method; upwind symmetric interior penalty Galerkin (SIPG) method; spatio-temporal adaptive artificial viscosity method; and a Discontinuous Spectral Element Method (DSEM).

Based on a review of previous studies, and to the best of the author's knowledge, no past studies have considered the application of entropy-based artificial viscosity to improve numerical accuracy, particularly in natural and mixed convection heat transfer problems. Therefore, one of the novel contributions of this thesis is the development of a new corrective mechanism for numerical algorithms, using the transport entropy to calculate an artificial viscosity. This new algorithm corrective mechanism produces positive (or minimally negative) entropy generation and thereby enhances the accuracy of the numerical model.

This chapter focuses on the development of an entropy-based artificial viscosity as a corrective mechanism to improve numerical accuracy in natural convection heat transfer simulations.

6.2 Problem Configuration

A schematic diagram for natural convection in a square cavity is presented in Figure 6.1. The problem geometry is a square enclosure of height H, and width L, filled with a gas. The buoyancy induced flow is assumed to be two-dimensional flow of a Newtonian fluid. The thermophysical properties of the base fluid are assumed to be constant. The variation of density in the buoyancy force term is determined based on the Boussinesq

approximation. The upper and bottom walls of the cavity are assumed adiabatic. The vertical walls are maintained at isothermal conditions. The left wall is maintained at a constant high temperature, while the right wall is kept at a constant low temperature.

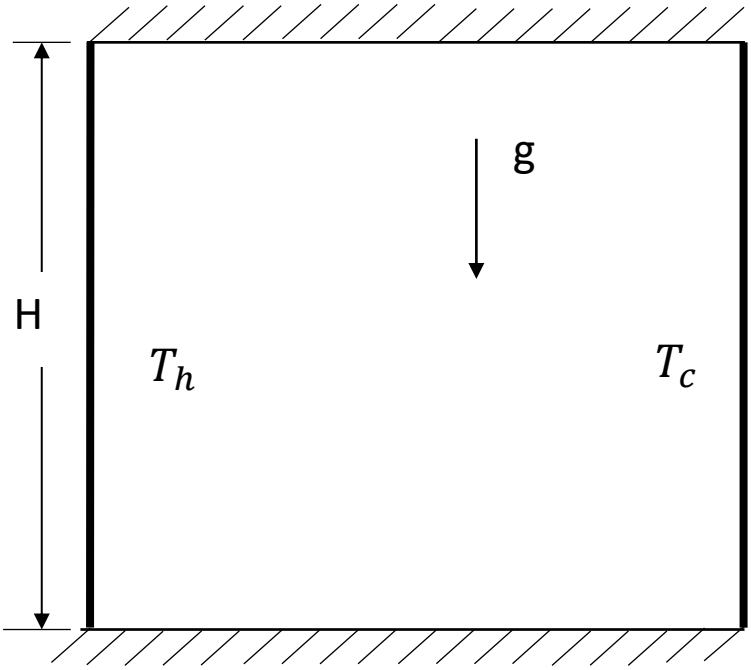

*Figure 6-1: Configuration for Natural Convection - Problem 2 (*Ra=10^4, Pr =*0.71)*

The boundary conditions for the test problem are defined as follows:

$$\frac{\partial T}{\partial \vec{n}} = 0; \quad v = u = 0 \quad for\ y = 0, H\ and\ 0 \le x \le L$$

$$T = T_h; \quad v = u = 0 \quad for\ x = 0\ and\ 0 \le y \le H$$

$$T = T_c; \quad v = u = 0 \quad for\ x = L\ and\ 0 \le y \le H$$

(6.1)

6.3 Results and Discussion

In this section, a varying number of timesteps will be used in the simulations, each of 1s duration, although results are steady-state so the timestep progression of the transient formulation serves like an iterative solver. Figure 6.2 presents the variation of total negative transport entropy production, total negative entropy-based artificial viscosity, and numerical error in velocity with grid spacing (11x11, 21x21, 41x41, and 81x81) along the midplane (y = 0.5), when the number of timesteps is set at 10. The top horizontal axis, *(1/ΔX),* represents the grid spacing.

The total entropy production is obtained as the summation of the products of the volumetric entropy productions and the areas of each control volume. The results indicate that the total negative transport entropy production and total negative entropy-based artificial viscosity decrease with finer grids. It is also observed that as the total negative transport entropy production and total negative entropy-based artificial viscosity decrease, the numerical error in v-velocity along the midplane also decreases. The numerical error in v-velocity is obtained by comparing the dimensionless v-velocity along the cavity midplane with past data of Khanafer et al. (2003).

Another interesting observation is that the entropy-based artificial viscosity yields less negative values compared to the transport entropy form for each subsequent grid spacing. The rate of entropy production with units of W/mK represent the total entropy production, which is obtained by the summation of the product of the volumetric entropy and the area of the control volume.

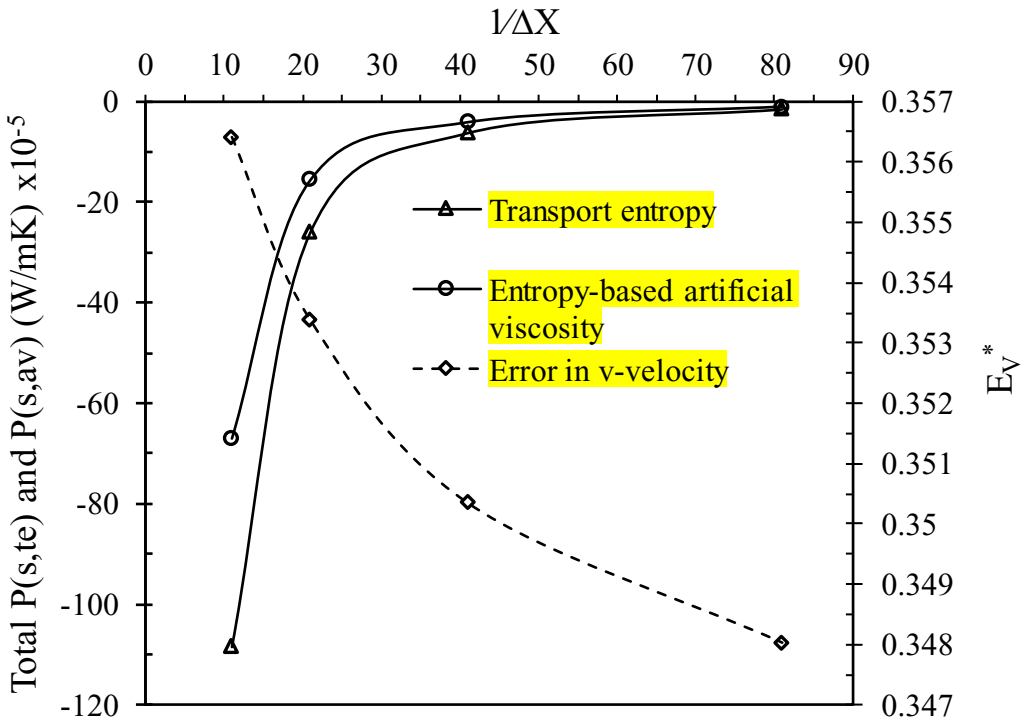

Figure 6-2: Variation of total negative transport entropy production, total negative entropy-based artificial viscosity, and numerical error in velocity with grid spacing along the midplane (y=0.5), for the number of timesteps of 10

The same procedure in Figure 6.2 is repeated for a different number of timesteps; in this case the number of timesteps is increased to 20. The results are presented in Figure 6.3, the total negative transport entropy production, the total negative entropy-based artificial viscosity, as well as the numerical error in v-velocity along the midplane decrease with finer grids. It is observed that as the number of timesteps is increased, the difference between the total negative transport entropy production and total negative entropy-based artificial viscosity increase. The entropy-based artificial viscosity produces lower negative entropy values for a timestep number of 20 when compared to entropy-based artificial viscosity with a timestep number of 10.

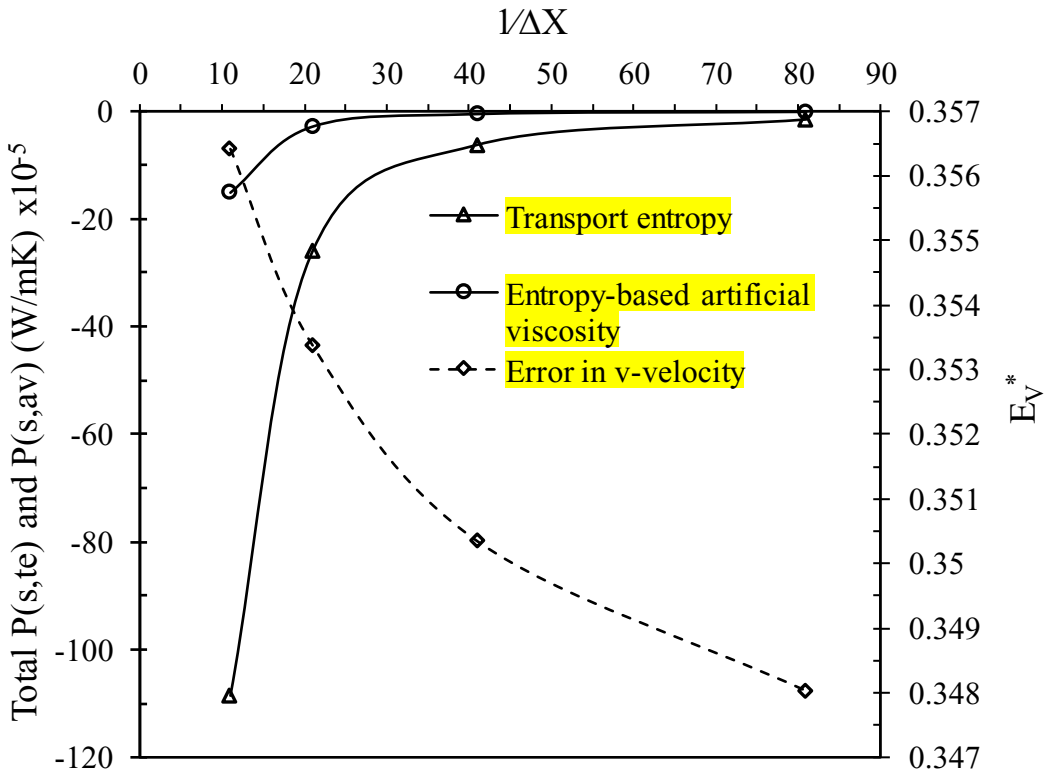

Figure 6-3: Variation of total negative transport entropy production, total negative entropy-based artificial viscosity, and numerical error in velocity with grid spacing along the midplane (y=0.5), for the number of timesteps of 20

The numerical computation is repeated once more for an increased number of timesteps of 30. The results presented in Figure 6.4 indicate that the total negative transport entropy production, total negative entropy-based artificial viscosity, and numerical error in v-velocity along the midplane decrease as the grid density is increased. It is observed that the difference between the total negative transport entropy production and the total negative entropy-based artificial viscosity increased with the increase in the number of timesteps. The entropy-based artificial viscosity produces less negative entropy production (nearly zero) values when the number of timesteps is set at 30, compared to entropy-based artificial

viscosity when the number of timesteps is set at 20 or 10. It is also observed that the entropy-based artificial viscosity results converged at the number of timesteps of 30, the entropy-based artificial viscosity at this number of timesteps is minimally negative (nearly zero). This suggests that the number of timesteps is a relevant factor in the application of the entropy-based artificial viscosity.

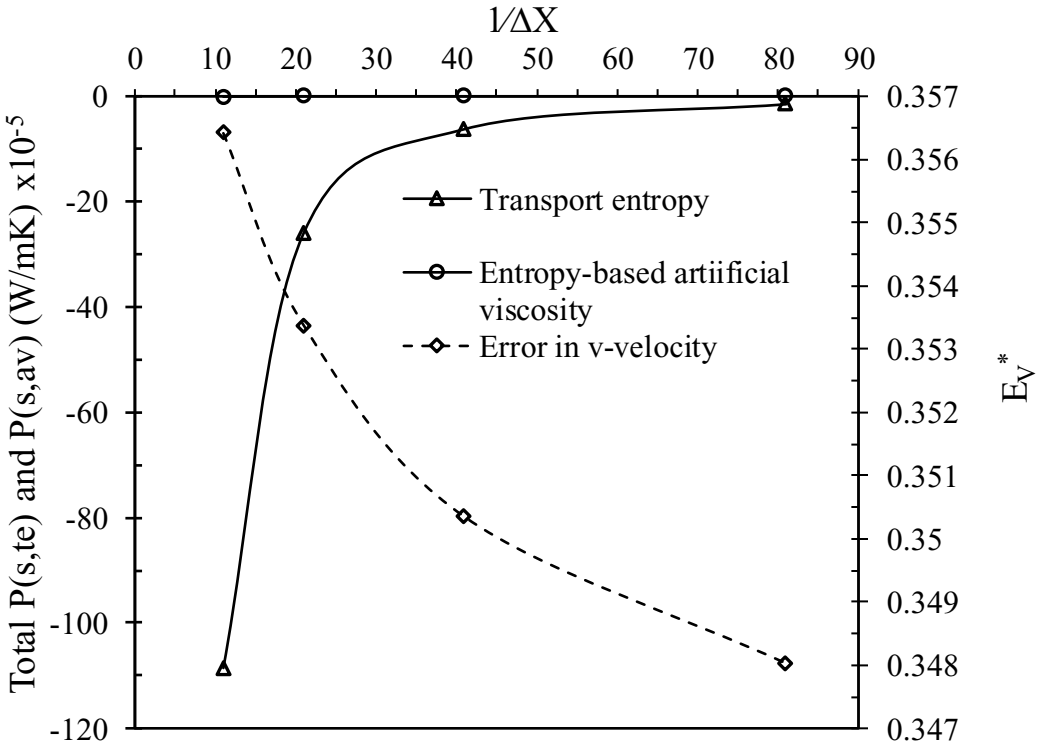

Figure 6-4: Variation of total negative transport entropy production, total negative entropy-based artificial viscosity, and numerical error in v-velocity with grid spacing along the midplane (y=0.5), for the number of timesteps of 30

Overall, the results in Figures 6.2 - 6.4 suggest that grid spacing and number of timesteps are important parameters in the application of entropy-based artificial viscosity as a corrective mechanism. The results indicate that the application of the entropy-based

artificial viscosity significantly minimizes the negative values in entropy production and reduces the error in the v-velocity results, thereby improving the overall accuracy of the numerical model.

A similar computational procedure is repeated in Figures 6.5 – 6.7.

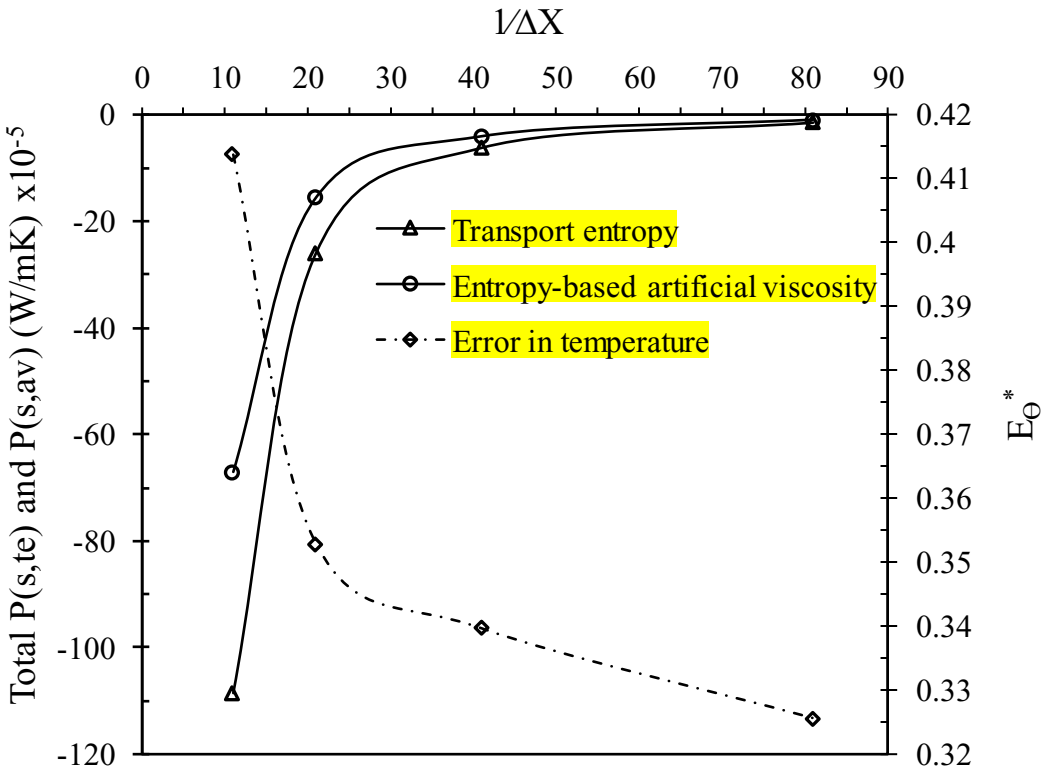

Figure 6-5: Variation of total negative transport entropy production, total negative entropy-based artificial viscosity, and numerical error in temperature with grid spacing along the horizontal midplane, for a number of timesteps of 10

This time, the variation of total negative transport entropy production, and total negative entropy-based artificial viscosity is compared with the variation in numerical error in temperature as the grid density is increased, for a number of timesteps of 10. Similarly, the results show that the total negative transport entropy production and the total negative entropy-based artificial viscosity decrease with an increase in grid density. Just like the

case of the numerical error in v-velocity, the numerical error in temperature along the midplane also decreases as the total negative transport entropy production and total negative entropy-based artificial viscosity decreased. The numerical error in temperature is determined by comparing the dimensionless temperature along the cavity midplane with past data of Khanafer et al. (2003).

Figure 6.6 presents the variation of the total negative transport entropy production, total negative entropy-based artificial viscosity, and numerical error in temperature with grid spacing along the horizontal midplane, when the number of timesteps is increased to 20. As in the previous case, the numerical error in temperature along the midplane decreases as the total negative transport entropy production and total negative entropy-based artificial viscosity decrease. And the entropy-based artificial viscosity tends to zero as the number of timesteps is increased.

In Figure 6.7, variation of the numerical error in temperature with grid spacing along the horizontal midplane is once again compared with the variation of the total negative transport entropy production and total negative entropy-based artificial viscosity, when the number of timesteps is set at 30. These results show that the total negative transport entropy production, total negative entropy-based artificial viscosity, and numerical error in temperature decrease as the grid density is increased.

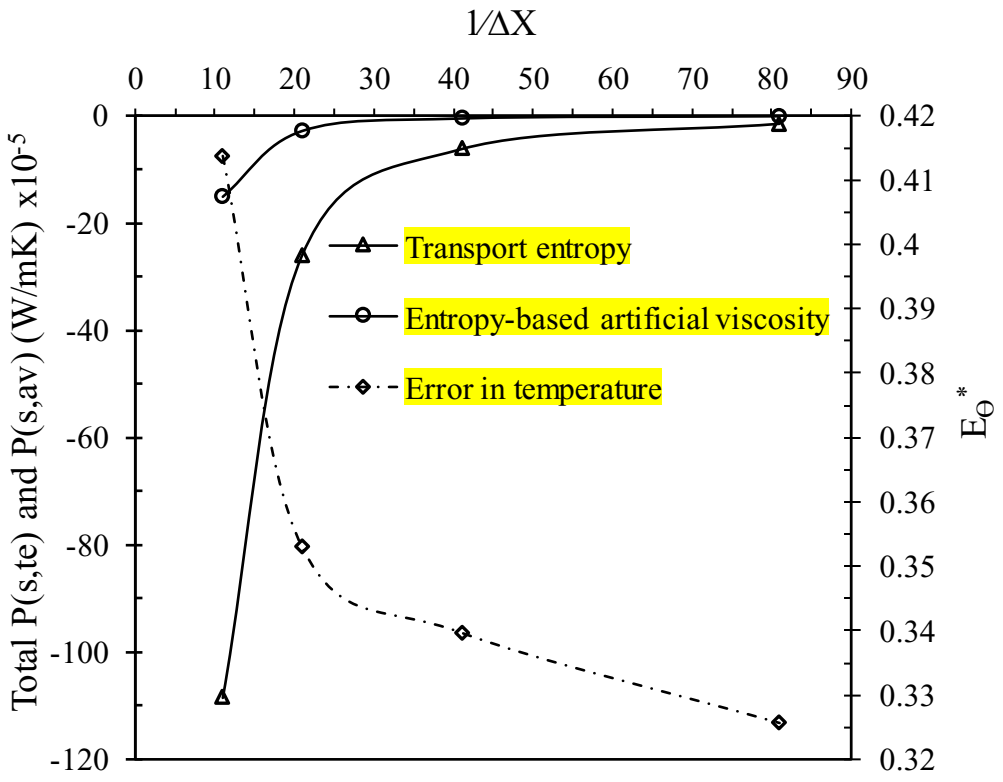

Figure 6-6: Variation of total negative transport entropy production, total negative entropy-based artificial viscosity, and numerical error in temperature with grid spacing along the horizontal midplane, for a number of timesteps of 20

In summary, the results in Figures 6.5 – 6.7 indicate that the application of the entropy-based artificial viscosity is also effective in reducing the numerical errors in temperature, just as in the case of numerical error v-velocity. The results show that the implementation of the entropy-based artificial viscosity can significantly minimize the negative values in entropy production, reduce the solution error in the numerical results, and thereby enhance the overall accuracy of the numerical model.

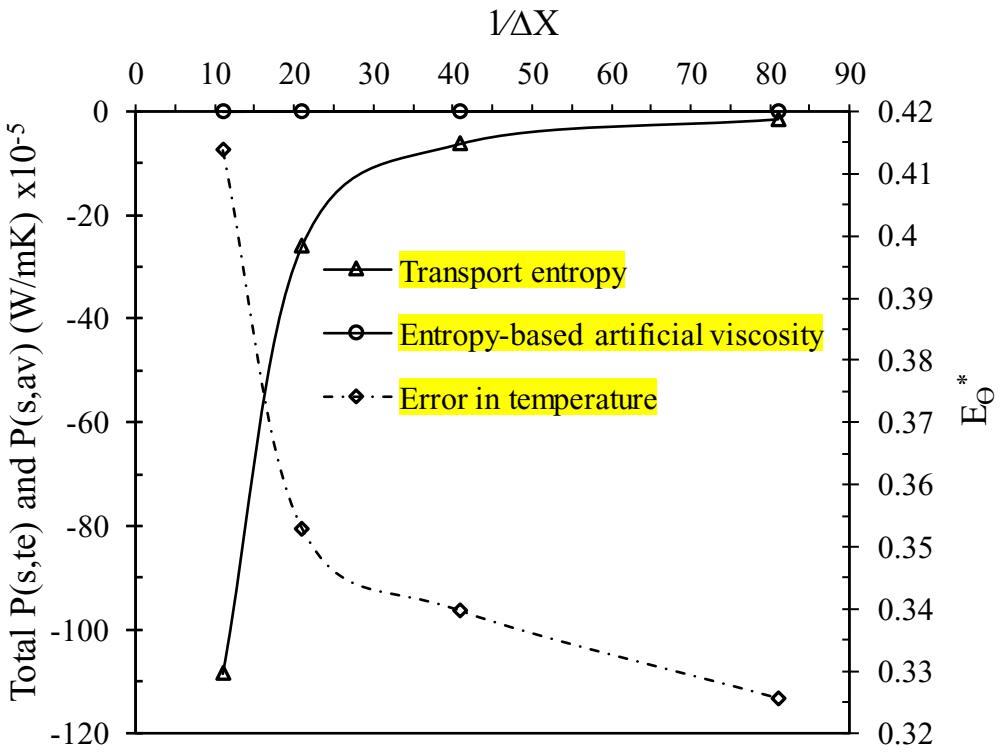

Figure 6-7: Variation of total negative transport entropy production, total negative entropy-based artificial viscosity, and numerical error in temperature with grid spacing along the horizontal midplane, for a number of timesteps of 30

A comparison between the transport entropy production, P(s,te), and entropy-based artificial viscosity, P(s,av), along the cavity horizontal midplane for a 21 x 21 mesh at different number of timesteps (10, 20, and 30) is presented in Figure 6.8. It is observed that as the number of timesteps increases, the entropy-based artificial viscosity stabilizes until it converges (at the number of timesteps of 30). As the entropy-based artificial viscosity stabilizes, the negative entropy production decreases until it becomes minimally negative. As illustrated in Figures 6.2 – 6.7, as the entropy-based artificial viscosity stabilizes, the numerical accuracy improves.

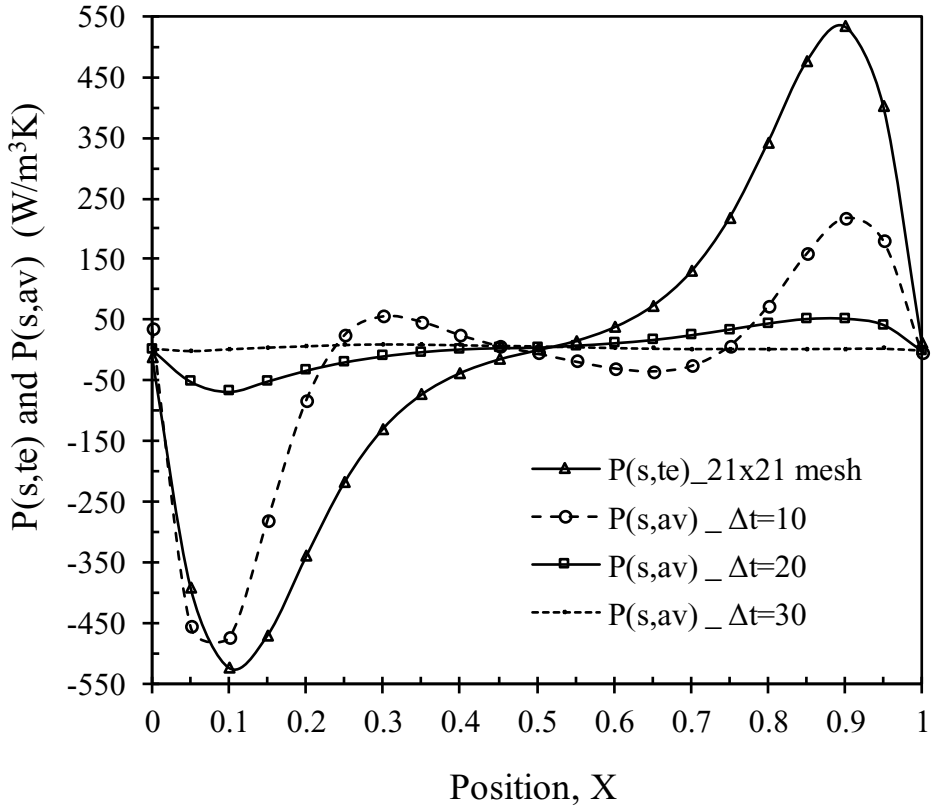

Figure 6-8: Comparison between transport entropy production, P(s,te), and entropy-based artificial viscosity, P(s,av), along the cavity horizontal midplane for a 21 x 21 mesh at different number of timesteps

The number of timesteps used to compute the transport entropy production, P(s,te), is 30. At convergence, the results of the transport entropy production, P(s,te) produce higher negative entropy production compared to the entropy-based artificial viscosity, P(s,av). This demonstrates the effectiveness of the entropy-based artificial viscosity, P(s,av) for stabilizing the artificial viscosity and minimizing the negative entropy production. The stabilized artificial viscosity is important for correcting the algorithm, yielding minimally negative entropy production, minimizing numerical errors, and improving the overall accuracy of the model.

In Figure 6.9, a 41 x 41 mesh was considered for the computation of the transport entropy production, P(s,te), and entropy-based artificial viscosity, P(s,av), along the cavity horizontal midplane for at different number of timesteps (10, 20, and 30). As in the case of the 21 x 21 mesh, the entropy-based artificial viscosity stabilizes with increase in number of timesteps until it reaches convergence. As the entropy-based artificial viscosity stabilizes, the negative entropy production decreases until it becomes minimally negative.

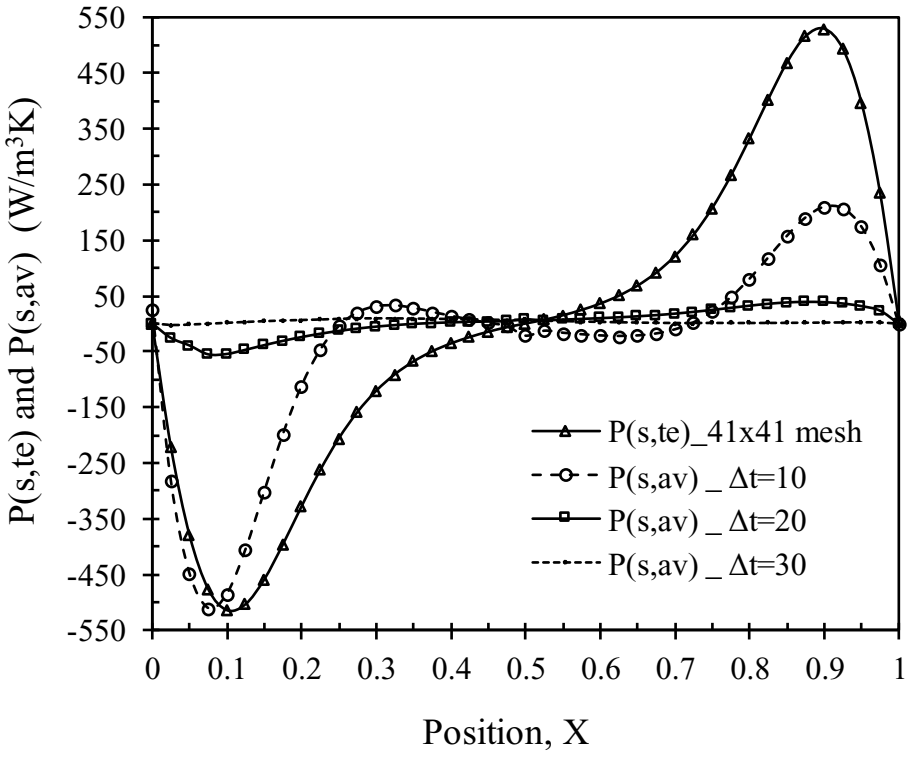

Figure 6-9: Comparison between transport entropy production, P(s,te) and entropy-based artificial viscosity, P(s,av) along the cavity horizontal midplane for 41 x 41 mesh at different timesteps sizes

Figure 6.10 presents the comparison of entropy-based artificial viscosity along the cavity midplane for different grid spacings (21x21, 41x41, and 81x81), when the number of

timesteps is set at 30. The stabilized entropy-based artificial viscosity at the number of timesteps of 30, is not zero as it appears in Figures 6.8 and 6.9. The results show that finer grids yielded less negative entropy production. For example, the entropy-based artificial viscosity for a 21x21 mesh yielded a negative entropy production of -2.3155 (W/m^3K). The entropy-based artificial viscosity for a 41x41 mesh yielded negative entropy production of -1.8872 (W/m^3K), while a negative entropy production of -1.6229 (W/m^3K) was obtained by the entropy-based artificial viscosity for the 81x81 mesh.

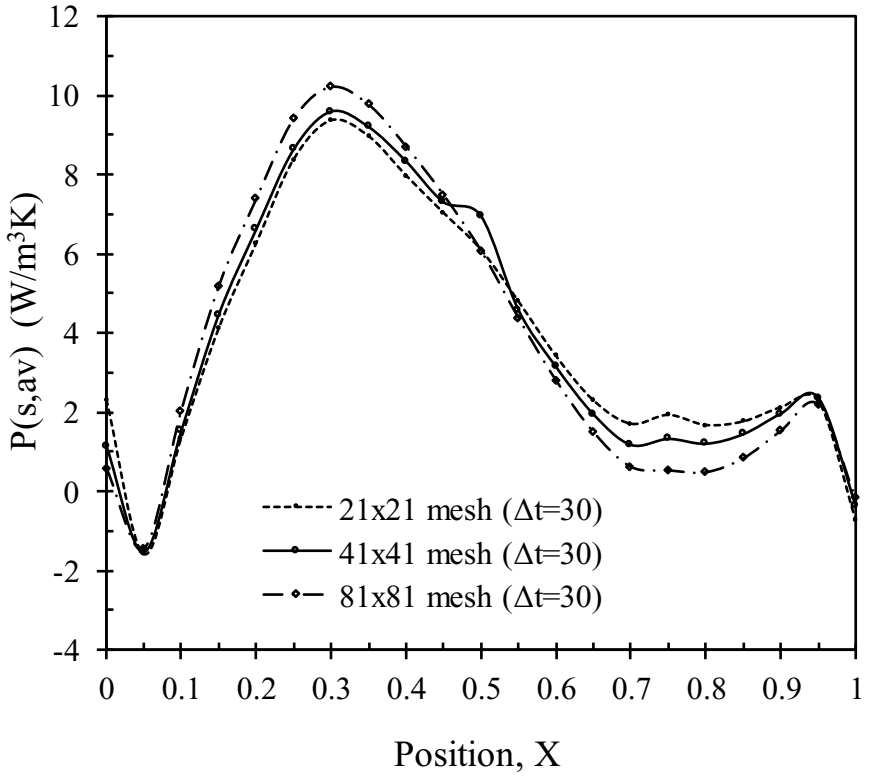

Figure 6-10: Comparison of entropy-based artificial viscosity along the cavity horizontal midplane for different grid spacings at the number of timesteps of 30

Figure 6.11 compares the total negative transport entropy production and total negative entropy-based artificial viscosity along the cavity midplane (y = 0.5) for different grid

spacings (41 x 41 and 81x81) as a function of number of timesteps (10, 20, and 30). The results illustrate that both the negative transport entropy production and negative entropy-based artificial viscosity vary as a function of the grid spacing and number of timesteps. As the grid density and number of timesteps increase, the negative entropy-based artificial viscosity and negative transport entropy decrease.

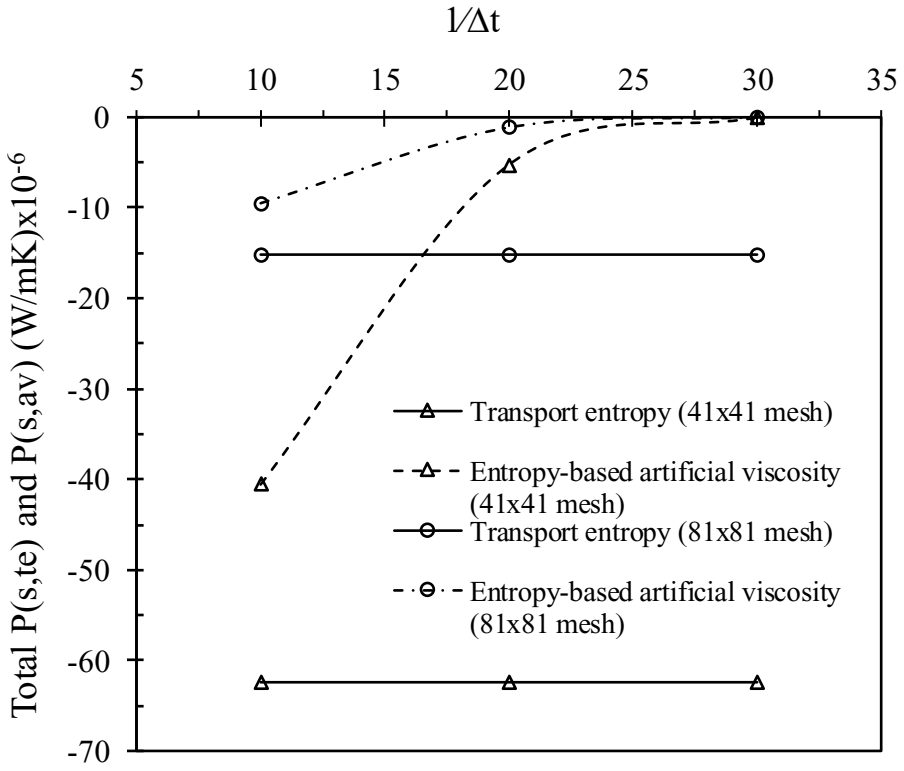

Figure 6-11: Comparison between total negative transport entropy and total negative entropy-based artificial viscosity along the cavity horizontal midplane for different grid spacings as a function of number of timesteps.

The plot also shows that the total negative entropy-based artificial viscosity converges at a value of -1.0×10^{-10} W/mK (minimally negative) when the number of timesteps is set at 30, with a grid spacing of 81x81. This result again suggests that the entropy-based artificial viscosity can be used as a corrective mechanism to significantly minimize the negative

entropy production, correct numerical errors in the algorithm, and improve the accuracy of the model.

The total negative transport entropy production, and total negative entropy-based artificial viscosity with the computation time for the results of 21x21 mesh is presented in Figure 6.12, while Figure 6.13 presents the total negative transport entropy production, and total negative entropy-based artificial viscosity with the computation time for the results of 41x41 mesh. Figures 6.11 - 6.13 illustrate that as the grid density and number of timesteps is increased, the negative entropy reduces, and the computation time of the results increases. For example, between Figures 6.12 and 6.13, a minimum total negative entropy-based artificial viscosity of -1.1 x 10^{-8} W/mK is obtained by a 41x41 mesh at computation time of 175.13 seconds.

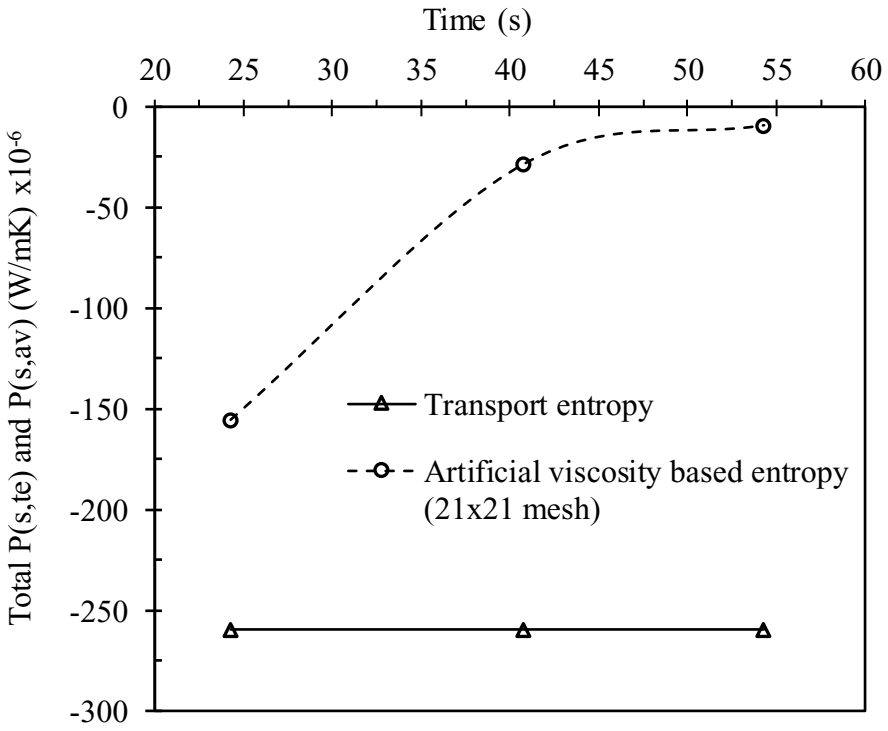

Figure 6-12: Total negative transport entropy production, and total negative entropy-based artificial viscosity with the computation time for the results for 21x21 mesh

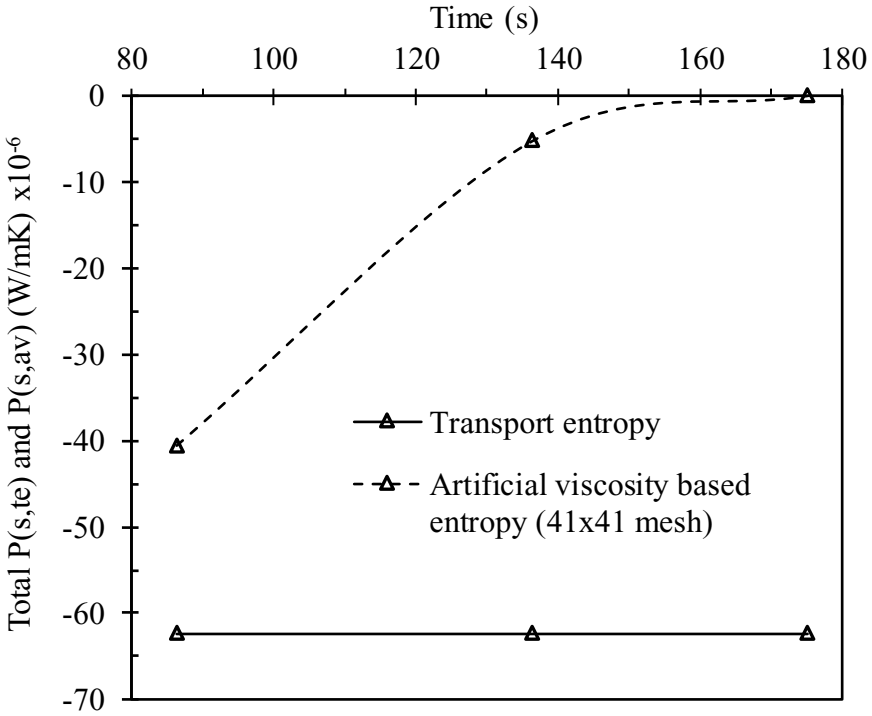

Figure 6-13: Total negative transport entropy production, and total negative entropy-based artificial viscosity with the computation time for 41x41 mesh

This imply that the application of the entropy-based artificial viscosity to improve the accuracy of the numerical model is at the expense of storage memory and computational time. Figure 6.14 compares the artificial viscosity for different number of timesteps (10, 20, 30, and 40) at a grid spacing of 21x21. Also, a grid spacing of 41x41 is considered in the comparison of the artificial viscosity for different number of timesteps (10, 20, 30, and 40) as presented in Figure 6.15, while a grid spacing of 81x81 is used in the comparison of the artificial viscosity for different number of timesteps (10, 20, 30, and 40) presented in Figure 6.16. The results from Figures 6.14 – 6.16 illustrates that the artificial viscosity stabilizes as the number of timesteps is increased for each grid spacing. The results also indicate that the artificial viscosity is approximately proportional to the entropy-based artificial viscosity.

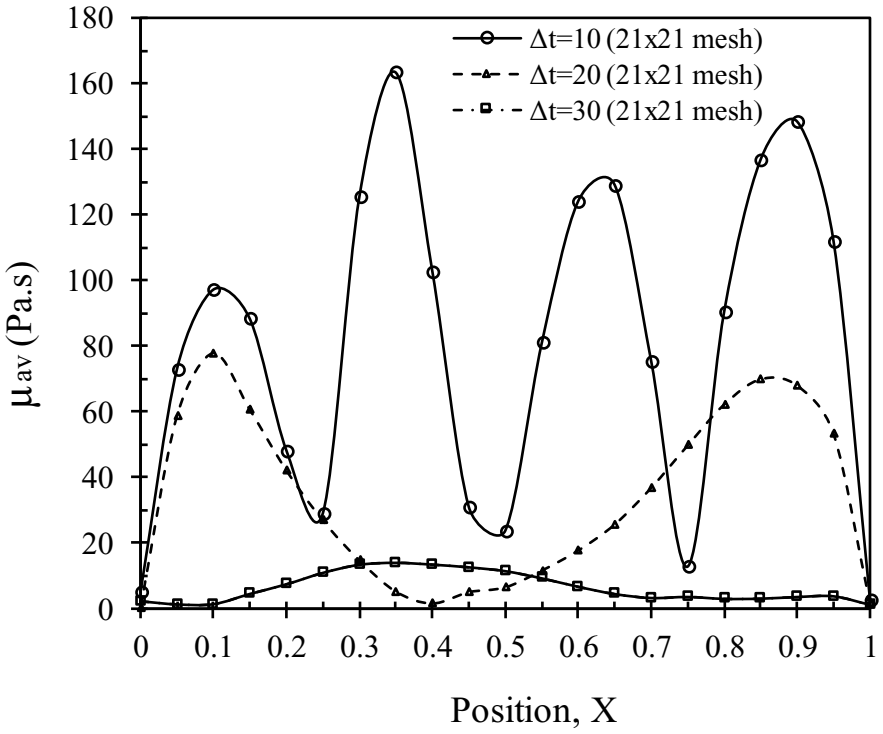

Figure 6-14: Comparison between the artificial viscosity for different number of timesteps at a grid spacing of 21x21

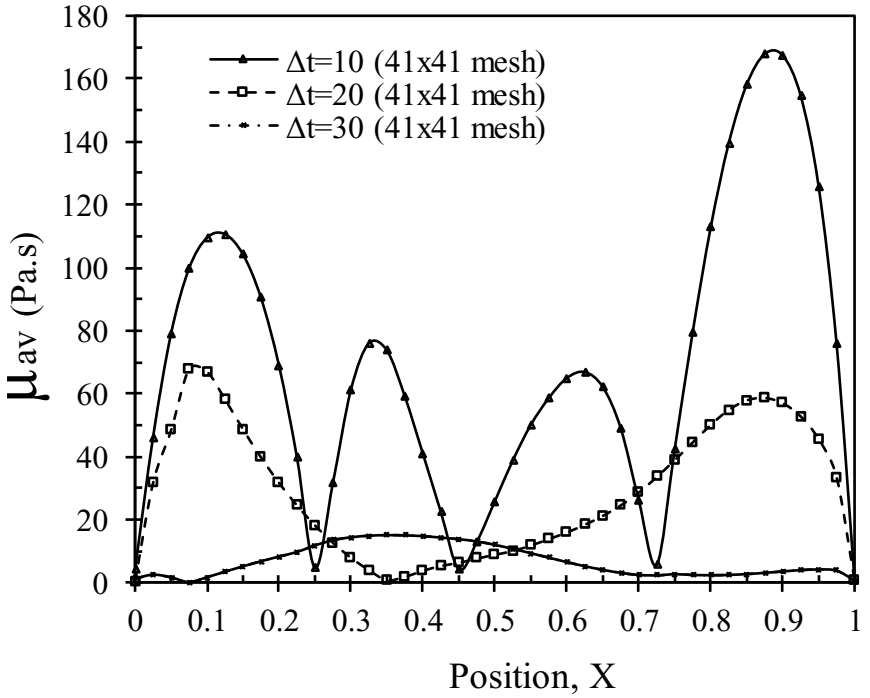

Figure 6-15: Comparison between the artificial viscosity for different number of timesteps at a grid spacing of 41x41

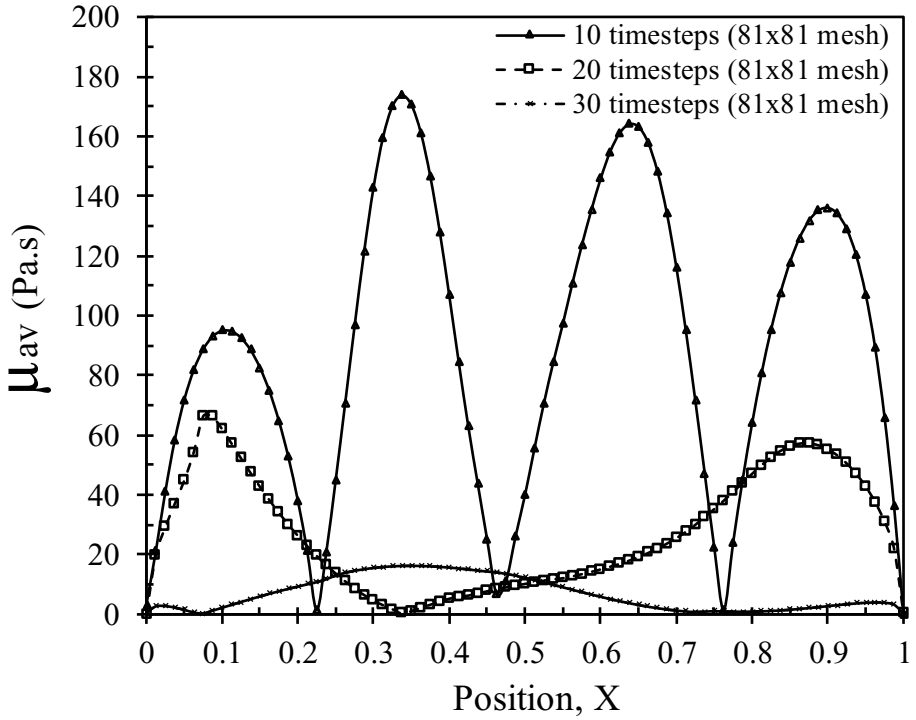

Figure 6-16: Comparison between the artificial viscosity for different number of timesteps at a grid spacing of 81x81

Figures 6.17 – 6.19 presents the artificial viscosity for each number of timesteps while the grid spacing is being varied. The artificial viscosity for different grid spacings (21x21, 41x41, and 81x81) for the number of timesteps of 10, is presented in Figure 6.17. Figure 6.18 shows the artificial viscosity for different grid spacings (21x21, 41x41, and 81x81) when the number of timesteps is increased to 20, while Figure 6.19 presents the artificial viscosity for different grid spacings (21x21, 41x41, and 81x81) with the number of timesteps increased to 30. By comparing Figures 6.17, 6.18, and 6.19, it can be observed that the magnitude of the artificial viscosity decreases with an increase in the number of timesteps.

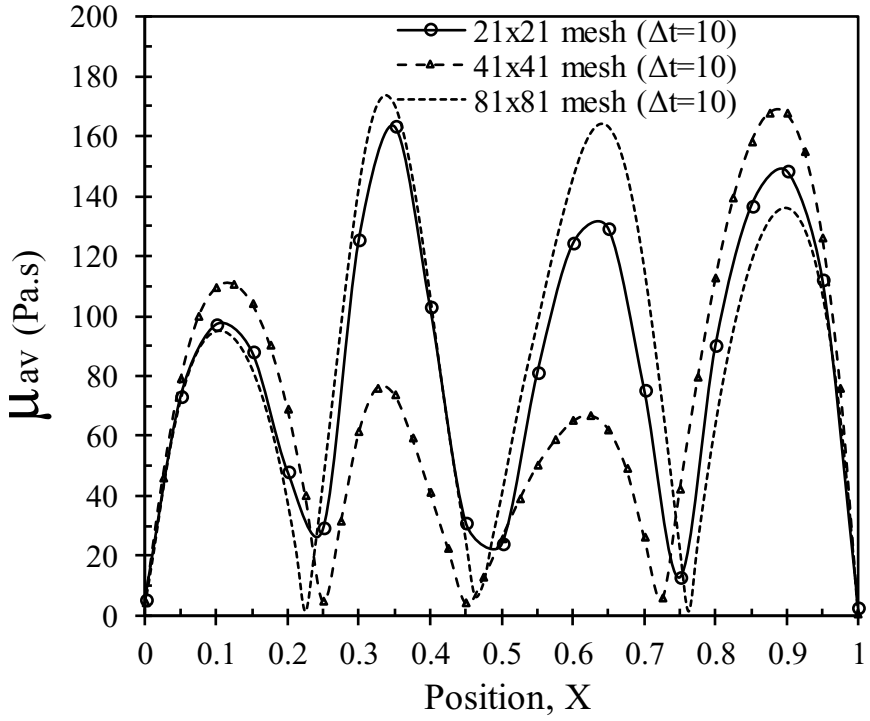

Figure 6-17: Artificial viscosity for different grid spacings and number of timesteps of 10

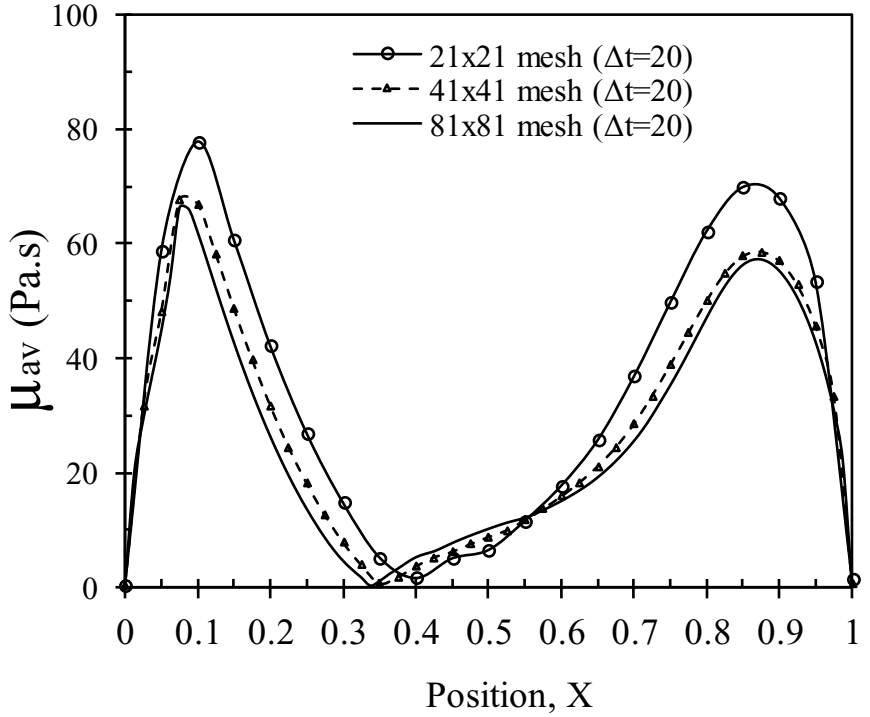

Figure 6-18: Artificial viscosity for different grid spacings and number of timesteps of 20

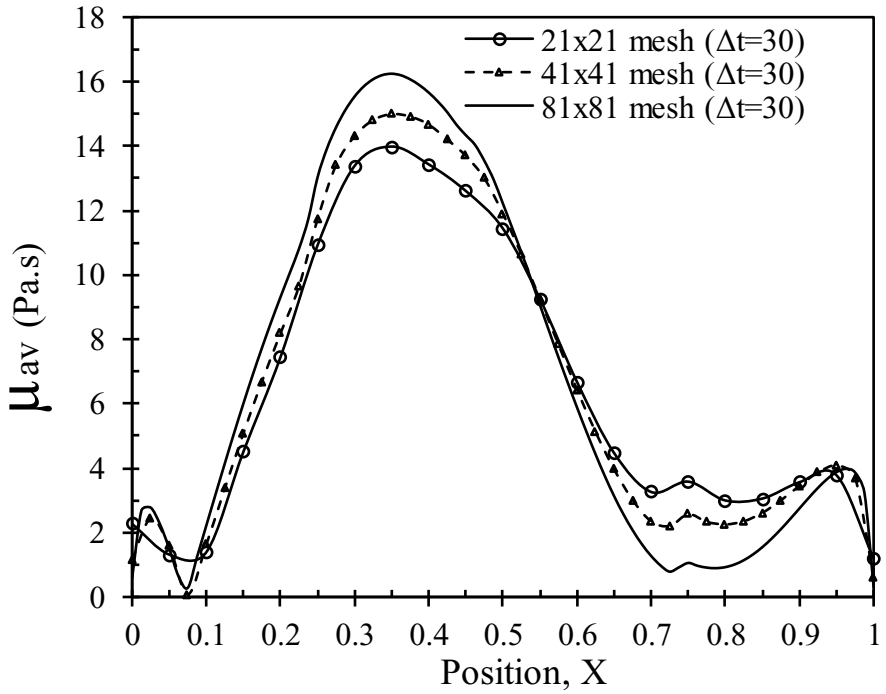

Figure 6-19: Artificial viscosity for different grid spacings and number of timesteps of 30

Also, the results indicate that the waveform in the artificial viscosity solution decreases and stabilizes with an increase in the number of timesteps. The stabilized artificial viscosity is important for correcting the algorithm, yielding minimally negative entropy production, minimizing numerical errors, and improving the overall accuracy of the model.

The results along the horizontal midplane (y = 0.5) has been considered in previous Graphs. In Figures 6.20 – 6.23, the results along the horizontal midplane at y = 0.75 will be analyzed. Figure 6.20 presents the variation of total negative transport entropy production, total negative entropy-based artificial viscosity, and numerical error in v-velocity as a function of grid spacing (21x21, 41x41, and 81x81) along the horizontal plane at y = 0.75, for the number of timesteps of 20.

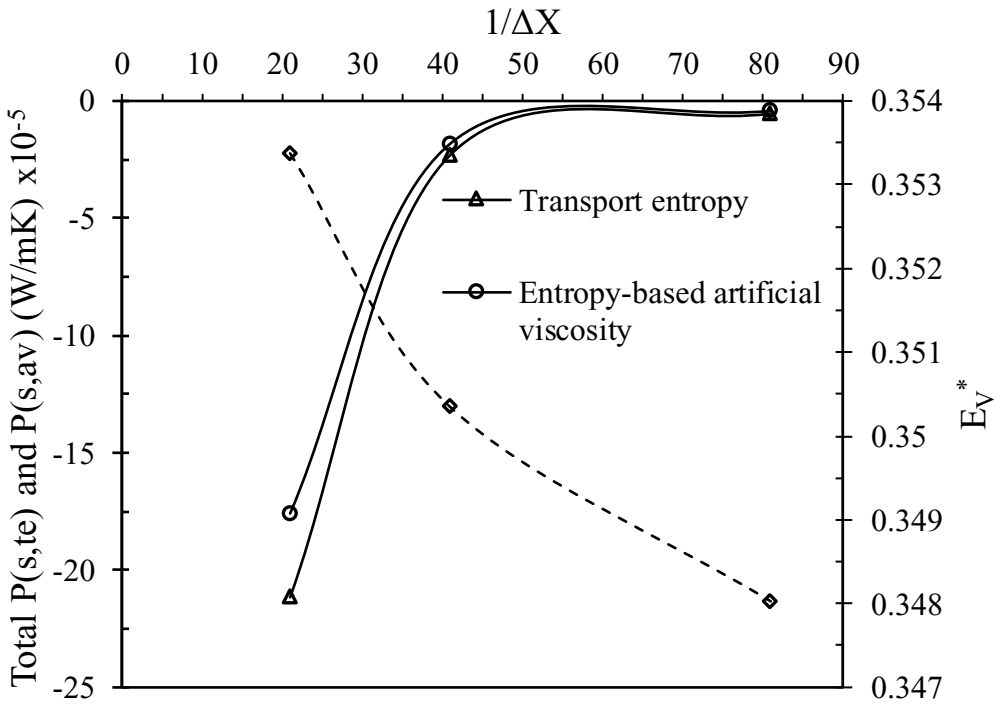

Figure 6-20: Variation of total negative transport entropy production, total negative entropy-based artificial viscosity, and numerical error in v-velocity with grid spacing along the horizontal plane (y=0.75), for the number of timesteps of 20

Similar to the case of y = 0.5, the results indicate that the total negative transport entropy production and total negative entropy-based artificial viscosity decreases as the grid density increases. It is also observed that as the total negative transport entropy production and total negative entropy-based artificial viscosity decrease, the numerical error in v-velocity also decreases.

The number of timesteps is increased to 30, and the variation of total negative transport entropy production, total negative entropy-based artificial viscosity, and numerical error in v-velocity as a function of grid spacing (21x21, 41x41, and 81x81) along the horizontal plane at y = 0.75, is analyzed in Figure 6.21.

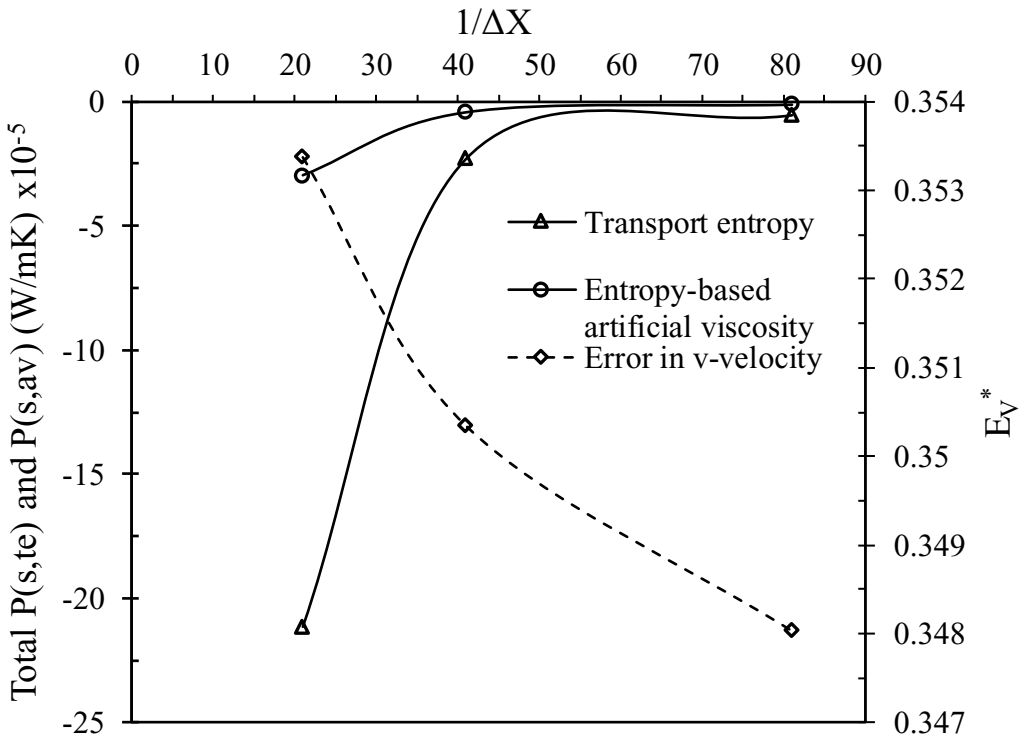

Figure 6-21: Variation of total negative transport entropy production, total negative entropy-based artificial viscosity, and numerical error in v-velocity with grid spacing along the horizontal plane (y=0.75) for the number of timesteps of 30

The results show that finer grids minimize the total negative transport entropy production and total negative entropy-based artificial viscosity. Again, like the case of y = 0.5, it is also observed that the numerical error in v-velocity decreases as the total negative transport entropy production and total negative entropy-based artificial viscosity decrease. Furthermore, as the number of timesteps is increased, the entropy-based artificial viscosity approaches zero.

In Figures 6.22 and 6.23, the variation of the numerical error in temperature is compared with the total negative transport entropy production, and total negative entropy-based

artificial viscosity, as a function of grid spacing along the horizontal midplane at y = 0.75 for the number of timesteps of 20 and 30, respectively.

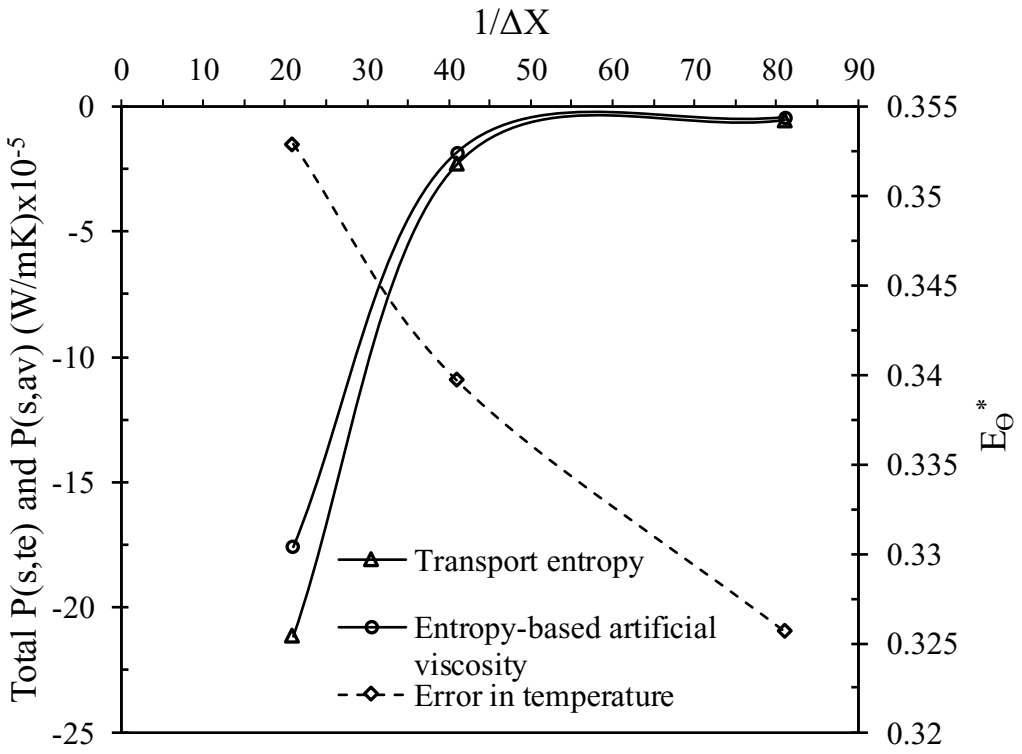

Figure 6-22: Variation of total negative transport entropy production, total negative entropy-based artificial viscosity, and numerical error in temperature with grid spacing along the horizontal plane (y=0.75), for a number of timesteps of 20

Like the case of numerical error in v-velocity and y = 0.5, the results show that the total negative transport entropy production and total negative entropy-based artificial viscosity decrease with finer grids, and the numerical error in temperature decreases as the total negative entropy-based artificial viscosity and total negative transport entropy production decrease. It is also observed that the entropy-based artificial viscosity yields less negative values compared to the transport entropy production for each grid spacing, and the entropy-based artificial viscosity tends to zero as the number of timesteps is increased.

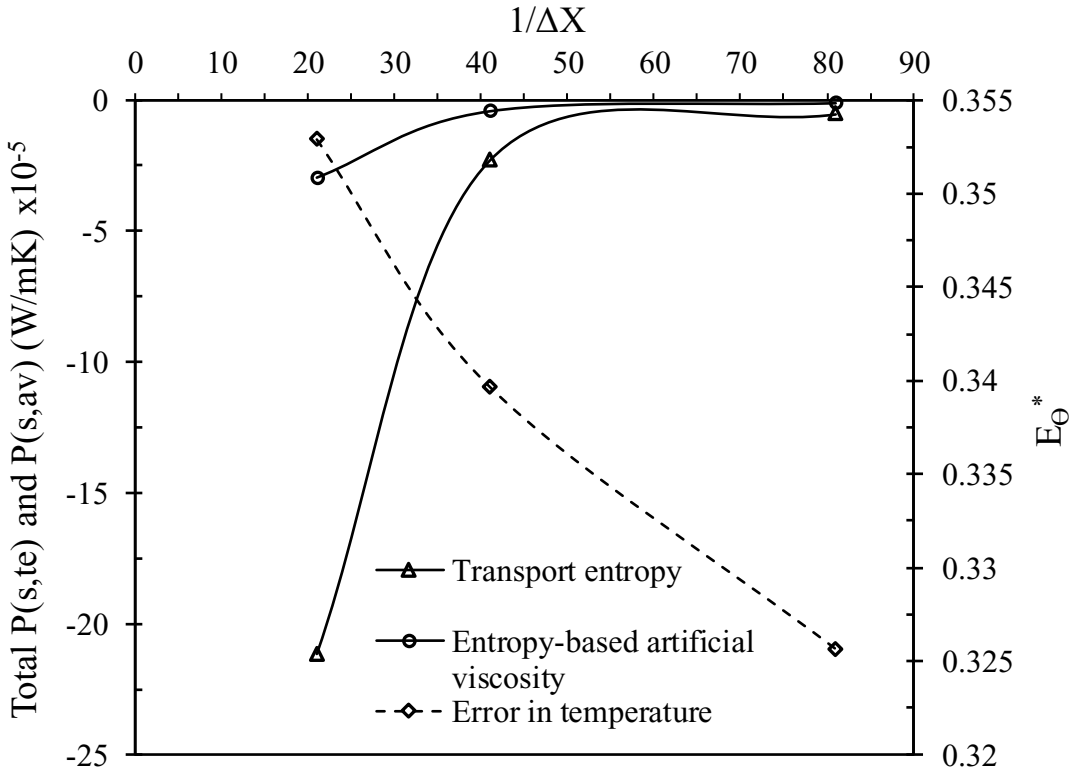

Figure 6-23: Variation of total negative transport entropy production, total negative entropy-based artificial viscosity, and numerical error in temperature with grid spacing along the horizontal plane (y=0.75) for a number of timesteps of 30

Figure 6.24 (a) shows a comparison of temperature distributions of the present study and that of the entropy-based artificial viscosity model with past data presented by Khanafer et al. [94]. Figure 6.24 (b) presents a comparison of the u-velocity of the present study and that of the entropy-based artificial viscosity model with past results of Engelman [181]. It is observed from the results that the artificial viscosity model is in good agreement with the benchmark solutions.

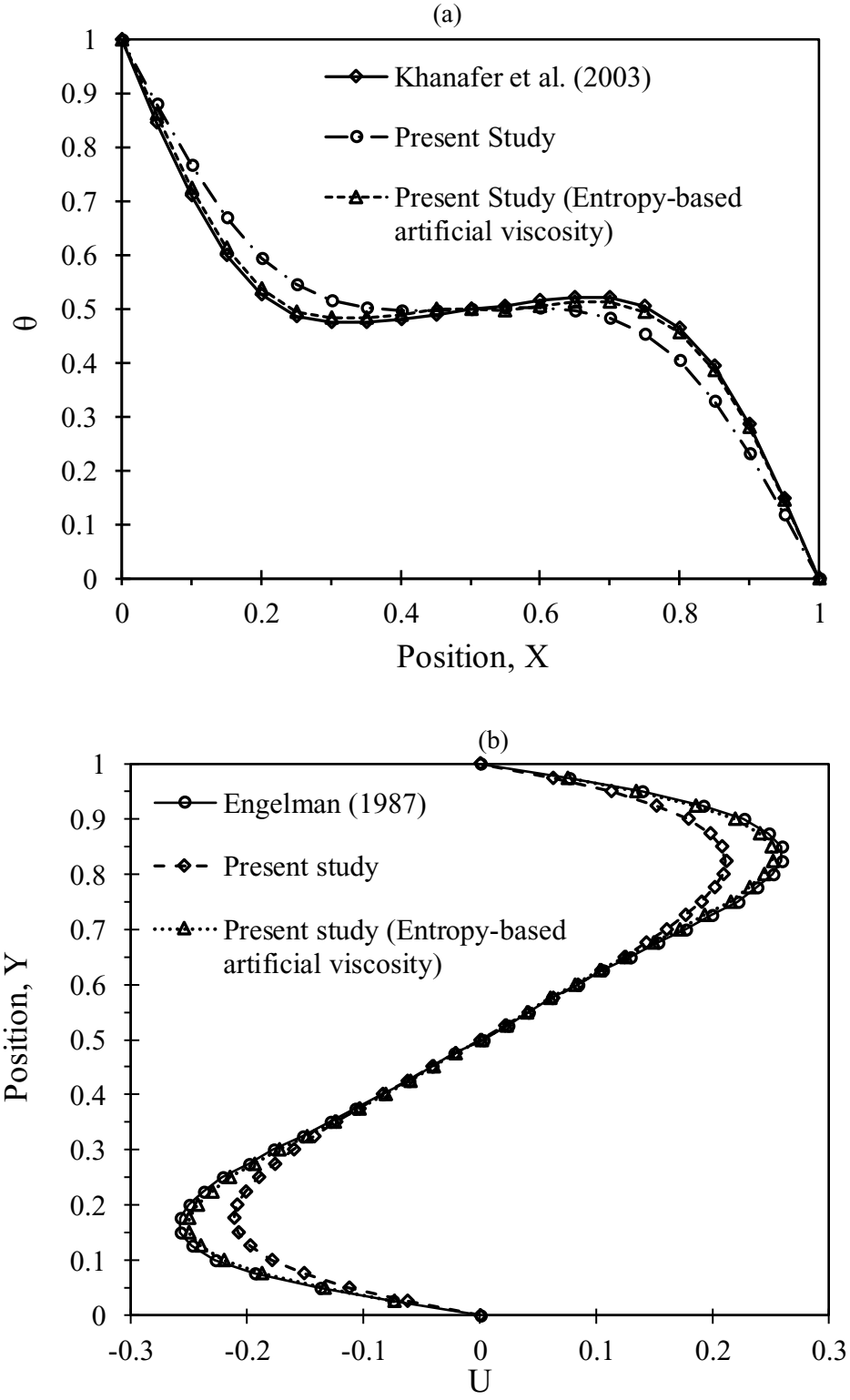

Figure 6-24: (a) Temperature and (b) velocity using the entropy-based artificial viscosity model

Hence, the results suggest that the use of the entropy-based artificial viscosity considerably minimizes the negative values in entropy production and reduces the numerical errors in the temperature and v-velocity results, thereby enhancing the accuracy of the numerical model.

In summary, the results in Figures 6.20 – 6.24 shows that the characteristics of the negative entropy-based artificial viscosity and the negative transport entropy production along the horizontal plane at y = 0.75 has a similar pattern with the results along y = 0.5. This is an indication that entropy-based artificial viscosity is effective as an algorithm corrective mechanism in different regions of the geometry. The results suggest that the application of the entropy-based artificial viscosity significantly minimizes the negative values in entropy production across the geometry and reduces the numerical errors in both velocity and temperature results, thereby improving the accuracy of the numerical model.

6.4 Conclusions

This chapter presented the development of a corrective mechanism in the numerical algorithm. The corrective mechanism was developed by using the transport form of the entropy production to calculate a parameter called the entropy-based artificial viscosity. It remodeled the diffusion coefficient in the momentum conservation equations to minimize the numerical error in the algorithm. The modification ensured that the transport entropy production was minimally negative.

The results of the modified algorithm for natural convection in cavities were presented and discussed for horizontal midplanes. It was shown that as the number of timesteps increased,

the entropy-based artificial viscosity stabilized and reached convergence. As a result, the negative entropy production decreased until it became minimally negative. The results also showed that finer grids produced less negative entropy production. For example, the entropy-based artificial viscosity for the 21x21 mesh had a total negative entropy production of -2.32 (W/m^3K), while the entropy-based artificial viscosity for the 41x41 mesh yielded -1.89 (W/m^3K), and -1.62 (W/m^3K) by the entropy-based artificial viscosity for the 81x81 mesh. It was also analyzed in this chapter that as the entropy-based artificial viscosity stabilized, the numerical accuracy was improved.

Overall, the analysis presented in this chapter indicated that the use of the entropy-based artificial viscosity significantly minimizes the negative values of entropy production and reduces the error in the velocities and temperature results, thereby improving the numerical accuracy of the model. The presented results also suggested that the grid spacing and number of timesteps are important parameters in the application of the entropy-based artificial viscosity as an algorithm corrective mechanism.

7 CONCLUSIONS AND RECOMMENDATIONS

7.1 Summary and Conclusions

In this thesis, a new approach is presented for how entropy and the Second Law of Thermodynamics can be used as tools for the improvement of energy efficiency and numerical modeling of thermal engineering systems. Past conventional methods generally detect energy losses on a system-wide or global scale, while the margins for improving the efficiency for existing devices are often relatively small. However, entropy-based design tracks energy losses locally and therefore can offer higher levels of system efficiency and energy savings in various applications.

This thesis presented a numerical investigation of entropy production and heat transfer for natural and mixed convection in rectangular enclosures including those filled with nanofluids. For the analysis with nanofluids, an optimum nanoparticle volume fraction is determined for which entropy production is minimized. The study also compared the natural convection heat transfer and entropy production for different nanofluids in the enclosure to determine the optimal nanofluid that is best suited for each system. An aspect ratio sensitivity study was also performed. A comparison of the heat transfer rates and entropy production for Cu-water, Al_2O_3-water, and TiO_2-water nanofluids in the enclosure was performed. The results indicated a reduction in the rate of entropy production and an increase in heat conduction when the nanoparticle volume fraction increases. Among the nanofluids compared, Cu-water was found to produce the lowest entropy production and best heat transfer performance.

Results for the mixed convection case showed that an optimum value of the nanoparticle volume fraction can be achieved, as well as a wall velocity, for which the total rate of entropy production is minimized. It was also observed that the total entropy production increases with an increase in the aspect ratio of the enclosure. Overall, the study has presented a new approach for the application of the Second Law, entropy generation minimization and heat transfer enhancement in mixed and natural convection of nanofluids in enclosures.

The thesis also examined both physical and computational characteristics of entropy generation. Numerical methods may destroy or produce computational entropy due to approximation errors that lead to non-physical numerical results, artificial dissipation, or other discretization errors. A Second Law formulation was presented and analyzed in this thesis based on different forms of the positive-definite and entropy transport equations. In order to assess the numerical error, a new parameter called the "apparent entropy production difference" was established based on the difference between the transport and positive-definite forms of the entropy production rate. A relationship between this difference and numerical errors in each control volume was developed and discussed.

Furthermore, this thesis examined entropy production of mixed convection in lid-driven and isothermal wall cavities filled with various fluids. It was observed that the apparent entropy production difference is related to the numerical error. The normalized peak apparent entropy production difference showed a reasonable agreement with the normalized peak numerical error at corresponding nodes. It is anticipated that similar trends exist for other flow conditions and geometrical configurations.

This thesis further presented a new model of the apparent entropy production difference, numerical solution errors, and a new trend between these variables. Grid refinement studies were performed, and their effects on the apparent entropy production difference were reported. The normalized peak values of apparent entropy production and numerical error were connected. The results from the lid-driven cavity problem suggested a relationship between the numerical error in u-velocity and the apparent entropy production difference. Similar results for velocity and temperature were obtained for natural convection in a cavity. The effects of grid size on the relationship were analyzed.

A corrective mechanism in the numerical algorithm was also developed. The transport form of the entropy production was used to calculate a parameter (entropy-based artificial viscosity) and remodel the diffusion coefficient in the momentum conservation equations to minimize the numerical error in the algorithm. This modification of the algorithm also ensured that the transport entropy production was minimally negative.

The modified algorithm was tested on a case study of natural convection in enclosures. Results were analyzed and discussed for horizontal midplanes. It was observed that as the number of timesteps increased, the entropy-based artificial viscosity stabilized and reached convergence. Also, as the entropy-based artificial viscosity stabilized, the negative entropy production decreased until it became minimally negative. As the entropy-based artificial viscosity stabilized, the numerical accuracy was enhanced. The results also showed that finer grids produced less negative entropy production.

Overall, the analysis presented in this study suggested that the grid spacing and number of timesteps are important parameters in the application of the entropy-based artificial

viscosity as an algorithm corrective mechanism. The results indicated that the application of the entropy-based artificial viscosity significantly minimizes the negative values of entropy production and reduces the error in the velocities and temperature results, thereby enhancing the accuracy of the numerical model.

In summary, the main conclusions and major contributions from this thesis are outlined as follows.

1. This thesis presented a new application of entropy and the Second Law for the mapping of available energy losses in a system. It has described design modifications to minimize irreversibilities and enhance energy efficiency.
2. This thesis also outlined the application of the Second Law to formulate a new entropy-based indicator for numerical error characterization, which can be useful to predict trends in the solution errors for computational heat transfer and fluid flow.
3. Local values of the computed entropy production have provided a valuable new metric because the overall performance of thermofluid systems can be improved by modifying design parameters locally based on the local entropy production rates.
4. The new approach for numerical error characterization can use the distribution and peak values of the apparent entropy production difference to predict trends in the solution errors for computational heat transfer and fluid flow.
5. The new model of entropy production and heat transfer for natural and mixed convection can predict and optimize the effects of nanoparticle volume fraction on heat conduction and entropy production. It predicted the optimum nanoparticle volume fraction for which entropy production is minimized.

6. The formulation has also provided a new corrective mechanism on the numerical algorithm. A parameter known as the entropy-based artificial viscosity was used to remodel the diffusion coefficient in the momentum conservation equations to reduce numerical errors in the solution algorithm. This modification aimed to ensure that the transport entropy production is minimally negative, and that the accuracy of the model is enhanced.

7.2 Recommendations for Future Research

Further research is recommended in the following areas.

- Entropy and Second Law predictions should be extended to other flow applications including turbulent flows. Local energy losses have been analyzed successfully in internal flows. The application of entropy production analysis in external flows will be useful for drag prediction.
- A Second Law formulation based on different forms of the positive-definite and entropy transport equations was used to obtain entropy-based numerical error indicators for convective heat transfer. This thesis considered mixed convection in lid-driven and isothermal wall cavities filled with various fluids. A correlation factor or higher order relationship between the apparent entropy production difference and numerical error is recommended for more complex flow configurations and geometries. Also, it is recommended to implement an entropy-based corrective mechanism to further modify the convective scheme to ensure positive entropy production and further reduce the numerical errors.

REFERENCES

[1] A. Bejan, Entropy generation minimization: the method of thermodynamic optimization of finite-time Systems and finite-time processes, CRC Press, Boca Raton, FL, 1996.

[2] G. F. Naterer, J. A. Camberos, Entropy–based analysis and design of fluids engineering systems, CRC Press, Boca Raton, FL, 2008.

[3] G. F. Naterer, Constructing an entropy-stable upwind scheme for compressible fluid flow computations, AIAA Journal. 37. 3 (1999) 303-312.

[4] R. A. Cox, B. M. Argrow, Entropy production in finite-difference schemes, AIAA Journal. 31.1 (1992) 210-211.

[5] G. F. Naterer, G. E. Schneider, Use of the second law for artificial dissipation in compressible flow discrete analysis, AIAA Journal of Thermophysics and Heat Transfer. 8.3 (1994) 500-506.

[6] G. F. Naterer, J. A. Camberos, The role of entropy and the second law in computational Thermofluids. AIAA Paper 2001-2758, AIAA 35th Thermophysics Conference, Anaheim, CA, June 11-14, 2001.

[7] O. B. Adeyinka, G. F. Naterer, Apparent entropy production difference with heat and fluid flow irreversibilities, Numerical Heat Transfer: Part B. 42.5 (2002) 411-436.

[8] M. J. Moran, H. N. Shapiro, D. D. Boettner, M. B. Bailey, Fundamentals of engineering thermodynamics. John Wiley & Sons, 2010.

[9] J. A. Camberos, Revised interpretation of work potential in thermophysical processes, AIAA Journal of Thermophysics and Heat Transfer. 14.2 (2000) 177-185.

[10] B. Roth, D. Mavris, A Method for propulsion technology impact evaluation via thermodynamic work potential, 9th AIAA / USAF / NASA/ ISSM symposium on multidisciplinary analysis and optimization, AIAA paper 2000-4854, Long Beach, CA, 2000.

[11] D. J. Moorhouse, C. F. Suchomel, Exergy methods applied to the hypersonic vehicle challenge, 32nd AIAA Plasmadynamics and laser conference, 4th weakly ionized gases workshops, AIAA paper 2001-3063, AIAA, Anaheim, CA, 2001.

[12] K. Pope, I. Dincer, G. F. Naterer, Energy and exergy efficiency comparison of horizontal and vertical axis wind turbines. Renewable Energy 35.9 (2010) 2102-2113.

[13] A. R. Mamouri, A. B. Khoshnevis, E. Lakzian, Entropy generation analysis of S825, S822, and SD7062 offshore wind turbine airfoil geometries, Ocean Engineering 173 (2019) 700-715.

[14] M. Nazeryan, E. Lakzian, Detailed entropy generation analysis of a Wells turbine using the variation of the blade thickness, Energy 143 (2018) 385-405.

[15] A. Bejan, Aduanced Engineering Thermodynamics, John Willey and Son, Inc., USA, 2nd ed., 1997.

[16] M. Rosen, I. Dincer, Effect of varying dead-state properties on energy and exergy analyses of thermal systems, International Journal of Thermal Science. 43.2 (2004) 121-133.

[17] I. Dincer, A. Z. Sahin, A new model for thermodynamic analysis of a drying process, International Journal of Heat and Mass Transfer. 47.4 (2004) 645-652.

[18] D. Poulikakos, A. Bejan, A fin geometry for minimum entropy generation in forced convection, Transactions of the ASME, 104 (1982) 616-623.

[19] S. M. Zubair, P. V. Kadaba, R. B. Evans, Second-Law-Based thermoeconomic optimization of two-phase heat exchangers, Journal of Heat Transfer, 109 (1987) 287-294.

[20] O. B. Adeyinka, G. F. Naterer, Optimization correlation for entropy production and energy availability in film condensation heat transfer, International Communications in Heat and Mass Transfer, 31.4 (2004) 513-524.

[21] E. Sciubba, Calculating entropy with CFD, Mechanical Engineering, 119.10 (1997) 86.

[22] G. Natalini, E. Sciubba, Minimization of the local rates of entropy production in the design of air-cooled gas turbine blades, ASME Journal of Engineering for Gas Turbine and Power, 121(1999) 466 - 475.

[23] S. M. Kresta, P. E. wood, The Flow Field Produced by a pitched Blade Turbine: characterization of the Turbulence and Estimation of the Dissipation Rate," Chemical Engineering Science, 48 (1993). I76I-I774.

[24] A. C. Baytas, Entropy generation for natural convection in an inclined porous cavity, International Journal of Heat and Mass Transfer. 43 (2000) 2089-2099.

[25] E. Abu-Nada and H. F. Oztop, Effects of inclination angle on natural convection in enclosures filled with Cu–water nanofluid, International Journal of Heat and Fluid Flow. 30 (2009) 669–678.

[26] M. Ghalambaz, A. Doostanidezfuli, H. Zargartalebi, A. J. Chamkha. MHD phase change heat transfer in an inclined enclosure: Effect of a magnetic field and cavity inclination, Numerical Heat Transfer, Part A. 71.1(2017) 91-109.

[27] K. Kahveci, Buoyancy driven heat transfer of nanofluids in a tilted enclosure, Journal of Heat Transfer. 132 (2010) 062501.

[28] C. H. Cheng, W. P. Ma, W. H. Huang, Numerical predictions of entropy generations for mixed convective flows in a vertical channel with transverse fin array, International Communications in Heat and Mass Transfer. 21.4 (1994) 519-530.

[29] S. Mahmud, R. A. Fraser, Magnetohydrodynamic free convection and entropy generation in a square porous cavity, International Journal of Heat and Mass Transfer. 47 (2004) 3245–3256.

[30] A. Z. Sahin, Entropy generation and pumping power in a turbulent fluid flow through a smooth pipe subjected to constant heat flux, Exergy, an International Journal, 2(2002) 314-321.

[31] Y. Demirel, Irreversibility profiles in a circular couette flow of temperature dependence materials, International Communications in Heat and Mass Transfer, 26(1999) 75-83.

[32] A. Z. Sahin, Entropy generation in turbulent liquid flow through a smooth duct subjected to constant wall temperature, International Journal of Heat and Mass Transfer, 43(2000) 1469-1478.

[33] O. B. Adeyinka, G. F. Naterer, Entropy-based metric for component level energy management: application to diffuser performance, International Journal of Energy Research. 29.11(2005) 1007-1024.

[34] P. Biswal, T. Basak, Entropy generation vs energy efficiency for natural convection based energy flow in enclosures and various applications: A review, Renewable and Sustainable Energy Reviews 80 (2017) 1412-1457.

[35] S. Chen, R. Du, Entropy generation of turbulent double-diffusive natural convection in a rectangle cavity, Energy. 36.3 (2011) 1721–34.

[36] A. Mchirgui, N. Hidouri, M. Magherbi, A. B. Brahim, Entropy generation in double-diffusive convection in a porous square cavity using Darcy–Brinkman formulation, Transport in porous media. 93.1 (2012) 223-240.

[37] G. Ruocco, Entropy generation in conjugate heat transfer from a discretely heated plate to an impinging confined jet, International communications in heat and mass transfer. 24.2 (1997) 201-210.

[38] N. Hidouri, M. Magherbi, H. Abbassi, A. B. Brahim, Entropy generation in double-diffusive convection in presence of the Soret effect, Progress in Computational Fluid Dynamics, 7.5 (2007) 237-246.

[39] Z. M. Behrooz, R. Dehnavi, Heat transfer in a large triangular-roof enclosure based on the second law analysis, Heat and Mass Transfer. 51.7 (2015) 931-940.

[40] Y. Varol, H. F. Oztop, A. Koca, E. Avci, Forecasting of entropy production due to buoyant convection using support vector machines (SVM) in a partially cooled square cross-sectional room, Expert Systems with Applications. 36.3 (2009) 5813-5821.

[41] Y. Yonghua, A. Fan, Y. Liang, S. Jin, W. Liu, F. Dai, Entropy generation analysis for laminar thermal augmentation with conical strip inserts in horizontal circular tubes, International Journal of Thermal Sciences. 88 (2015) 201-214.

[42] T. H. Ko, K. Ting, Entropy generation and thermodynamic optimization of fully developed laminar convection in a helical coil, International Communications in Heat and Mass Transfer. 32.1-2 (2005) 214-223.

[43] V. M. Rathnam, P. Biswal, T. Basak, Analysis of entropy generation during natural convection within entrapped porous triangular cavities during hot or cold fluid disposal, Numerical Heat Transfer, Part A: Applications. 69.9 (2016) 931-956.

[44] T. Basak, R. Anandalakshmi, T. P. A. Sruthi, Analysis of entropy generation due to natural convection for hot and cold materials confined within two entrapped triangular cavities, Industrial and Engineering Chemistry Research. 52.46 (2013) 16414–16426.

[45] B. A. Abu-Hijleh, I. N. Jadallah, E. Abu Nada, Entropy generation due to natural convection from a horizontal isothermal cylinder in oil, International communications in heat and mass transfer. 25.8 (1998) 1135-1143.

[46] B. A. Abu-Hijleh, M. Abu-Qudais, E. Abu-Nada, Numerical prediction of entropy generation due to natural convection from a horizontal cylinder, Energy. 24.4 (1999) 327-333.

[47] I. Dagtekin, H. F. Oztop, A. Z. Şahin, An analysis of entropy generation through a circular duct with different shaped longitudinal fins for laminar flow, International Journal of Heat and Mass Transfer. 48.1 (2005) 171-181.

[48] Y. Demirel, R. Kahraman, Thermodynamic analysis of convective heat transfer in an annular packed bed, International Journal of Heat and Fluid Flow. 21.4 (2000) 442-448.

[49] Y. Demirel, Thermodynamic optimization of convective heat transfer in a packed duct, Energy. 20.10 (1995) 959-967.

[50] S. Z. Shuja, B. S. Yilbas, M. Kassas, Entropy generation in a square cavity International Journal of Numerical Methods for Heat & Fluid Flow. 20 (2010) 332–347.

[51] S. Z. Shuja, B. S. Yilbas, M. O. Budair, Natural convection in a square cavity with a heat generating body: entropy consideration, Heat and Mass Transfer. 36.4 (2000) 343-350.

[52] W. J. Yang, T. Furukawa, S. Torii, Optimal package design of stacks of convection-cooled printed circuit boards using entropy generation minimization method, International Journal of Heat and Mass Transfer. 51.15-16 (2008) 4038-4046.

[53] A. Erek, I. Dincer, An approach to entropy analysis of a latent heat storage module, International Journal of Thermal Sciences. 47.8 (2008) 1077-1085.

[54] S. M. Flueckiger, S. V. Garimella, Second-law analysis of molten-salt thermal energy storage in thermoclines, Solar Energy. 86.5 (2012) 1621-1631.

[55] D. Das, T. Basak, Role of distributed/discrete solar heaters for the entropy generation studies in the square and triangular cavities during natural convection, Applied Thermal Engineering. 113 (2017) 1514-1535.

[56] K. Ghachem, L. Kolsi, C. Maatki, A. K. Hussein, M. N. Borjini, Numerical simulation of three-dimensional double-diffusive free convection flow and irreversibility studies in a solar distiller, International Communications in Heat and Mass Transfer. 39.6 (2012) 869-876.

[57] P. Naphon, On the performance and entropy generation of the double-pass solar air heater with longitudinal fins, Renewable Energy. 30.9 (2005) 1345-1357.

[58] P. Biswal, T. Basak, Role of various concave/convex walls exposed to solar heating on entropy generation during natural convection within porous right angled triangular enclosures, Solar Energy. 137 (2016) 101-121.

[59] R. Nasrin, S. Parvin, M. A. Alim, Effect of Prandtl number on free convection in a solar collector filled with nanofluid, Procedia Engineering. 56 (2013) 54-62.

[60] A. D. Risi, M. Milanese, D. Laforgia, Modelling and optimization of transparent parabolic trough collector based on gas-phase nanofluids, Renewable Energy. 58 (2013) 134-139.

[61] A. K. Tiwari, P. Ghosh, J. Sarkar, Solar water heating using nanofluids–a comprehensive overview and environmental impact analysis, International Journal of Emerging Technology and Advanced Engineering. 3.3 (2013) 221-224.

[62] A. D. Risi, M. Milanese, D. Laforgia, Modelling and optimization of transparent parabolic trough collector based on gas-phase nanofluids, Renewable Energy. 58 (2013) 134-139.

[63] H. Tyagi, P. Phelan, R. Prasher, Predicted efficiency of a low-temperature nanofluid-based direct absorption solar collector, Journal of solar energy engineering 131.4 (2009).

[64] M. M. Rahman, S. Mojumder, S. Saha, S. Mekhilef, R. Saidur, Effect of solid volume fraction and tilt angle in a quarter circular solar thermal collectors filled with CNT–water nanofluid, International Communications in Heat and Mass Transfer. 57 (2014) 79-90.

[65] J. Sarkar, Performance of a flat-plate solar thermal collector using supercritical carbon dioxide as heat transfer fluid, International Journal of Sustainable Energy 32.6 (2013) 531-543.

[66] R. Saidur, T. C. Meng, Z. Said, M. Hasanuzzaman, A. Kamyar, Evaluation of the effect of nanofluid-based absorbers on direct solar collector, International Journal of Heat and Mass Transfer. 55.21-22 (2012) 5899-5907.

[67] Z. Said, R. Saidur, N. A. Rahim, M. A. Alim, Analyses of exergy efficiency and pumping power for a conventional flat plate solar collector using SWCNTs based nanofluid, Energy and Buildings. 78 (2014) 1-9.

[68] M. Alipanah, P. Hasannasab, S. F. Hosseinizadeh, M. Darbandi, Entropy generation for compressible natural convection with high gradient temperature in a square cavity, International Communications in Heat and Mass Transfer. 37. 9 (2010): 1388-1395.

[69] M. H. Arshad, R. Kahraman, A. Z. Sahin, R. Ben-Mansour, Second law analysis of compressible flow through a diffuser subjected to constant heat flux at wall, Energy Conversion and Management 51, no. 12 (2010): 2808-2815.

[70] M. Yurusoy, B. S. YilbaŞ, M. Pakdemirli, Non-Newtonian fluid flow in annular pipes and entropy generation: temperature-dependent viscosity, Sadhana. 31.6 (2006) 683-695.

[71] M. Pakdemirli, B. S. Yilbas, Entropy generation in a pipe due to non-Newtonian fluid flow: Constant viscosity case, Sadhana. 31.1 (2006) 21-29.

[72] B. S. Yilbas, M. Yürüsoy, M. Pakdemirli, Entropy analysis for non-Newtonian fluid flow in annular pipe: constant viscosity case, Entropy. 6.3 (2004) 304-315.

[73] M. Magherbi, H. Abbassi, A. B. Brahim, Entropy generation at the onset of natural convection, International Journal of Heat and Mass Transfer. 46 (2003) 3441–3450.

[74] L. B. Erbay, Z. Altac, B. Sulus, An analysis of the entropy generation in a square enclosure, Entropy. 5 (2003) 496–505.

[75] B. S. Yilbas, S. Z. Shuja, S. A. Gbadebo, H. I. Abu Al-Hamayle, K. Boran, Natural convection and entropy generation in a square cavity, International Journal of Energy Research. 22 (1998) 1275–1290.

[76] A. Mukhopadhyay, Analysis of entropy generation due to natural convection in square enclosures with multiple discrete heat sources, International Communications in Heat and Mass Transfer. 37 (2010) 867–872.

[77] I. Dagtekin, H.F. Oztop, A. Bahloul, Entropy generation for natural convection in C-shaped enclosures, International Communications in Heat and Mass Transfer. 34 (2007) 502–510.

[78] S. Mahmud, A. K. M. S. Islam, Laminar free convection and entropy generation inside an inclined wavy enclosure, International Journal of Thermal Sciences. 42 (2003) 1003–1012.

[79] S. U. S. Choi, J. A. Estman, Enhancing thermal conductivity of fluids with nanoparticles, No. ANL/MSD/CP-84938; CONF-951135-29, Argonne National Laboratory, IL (United States). 231 (1995) 99-106.

[80] O. Aydin, W. J. Yang, Natural convection in enclosures with localized heating from below and symmetrical cooling from sides, International Journal of Numerical Method for Heat and Fluid Flow. 10.5 (2000) 518-529.

[81] B. Calcagni, F. Marsili, M. Paroncini, Natural convective heat transfer in square enclosures heated from below, Applied Thermal Engineering. 25.16 (2005) 2522-2531.

[82] S. Abdelkader, R. Mebrouk, B. Abdellah, B. Khadidja, Natural convection in a horizontal wavy enclosure, Journal of Applied Sciences Research. 7 (2007) 334–341.

[83] J. Rostami, Unsteady natural convection in an enclosure with vertical wavy walls, Journal of Heat and Mass Transfer 44 (2008) 1079–1087.

[84] R. Saidur, K.Y. Leong, H.A. Mohammad, A review on applications and challenges of nanofluids, Renewable and Sustainable Energy Reviews. 15.3 (2011) 1646-1668.

[85] V. Trisaksri, S. Wongwises, Critical review of heat transfer characteristics of nanofluids, Renewable and Sustainable Energy Reviews .11.3 (2007) 512-523.

[86] W. Daungthongsuk, S. Wongwises, A critical review of convective heat transfer of nanofluids, Renewable and Sustainable Energy Reviews. 11.5 (2007) 797-817.

[87] Y. Li, S. Tung, E. Schneider, S. Xi, A review on development of nanofluid preparation and characterization, Powder Technology. 196.2 (2009) 89-101.

[88] S. Kakaç, A. Pramuanjaroenkij, Review of convective heat transfer enhancement with nanofluids, International Journal of Heat and Mass Transfer. 52.13-14 (2009) 3187-3196.

[89] A. Ghadimi, R. Saidur, H.S.C. Metselaar, A review of nanofluid stability properties and characterization in stationary conditions. International Journal of Heat and Mass Transfer. 54.17-18 (2011) 4051-4068.

[90] K. Khanafer, K. Vafai, A critical synthesis of thermophysical characteristics of nanofluids, International Journal of Heat and Mass Transfer. 54.19-20 (2011): 4410-4428.

[91] G. Li, M. Aktas, Y. Bayazitoglu, A review on the discrete Boltzmann model for nanofluid heat transfer in enclosures and channels, Numerical Heat Transfer. Part B. 67.6 (2015) 463-488.

[92] H. E. Mghari, H. Louahlia-Gualous, E. Lepinasse, Numerical study of nanofluids condensation heat transfer in a square microchannel, Numerical Heat Transfer. Part A. 69.9 (2016) 957-976.

[93] K. S. Hwang, J. H. Lee, S. P. Jang, Buoyancy-driven heat transfer of water-based Al_2O_3 nanofluids in a rectangular cavity, International Journal of Heat and Mass Transfer. 50 (2007) 4003–4010.

[94] K. Khanafer, K. Vafai, M. Lightstone, Buoyancy-driven heat transfer enhancement in a two-dimensional enclosure utilizing nanofluids, International Journal of Heat and Mass Transfer. 46 (2003) 3639–3653.

[95] G. A. Sheikhzadeh, A. Arefmanesh, M. H. Kheirkhah, R. Abdollahi, Natural convection of Cu–water nanofluid in a cavity with partially active sidewalls, European Journal of Mechanics B/Fluid. 30 (2011) 166–176.

[96] H. F. Oztop and E. Abu-Nada, Numerical study of natural convection in partially heated rectangular enclosures filled with nanofluids, International Journal of Heat and Fluid Flow. 29 (2008) 1326–1336.

[97] M. Shahi, A. H. Mahmoudi, A. H. Raouf, Entropy generation due to natural convection cooling of a nanofluid, International Communications in Heat and Mass Transfer. 38.7 (2011) 972-983.

[98] J. Li, C. Kleinstreuer, Entropy generation analysis for nanofluid flow in microchannels, Journal of Heat Transfer. 132.12 (2010) 122401.

[99] P. K. Singh, K. B. Anoop, T. Sundararajan, S.K. Das, Entropy generation due to flow and heat transfer in nanofluids, International Journal of Heat and Mass Transfer. 53.21-22 (2010) 4757-4767.

[100] M. Moghaddami, A. Mohammadzade, S. A. Varzane Esfehani, Second law analysis of nanofluid flow, Energy Conversion Management. 52.2 (2011) 1397-1405.

[101] Y. Feng, C. Kleinstreuer, Nanofluid convective heat transfer in a parallel-disk system, International Journal of Heat and Mass Transfer. 53.21-22 (2010) 4619-4628.

[102] A. Kashani, A. A. Ranjbar, M. Mastiani, H. Mirzaei, Entropy generation and natural convection of nanoparticle-water mixture (nanofluid) near water density inversion

in an enclosure with various patterns of vertical wavy walls, Applied Mathematics and Computation. 226 (2014): 180-193.

[103] A. H. Mahmoudi, M. Shahi, F. Talebi, Entropy generation due to natural convection in a partially open cavity with a thin heat source subjected to a nanofluid, Numerical Heat Transfer, Part A: Applications. 61.4 (2012) 283-305.

[104] H. Khorasanizadeh, J. Amani M. Nikfar, Numerical investigation of Cu-water nanofluid natural convection and entropy generation within a cavity with an embedded conductive baffle, Scientia Iranica. 19.6 (2012) 1996-2003.

[105] K. Y. Leong, R. Saidur, T. M. I. Mahlia, Y. H. Yau, Entropy generation analysis of nanofluid flow in a circular tube subjected to constant wall temperature, International Communications in Heat and Mass Transfer. 39.8 (2012): 1169-1175.

[106] T. Armaghani, A. Kasaeipoor, N. Alavi, M. M. Rashidi, Numerical investigation of water-alumina nanofluid natural convection heat transfer and entropy generation in a baffled L-shaped cavity, Journal of Molecular Liquids. 223 (2016) 243-251.

[107] M. A. Ismael, T. Armaghani, A. J. Chamkha, Conjugate heat transfer and entropy generation in a cavity filled with a nanofluid-saturated porous media and heated by a triangular solid, Journal of the Taiwan Institute of Chemical Engineers. 59 (2016) 138-151.

[108] M. Salari, E. H. Malekshah, M. H. Esfe, Three dimensional simulation of natural convection and entropy generation in an air and MWCNT/water nanofluid filled

cuboid as two immiscible fluids with emphasis on the nanofluid height ratio's effects, Journal of Molecular Liquids. 227 (2017) 223-233.

[109] C. C. Cho, Influence of magnetic field on natural convection and entropy generation in Cu–water nanofluid-filled cavity with wavy surfaces, International Journal of Heat and Mass Transfer. 101 (2016) 637-647.

[110] F. Selimefendigil, H. F. Oztop, N. Abu-Hamdeh, Natural convection and entropy generation in nanofluid filled entrapped trapezoidal cavities under the influence of magnetic field, Entropy. 18.2 (2016) 43.

[111] M. Mamourian, K. M. Shirvan, I. Pop, Sensitivity analysis for MHD effects and inclination angles on natural convection heat transfer and entropy generation of Al_2O_3 water nanofluid in square cavity by response surface methodology, International Communications in Heat and Mass Transfer. 79 (2016) 46-57.

[112] A. Chamkha, M. Ismael, A. Kasaeipoor, T. Armaghani, Entropy generation and natural convection of CuO-water nanofluid in C-shaped cavity under magnetic field, Entropy. 18.2 (2016) 50.

[113] S. Chen, B. Yang, X. Xiao, C. Zheng, Analysis of entropy generation in double-diffusive natural convection of nanofluid, International Journal of Heat and Mass Transfer. 87 (2015) 447-463.

[114] C. C. Cho, H. T. Yau, C. H. Chiu, K. C. Chiu, Numerical investigation into natural convection and entropy generation in a nanofluid-filled U-shaped cavity, Entropy. 17.9 (2015) 5980-5994.

[115] O. Mahian, A. Kianifar, A. Z. Sahin, S. Wongwises, Entropy generation during Al_2O_3/water nanofluid flow in a solar collector: Effects of tube roughness, nanoparticle size, and different thermophysical models, International Journal of Heat and Mass Transfer. 78 (2014) 64-75.

[116] C. C. Cho, C. L. Chen, C. N. Chen, Natural convection heat transfer and entropy generation in wavy-wall enclosure containing water-based nanofluid, International Journal of Heat and Mass Transfer. 61 (2013) 749-758.

[117] M. A. Alim, Z. Abdin, R. Saidur, A. Hepbasli, M. A. Khairul, N. A. Rahim, Analyses of entropy generation and pressure drop for a conventional flat plate solar collector using different types of metal oxide nanofluids, Energy and Buildings. 66 (2013) 289-296.

[118] S. Parvin, R. Nasrin, M. A. Alim, Heat transfer and entropy generation through nanofluid filled direct absorption solar collector, International Journal of Heat and Mass Transfer. 71 (2014) 386-395.

[119] M. Mirzazadeh, A. Shafaei, F. Rashidi, Entropy analysis for non-linear viscoelastic fluid in concentric rotating cylinders. International Journal of Thermal Science. 47.12 (2008) 1701-1711.

[120] O. Mahian, S. Mahmud, S. Z. Heris, Analysis of entropy generation between co-rotating cylinders using nanofluids, Energy. 44.1 (2012) 438-446.

[121] G. F. Naterer, Finite Element Compressible Fluid Flow Prediction Using the Second Law of Thermodynamics, M.Sc. thesis, University of Waterloo, Waterloo, Ontario, Canada, 1991.

[122] P. Lax, Shock waves and entropy, Contributions to nonlinear functional analysis. Academic Press. (1971) 603-634.

[123] T. J. R. Hughes, L. P. Franca, M. Mallet, A new finite element formulation for computational fluid dynamics: I. Symmetric forms of the compressible Euler and Navier-Stokes equations and the second law of thermodynamics, Computer Methods in Applied Mechanics and Engineering. 54.2 (1986) 223-234.

[124] M. L. Merriam, Smoothing and the second law, Computer Methods in Applied Mechanics and Engineering. 64.1-3 (1987) 177-193.

[125] A. Majda, S. Osher, Numerical viscosity and the entropy condition, Communications on Pure and Applied Mathematics. 32.6 (1979) 797-838.

[126] G. F. Naterer, J. A. Camberos, Second law formulation for a stable velocity-temperature coupling in computational fluid flow, AIAA Paper 99-3514, AIAA 30th Fluid Dynamics Conf., Norfolk, VA, June 1999.

[127] M. L. Merriam, An Entropy-Based Approach to Nonlinear Stability, Ph.D. thesis, Stanford University, Stanford, CA, 1988.

[128] J. VonNeumann, R. D. Richtmyer, A method for the numerical calculation of hydrodynamic shocks, Journal of Applied Physics. 21.3 (1950) 232-237.

[129] R. D. Richtmyer, A proposed method for the calculation of shocks, Technical Report LA–671, Los Alamos Scientific Laboratory: Los Alamos, New Mexico, USA, 1948.

[130] M. L. Wilkins, Calculation of Elastic-Plastic Flow, Academic Press: New York, 3 (1964).

[131] M. L. Wilkins, Use of artificial viscosity in multidimensional fluid dynamic calculations, Journal of Computational Physics. 36.3 (1980) 281-303.

[132] J. Smagorjnsky, The beginnings of numerical weather prediction and general circulation modeling: early recollections, Advances in Geophysics. 25 (1983) 3-37.

[133] J. Smagorinsky, General circulation experiments with the primitive equations: I, The basic experiment, Monthly Weather Review 91.3 (1963) 99-164.

[134] M. Nazarov, J. Hoffman, Residual-based artificial viscosity for simulation of turbulent compressible flow using adaptive finite element methods, International Journal for Numerical Methods in Fluids. 71.3 (2013) 339-357.

[135] J. Albright, M. Shashkov, Locally adaptive artificial viscosity strategies for Lagrangian hydrodynamics, Computers & Fluids. (2020) 104580.

[136] G. E. Barter, D. L. Darmofal, Shock capturing with PDE-based artificial viscosity for DGFEM: Part I. Formulation, Journal of Computational Physics. 229.5 (2010) 1810–1827.

[137] R. Hartmann, Adaptive discontinuous Galerkin methods with shock-capturing for the compressible Navier–Stokes equations, International Journal for Numerical Methods in Fluids. 51.9–10 (2006) 1131–1156.

[138] T. V. Kolev, R. N. Rieben, A tensor artificial viscosity using a finite element approach, Journal of Computational Physics. 228.22 (2009) 8336-8366.

[139] P. Persson, J. Peraire, Sub-cell shock capturing for discontinuous Galerkin methods, 44th AIAA Aerospace Sciences Meeting and Exhibit. 2006.

[140] H. Yucel, M. Stoll, P. Benner, Discontinuous Galerkin finite element methods with shock-capturing for nonlinear convection dominated models, Computers and Chemical Engineering. 58 (2013) 278-287.

[141] J. Reisner, J. Serencsa, S. Shkoller, A space–time smooth artificial viscosity method for nonlinear conservation laws, Journal of Computational Physics. 235 (2013) 912-933.

[142] J. L. Guermond, R. Pasquetti, B. Popov, Entropy viscosity for conservation equations, V European Conference on Computational Fluid Dynamics. (Eccomas CFD 2010), 2010.

[143] M. O. Delchini, J. C. Ragusa, R. A. Berry, entropy viscosity method applied to euler equation, No. INL/CON-13-29941, Idaho National Laboratory (INL), 2013.

[144] A. Chaudhuri, G. B. Jacobs, W. S. Don, H. Abbassi, F. Mashayek, Explicit discontinuous spectral element method with entropy generation based artificial

viscosity for shocked viscous flows, Journal of Computational Physics. 332 (2017) 99-117.

[145] G. F. Naterer, Advanced Heat Transfer, 2nd ed., CRC Press, Boca Raton, FL, 2018.

[146] A. Bejan, Convection Heat Transfer. Hoboken, NJ: John Wiley & Sons, 2013.

[147] S. Patankar, Numerical Heat Transfer and Fluid Flow. New York, NY: CRC Press, 1980.

[148] G. E. Schneider, M. J. Raw, A skewed, positive influence coefficient upwinding procedure for control-volume-based finite element convection-diffusion computation, Numerical Heat Transfer, Part A, 9 (1986) 1-26.

[149] P. Keblinski, S. R. Phillpot, S. U. S. Choi, J. A. Eastman, Mechanisms of heat flow in suspensions of nano-sized particles (nanofluids), International Journal of Heat and Mass Transfer. 45(2002) 855-863.

[150] J. Koo, C. Kleinstreuer. Impact analysis of nanoparticle motion mechanisms on the thermal conductivity of nanofluids, International Communications in Heat and Mass Transfer. 32.9 (2005) 1111-1118.

[151] J. Buongiorno, Convective transport in nanofluids, Journal of Heat Transfer. 128.3 (2006) 240-250.

[152] H. C. Brinkman, The viscosity of concentrated suspensions and solutions. The Journal of Chemical Physics. 20.4 (1952) 571-571.

[153] J. R. Eggers, S. Kabelac, Nanofluids revisited, Applied Thermal Engineering. 106 (2016) 1114–1126.

[154] R. S. Vajjha, D. K. Das, B. M. Mahagaonkar, Density measurement of different nanofluids and their comparison with theory, Petroleum Science and Technology. 27.6 (2009) 612–624.

[155] T. P. Teng Y. H. Hung, Estimation and experimental study of the density and specific heat for alumina nanofluid, Journal of Experimental Nanoscience. 9.7 (2014) 707–718.

[156] S. Q. Zhou, R. Ni, Measurement of the specific heat capacity of water-based Al_2O_3 nanofluid, Applied Physics Letters. 92.9 (2008).

[157] P. C. Mishra, S. Mukherjee, S. K. Nayak, A. Panda, A brief review on viscosity of nanofluids, International Nanofluids Letters. 4.4 (2014) 109-120.

[158] G. de Vahl Davis, Natural convection of air in a square cavity: a benchmark numerical solution, International Journal of Numerical Methods in Fluids. 3.3 (1983) 249-264.

[159] M. Hortmann, M. Peric, G. Scheuerer, Finite volume multigrid predictions for laminar natural convection: benchmark solution, International Journal of Numerical Methods in Fluids. 11 (1990) 189-207.

[160] M. F. Lightstone, W. M. Collins, Simulation of natural convection of air in a square cavity using the GOTHIC thermohydraulic code, Proceedings of the CNA / CNS Annual Conference, Montreal, Canada, 1994.

[161] K. A. R. Ismail, V. L. Scalon, A Finite element free convection model for the side wall heated cavity, International Journal of Heat and Mass Transfer. 43 (2000) 1373-1389.

[162] A. C. Baytas, Optimization in an enclosure for minimum entropy generation in natural convection, Journal of Non-Equilibrium Thermodynamics. 22. 2 (1997) 45-155.

[163] B. A. Abu-Hijleh, W. N. Heilen, Entropy generation due to laminar natural convection over a heated rotating gylinder, International Journal Heat and Mass Transfer. 42 (1999) 4225-4233.

[164] S. Thankappan, J. Abraham, S. C. George, and S. Thomas, Rheological characterization of nanocomposites, In Characterization of Nanomaterials. (2018) 167-189, Woodhead Publishing.

[165] K. Bashirnezhad, S. Bazri, M. R. Safaei, M. Goodarzi, M. Dahari, O. Mahian, A. S. Dalkılıça, and S. Wongwises, Viscosity of nanofluids: a review of recent experimental studies, International Communications in Heat and Mass Transfer. 73 (2016) 114-123.

[166] B. Aladag, S. Halelfad, N. Doner, T. Maré, S. Duret, P. Estellé, Experimental investigations of the viscosity of nanofluids at low temperatures, Applied Energy. 97 (2012) 876-880.

[167] N. Masoumi, N. Sohrabi, A. Behzadmehr, A new model for calculating the effective viscosity of nanofluids, Journal of Physics D: Applied Physics. 42 (2009) 055501.

[168] Y. Xuan, W. Roetzel, Conceptions for heat transfer correlation of nanofluids, International Journal of Heat and Mass Transfer. 43 (2000) 3701-3707.

[169] S.E.B. Maïga, S.J. Palm, C.T. Nguyen, G. Roy, N. Galanis, Heat transfer enhancement by using nanofluids in forced convection flows, International Journal of Heat Fluid Flow. 26 (2005) 530-546.

[170] G. de Vahl Davis, and I. P. Jones, Natural convection in a square cavity: a comparison exercise, International Journal for numerical methods in fluids 3.3 (1983): 227-248.

[171] D. C. Wan, B. S. V. Patnaik, G. W. Wei, A new benchmark quality solution for buoyancy-driven cavity by discrete singular convolution, Numerical Heat Transfer, Part B. 40 (2001): 199-228.

[172] B. Sarler, A radial basis function collocation approach in computational fluid dynamics, CMES-Computer Modeling in Engineering and Sciences. 7 (2005) 185-193.

[173] G. Kosec, B. Sarler, Numerical solution of natural convection problems by a meshless method, Convection and Conduction Heat Transfer. 2011.

[174] N. C. Markatos, K. A. Pericleous, Laminar and turbulent natural convection in an enclosed cavity, International Journal of Heat and Mass Transfer. 27 (1984) 755–772.

[175] X. Tian, Z. Shui, C. Ren, Numerical simulation of natural convection in square cavities with power function temperature wall by lattice Boltzmann method, 4th

International Conference on Mechatronics, Materials, Chemistry and Computer Engineering. Atlantis Press, (2015).

[176] U. Projahn, H. Rieger, H. Beer, Numerical analysis of laminar natural convection between concentric and eccentric cylinders, Numerical Heat Transfer. 4.2 (1981) 131-146.

[177] R. J. Krane, J. Jessee, Some detailed field measurements for a natural convection flow in a vertical square enclosure, Proceedings of the First ASME-JSME Thermal Engineering Joint Conference. 1 (1983).

[178] P. U. Ogban, G. F. Naterer, Apparent Entropy Production Difference for Error Characterization in Numerical Heat Transfer, Journal of Thermophysics and Heat Transfer. 34.3 (2020) 659-668.

[179] U. K. N. G. Ghia, K. N. Ghia, C. T. Shin, High-Re solutions for incompressible flow using the Navier-Stokes equations and a multigrid method, Journal of Computational Physics. 48.3 (1982) 387-411.

[180] F. Durst, A. Melling, J. H. Whitelaw, Low Reynolds number flow over a plane symmetric sudden expansion. Journal of Fluid Mechanics. 64.1 (1974) 111-128.

[181] M. S. Engelman, FIDAP Theoretical Manual, Fluid Dynamics International, Evanston, IL (1987)